Interfacing cold atoms and superconductors

Dissertation
der Mathematisch-Naturwissenschaftlichen Fakultät
der Eberhard Karls Universität Tübingen
zur Erlangung des Grades eines
Doktors der Naturwissenschaften
(Dr. rer. nat.)

vorgelegt von
Helge Hattermann
aus Sindelfingen

Tübingen
2013

Tag der mündlichen Qualifikation:	30.08.2013
Dekan:	Prof. Dr. Wolfgang Rosenstiel
1. Berichterstatter:	Prof. Dr. József Fortágh
2. Berichterstatter:	Prof. Dr. Dieter Kölle
3. Berichterstatter:	Prof. Dr. Peter Krüger

Abstract

One of the major challenges of the last decade in physics has been the practical implementation of quantum computing. One very promising candidate for this task are processors using superconducting qubits. While superconducting circuits working in the quantum regime can process quantum information at high rates, they lack the ability to store quantum information on timescales which are longer than a few microseconds. Unfortunately, there is no single quantum system which fulfills all the criteria for a quantum computer. It is therefore very interesting to combine two different quantum systems in order to exploit their respective advantages.

This thesis describes a path towards constructing a hybrid quantum system of ultracold atoms and superconducting microstructures. The ultimate goal of this is a hybrid system in which quantum information is processed by superconducting qubits, transferred using a superconducting coplanar microwave resonator and stored in an ensemble of cold rubidium-87 atoms. The experimental system used to pursue this goal combines a cold atom setup at room temperature with a helium flow cryostat, which is used to cool superconducting structures to a temperature of 4.2 K. Atoms are prepared and trapped in magnetic potentials created by currents in a superconducting microtrap.

We study the influence of the Meissner effect on the magnetic field, which greatly perturbs the magnetic trapping potential when atoms are brought close to superconducting structures.

It is demonstrated that lifetimes of atomic ensembles in the vicinity of superconductors are not limited by Johnson noise induced spin flips, as it would be the case for normal conductors.

We trap atomic ensembles on a superconducting atom chip and subsequently transport them into the gap of a coplanar microwave resonator. The transport is greatly facilitated by screening currents in the resonator ground planes, which keep the magnetic flux inside the superconducting resonator constant. Using these screening currents, a magnetic trap based on persistent currents is created.

We prepare atomic ensembles on the atom chip in a quantum superposition state using a two-photon radio-frequency and microwave transition. The coherence of this superposition is shown to be on the order of $T_2 \sim 10\,\mathrm{s}$, five orders of magnitude longer than the coherence time of superconducting circuits. It is demonstrated that long atomic coherence times can be achieved even in the presence of the nearby superconducting cavity, making atomic ensembles attractive as quantum memories in a hybrid quantum architecture.

In a further experiment, we study the temporal evolution of electric fields close to a metallic surface, when atoms are repeatedly deposited on it. Atoms which are

adsorbed at the surface give rise to an electrostatic field which impacts the energy of Rydberg atoms by the Stark effect. The energy of the Rydberg levels is observed using electromagnetically induced transparency. It is shown that these adsorbate fields can be detrimental in experiments which aim at coupling Rydberg atoms to coplanar resonators, as the Rydberg levels are shifted out of the cavity resonance.

Zusammenfassung

Eine der größten Herausforderungen der Physik unserer Zeit ist die praktische Umsetzung der Quanteninformationsverarbeitung. Einer der vielversprechendsten Ansätze in dieser Hinsicht beruht auf Prozessoren mit supraleitenden Qubits. Mehrere Experimente haben gezeigt, dass supraleitende Schaltkreise, die im Quantenregime arbeiten, in der Lage sind, Quantenalgorithmen auf sehr kurzen Zeitskalen auszuführen. Allerdings ist es mit supraleitenden Bauelementen nicht möglich, Quanteninformation über Zeiten, die länger als ein paar Mikrosekunden sind, zu speichern. Da kein einzelnes Quantensystem alle Bedingungen für einen Quantencomputer erfüllt, besteht großes Interesse an der Konstruktion eines hybriden Quantensystems, das die Vorteile verschiedener Quantensysteme ausnutzt.

Die vorliegende Arbeit beschreibt die Fortschritte in der Realisierung eines hybriden Systems aus ultrakalten Atomen und supraleitenden Mikrostrukturen. Das Ziel ist ein System, in der Quanteninformation mit Hilfe von supraleitenden Qubits verarbeitet wird, über einen supraleitenden koplanaren Mikrowellenresonator übertragen und in einem Ensemble aus kalten Rubidium-87-Atomen gespeichert wird. Der experimentelle Aufbau, mit dem dieses Ziel verfolgt wird, kombiniert eine Anlage zur Erzeugung kalter Atomwolken mit einem Helium-Durchflusskryostaten zur Kühlung supraleitender Strukturen auf Temperaturen von 4,2 K. Atome werden in magnetischen Potentialen, die durch Ströme in den Supraleitern erzeugt werden, gefangen und manipuliert.

Wir untersuchen den Einfluss des Meißner-Effekts auf das magnetische Fallenpotential, wenn Atome in die Nähe supraleitender Strukturen gebracht werden. Der Meißner-Effekt bewirkt sowohl eine Verschiebung des Fallenminimums in Richtung Oberfläche als auch eine Verringerung der Fallentiefe.

Wir zeigen, dass die Lebensdauer atomarer Ensembles in der Nähe von Supraleitern – im Gegensatz zu Normalleitern – nicht durch atomare Verluste, die durch Johnson-Rauschen verursacht werden, begrenzt sind.

Atome werden auf einem supraleitenden Atomchip in einer Magnetfalle gefangen und mit Hilfe von Magnetfeldern in den Spalt eines koplanaren Resonators gebracht. Der Transport der Atome in den Spalt wird durch Abschirmströme in den Masseflächen des Resonators ermöglicht, die den magnetischen Fluss innerhalb des Resonators erhalten. Diese Abschirmströme erlauben ebenfalls die Erzeugung einer Magnetfalle, die auf supraleitenden Dauerströmen beruht.

Durch einen Zweiphotonenübergang, der Mikrowellen und Radiofrequenzen nutzt, werden atomare Ensembles auf dem Chip in einem Quanten-Überlagerungszustand präpariert. Die Kohärenz dieser Überlagerung bleibt auf Zeitskalen in der Größenordnung von $T_2 \sim 10\,\mathrm{s}$ erhalten, fünf Größenordnungen länger als die Kohärenz supralei-

tender Bauelemente. Es wird gezeigt, dass lange Kohärenzzeiten auch in der Nähe des supraleitenden Resonators erreichbar sind. Dies macht Atomwolken als Quantenspeicher in einer hybriden Quantenarchitektur interessant.

In einem weiteren Experiment wird die zeitliche Entwicklung von elektrischen Feldern in der Nähe einer leitenden Oberfläche untersucht, auf die wiederholt Atome aufgebracht werden. Wenn Atome an einer Oberfläche adsorbiert werden, verursachen sie durch Ausbildung eines Dipols ein elektrostatisches Feld, welches durch den Stark-Effekt die Energie von Rydberg-Atomen in der Nähe beeinflusst. Die Energie der Rydberg-Zustände wird mit Hilfe von elektromagnetisch induzierter Transparenz untersucht. Es wird gezeigt, dass die von Adsorbaten erzeugten Felder negative Auswirkungen auf Experimente haben können, in denen Rydberg-Atome an koplanare Resonatoren gekoppelt werden sollen.

List of Publications

This is a cumulative thesis based on the publications listed below. The publications are appended at the very end of the thesis.

Appended Publications

Publication [1] D. Cano, **H. Hattermann**, B. Kasch, C. Zimmermann, R. Kleiner, D. Koelle, and J. Fortágh,
Experimental system for research on ultracold atomic gases near superconducting microstrucures,
Eur. Phys. J. D **63**, 17-23 (2011).

Publication [2] D. Cano, B. Kasch, **H. Hattermann**, R. Kleiner, C. Zimmermann, D. Koelle, and J. Fortágh,
Meissner Effect in Superconducting Microtraps,
Phys. Rev. Lett. **101**, 183006 (2008).

Publication [3] B. Kasch, **H. Hattermann**, D. Cano, T.E. Judd, S. Scheel, C. Zimmermann, R. Kleiner, D. Koelle, and J. Fortágh,
Cold atoms near superconductors: atomic spin coherence beyond the Johnson noise limit,
New. J. Phys. **12**, 065024 (2010).

Publication [4] S. Bernon*, **H. Hattermann***, D. Bothner, M. Knufinke, P. Weiss, F. Jessen, D. Cano, M. Kemmler, R. Kleiner, D. Koelle and J. Fortágh,
Manipulation and coherence of ultra-cold atoms on a superconducting atom chip,
Nat. Commun. **4**, 2380 (2013)
* These authors contributed equally to this work.

Publication [5] **H. Hattermann**, M. Mack, F. Karlewski, F. Jessen, D. Cano, and J. Fortágh,
Detrimental adsorbate fields in experiments with cold Rydberg gases near surfaces,
Phys. Rev. A **86**, 022511 (2012).

Publications not included in this thesis

Publication [6] D. Cano, B. Kasch, **H. Hattermann**, D. Koelle, R. Kleiner, C. Zimmermann, and J. Fortágh,
Impact of the Meissner effect on magnetic microtraps for neutral atoms near superconducting thin films,
Phys. Rev. A **77**, 063408 (2008).

Publication [7] Markus Mack, Florian Karlewski, **Helge Hattermann**, Simone Höckh, Florian Jessen, Daniel Cano, and József Fortágh,
Measurement of absolute transition frequencies of ^{87}Rb to nS and nD Rydberg states by means of electromagnetically induced transparency,
Phys. Rev. A **83**, 052515 (2011).

Publication [8] C. L. Hernández-Cedillo, S. Bernon, **H. Hattermann**, J. Fortágh, and R. Jáuregui,
Scattering of dilute thermal atom clouds on optical Weber beams,
Phys. Rev. A **87**, 023404 (2013)

Contents

1. Introduction: Hybrid Quantum Systems

1.1. The quest for a quantum computer

The practical implementation of a quantum computer has been a very active research topic since Richard Feynman suggested that quantum many-body problems might be simulated best with a computer based on quantum mechanical elements [9]. Such a computer is not based on classical bits which take the values 0 or 1, but by quantum bits or qubits, which may be in an arbitrary superposition of states $c_0 |0\rangle + c_1 |1\rangle$, $|c_0|^2 + |c_1|^2 = 1$. Certain problems can be solved much faster with such a device than it would be possible on any classical machine [10]. Prominent examples of these computations are the Deutsch-Jozsa algorithm [11], factorization with Shor's algorithm [12] and Grover's quantum database search algorithm [13].

However, the experimental realization of a quantum computer with more than a few qubits has proved to be extremely challenging. Numerous approaches to the problem have been developed in the past two decades, involving very different physical systems ranging from solid state devices to single atoms.

The use of trapped ions has so far been the most successful approach to quantum computing [14, 15]. Following a proposal by Cirac and Zoller [16], the first quantum logic gate based on a single ion was demonstrated in 1995 [17]. Many experiments have demonstrated the power of trapped ions for quantum computing: the realization of multi-qubit gates [18] and semiclassical quantum Fourier transform, which paves the way towards the implementation of Shor's algorithm [19] are just two important milestones. A system with trapped ions is also scalable, the current record being 14 entangled ions [20].

While it took some years between the first logic gate and more complex quantum operations with ions, rapid progress has been made using the spin states of molecules in a room temperature liquid. Experiments have successfully implemented Deutsch's quantum algorithm [21], as well as Shor's factorization algorithm [22]. However, it became obvious very early that quantum information processing with nuclear magnetic resonance faces severe limitations in terms of scalability as the signal-to-noise ratio decreases exponentially with the number of qubits [23].

The last decade has seen the advent of all-optical quantum computing [24]. One possible set of basis states in this approach are the vertical and horizontal polarization of photons. Optical waveguides on a chip make it possible to use optical elements for the realization of quantum gates. The on-chip integration of waveguides makes the system highly scalable and facilitates the generation of entangled

states [25], error correction [26] and quantum factoring [27].

Semiconductor qubits, such as quantum dots, also offer good prospects in quantum information processing, which so far have mainly been investigated theoretically [28, 29]. The experimental realization of a semiconducting quantum gate has been demonstrated [30], but more complex schemes seem to be difficult to implement due to the extremely short range of the interaction between qubits.

Superconducting two-level systems coupled to coplanar waveguide resonators [31] have proved to be excellent qubits, which are individually addressable on very short timescales. Using the microwave resonator as a quantum bus [32, 33], it is possible to entangle several of these superconducting qubits [34], perform basic two-qubit [35] and three-qubit [36] operations. It has been shown that this system can even be corrected for errors [37] and perform quantum factoring computations [38]. State-of-the-art chip fabrication techniques make these systems in principle highly scalable.

One very different approach to quantum computation involves Rydberg atoms. Quantum information processing with these atoms is appealing because the interaction between two atoms can be tuned over many orders of magnitude [39]. The physical mechanism behind this tuning is the dipole-dipole interaction between Rydberg atoms, which at close distances leads to the effect of Rydberg blockade [40, 41]. This interaction has been proposed for the implementation of quantum gates [42, 43]. Entanglement between two atoms [44] and the realization of a quantum CNOT-gate [45] have both been demonstrated.

It is already clear from these examples that a quantum system suitable for the construction of a truly useful quantum computer must have a number of different features which have been summarized elegantly by David DiVincenzo [46]. Among these criteria, which we cannot treat in detail in this context, are the prerequisites of a scalable physical system, which has well characterized qubits and can be initialized in a state $|000\ldots0\rangle$. Furthermore, a universal set of quantum gates and coherence times which are much longer than gate operations are necessary, and it must be possible to read out specific qubits. For quantum communication purposes, we also require the ability to convert static qubits into flying qubits (e.g. optical photons) and transmit these between locations where their information is processed.

1.2. Towards hybrid quantum systems

So far, there is no single quantum system which easily fulfills the complete wish list for a quantum computer. Superconducting circuits, for instance, are individually adressable and can process quantum information at very high rates. However, the typical coherence times of these solid state qubits are extremely short - on the timescale of microseconds. Recently, it has been shown that these coherence times can be augmented to about 0.2 ms by decoupling the qubits from their environment [47, 48], but this is still not in the range desired for storing information.

Other quantum systems, like atoms, interact only very weakly with their environment, which means that they are much less subject to decoherence than solid state

systems. Furthermore, due to their rich level structure, atoms provide the ability to convert static qubits into flying qubits in form of photons at optical frequencies, which can be easily transmitted over optical fibers. However, it is difficult to drive transitions efficiently with a single photon. To overcome the shortcomings of individual systems, researchers have started to look into hybrid quantum systems. The idea behind this is very simple, but unfortunately technically very difficult: combine two different quantum systems and exploit their respective advantages. The possibilities of such hybrid quantum systems are very intriguing, and there has been research involving many possible kinds of quantum systems. This area extends far beyond quantum information processing, and involves atoms coupled to mechanical oscillations [49] or superconducting elements coupled to mechanical oscillators in the quantum ground state [50], to name just a few.

Superconducting circuits have proved to be an extremely powerful tool for quantum measurements. Hence, researchers have worked towards coupling superconducting elements to a variety of other quantum systems. A common feature in many of these experiments is that superconducting qubits and the other quantum system are coupled to each other via a superconducting bus in the form of a coplanar microwave resonator.

These approaches are closely related to the development of a quantum memory [51], which is an important issue in the field of quantum information processing. A qubit which is used for processing and manipulation of quantum information, must necessarily be coupled to its environment, otherwise no interaction with any switching or control fields would be possible. However, the coupling to the environment causes the qubits to decohere, making it necessary to store the information on longer timescales in qubits which are decoupled from their surroundings. The development of a quantum memory is also pivotal for applications in quantum repeaters [52] and quantum networks [53]. Another important application of a hybrid quantum system with superconducting qubits is the interface between microwave (MW) photons and optical photons. While superconducting circuits usually work in the GHz regime, it would be very convenient to generate an optical photon based on the presence of a single MW photon, so that established photonic technologies, such as optical fibers and single photon counters, could be used.

There are diverse approaches to create such a hybrid quantum system: recently, several groups have shown collective coupling between a superconducting resonator and nitrogen-vacancy (NV) centers in diamond [54–56]. These NV centers consist of a nitrogen atom next to an empty site in the diamond lattice and have a ground state with spin $S = 1$. They have optical and MW transitions. Strong coupling to a superconducting microwave resonator is relatively easy to achieve, as the number of spins in the resonator mode can be very large. Furthermore, it is possible to store information in a ^{13}C atom close to an NV center, where it can be stored on timescales of 1 s at room temperature [57]. A similar tack uses the spin of ions in solid states to couple to the microwave, with the prospect of using the whole level structure of the involved atoms to serve as in interface between MW and optical photons. Work has been done using Cr^{3+} in ruby [54] and using rare earth spins of

Er^{3+} [58].

Most important for the work of this thesis are proposals to couple trapped neutral atoms to superconducting microwave resonators. Several experiments have already shown the possibility to write single optical photons into atomic ensembles and retrieve the information later [59, 60]. Using an optical resonator, the group of G. Rempe has made it possible to obtain a single-atom quantum memory [61] and remotely entangle Bose-Einstein condensates and single atoms [62]. This system has furthermore been employed to build a quantum network which entangles remote single atoms in cavities [63].

As superconducting qubits operate in the microwave regime, it would be desirable to store microwave photons in atomic ensembles, which have favorable coherence times. Large coupling strengths can be achieved by using polar molecules [64, 65] or Rydberg atoms [66]. Coplanar cavities could also be employed to mediate the Rydberg blockade over the length of the cavity and hence realize quantum gates with remote atoms [67]. However, trapping polar molecules or the excitation of Rydberg states close to a chip is difficult due to interactions between the atoms and the chip surface. It is therefore interesting to look into the prospects of coupling trapped ensembles of cold ground state atoms to a coplanar microwave resonator, using the collective enhancement of the coupling strength through high atom numbers. As theoretically evaluated by Verdú *et al.*, strong coupling between a ^{87}Rb cloud and a superconducting cavity is in principle feasible, but not easy to realize [68]. To achieve this task, one would need very large atom clouds ($N \sim 10^6$ atoms), at distances of a few µm to a low loss cavity ($Q \sim 10^6$). Unfortunately, such high quality factors are not possible with superconducting coplanar resonators at liquid helium temperatures, but only in the millikelvin regime, where the number of thermally excited quasi-particles (unpaired electrons) which lead to dissipation is negligible. Fortunately, it might be possible to observe cooperative effects like superradiance even at higher temperatures, where strong coupling cannot be reached and the cavity mode is occupied with some thermal MW photons [69].

Atoms in a microwave cavity also provide the possibility to transduce microwave to optical photons [70] required for readout and quantum communication: If the atoms absorb a MW photon, the excitation will be stored in the atomic ensemble. By application of a coherent optical control field close to resonance with an intermediate atomic level, an optical photon of deterministic frequency and polarization will be emitted by the atoms as a result of non-degenerate four-wave mixing.

1.3. Atoms and superconductors

Cold atomic physics is now a mature field that has developed a large toolbox of standard techniques. Since the development of laser cooling and trapping of neutral atoms in magneto-optical traps [72], countless different means to store, manipulate and cool atoms have been investigated, culminating in the observation of Bose-Einstein condensation in 1995 [73, 74]. Researchers can now routinely trap

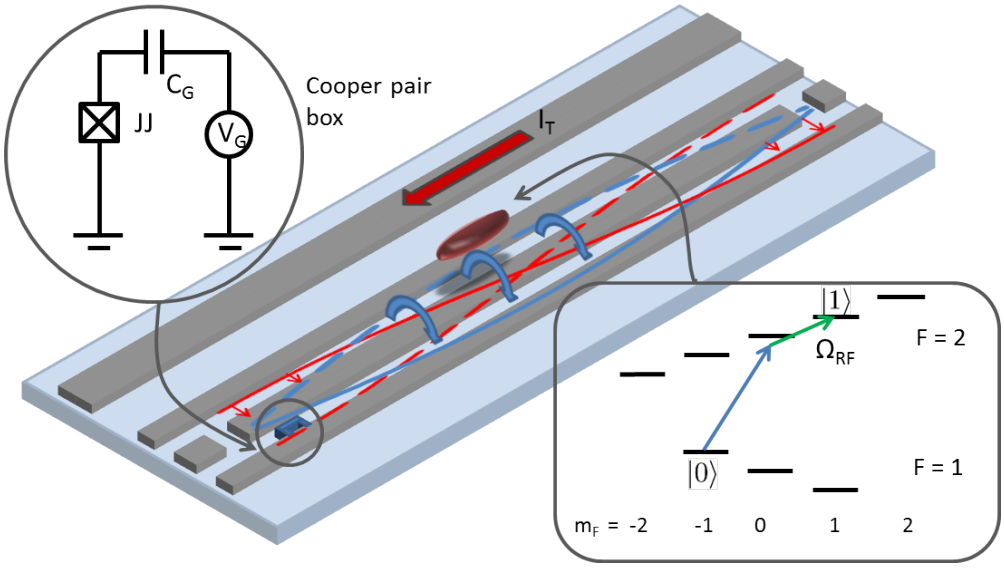

Figure 1.1.: Envisioned hybrid system of cold atoms and solid state qubits. In this system, a charge qubit (cooper pair box) is coupled to the electric field (red) of a superconducting coplanar waveguide resonator. The energy of the charge qubit can be tuned by the voltage V_G at the gate capacitor C_G [71]. Cooper pairs can tunnel through the Josephson junction (JJ) into the box. If the energy difference between the ground (n cooper pairs) and excited ($n+1$ cooper pairs) state of the box corresponds to the frequency of the resonator, the excitation can be transferred from the qubit to the resonator and vice versa. The magnetic field of the resonator photon (blue) couples to the magnetic moment of the trapped atom cloud. Together with a radio frequency field, this allows the transfer of atoms from state $|0\rangle$ to state $|1\rangle$. Due to its long coherence time, the atomic ensemble can be used as quantum memory. By employing an optical control field (not shown in the picture) the atomic ensemble can also be used as a microwave-to-optical photon interface [70].

dilute clouds of bosonic or fermionic atoms in optical potentials [75] or miniaturized magnetic traps [76] and cool the ensembles to quantum degeneracy. Using these techniques, we investigate the possibility of storing atoms close to conducting and superconducting surfaces. We exploit the capability of atom chips to generate almost arbitrary potentials which can be used to trap atoms at distances down to a few micrometers from the surface. In such an arrangement, atomic clouds can be used as very sensitive field and force probes. They have the capability to measure magnetic field modulations caused by spatial current variations [77] as well as tiny electric fields caused by surface adsorbates [78]. Atoms even provide the possibility to measure fundamental physical effects such as the Casimir-Polder force [79, 80]. This sensitivity makes it possible to use atomic clouds in a manner very similar to scanning probe microscopes [81].

In addition to applications in quantum information processing, there are fundamental reasons to study hybrid systems of cold atoms and superconductors. One such reason can be observed in normal conducting traps, when cold atoms are

brought close to metallic surfaces: the atomic lifetime in the magnetic trap drastically decreases and the atoms are lost from the trap [82–84]. The relevant loss mechanism is the magnetic near field noise due to thermally excited electrons in the metal. These field fluctuations cover a white power spectrum and contributions at the Larmor frequency couple to the magnetic moment of the trapped atom, which causes its spin to flip into an untrapped Zeeman state. The interest in superconducting traps for atoms was therefore greatly increased by the theoretical prediction that lifetimes near superconductors would not be limited by such noise [85], as all electronic excitations below the depairing energy of cooper pairs are forbidden.

The first demonstration of a superconducting atom chip was in the group of S. Haroche in Paris [86], followed by the experimental realization of an atomic trap based on persistent currents in a superconducting loop by the team of T. Mukai in Tokyo [87]. Although the atoms in this experiment were far away from the chip surface, the possibility of using persistent currents for trapping is a major breakthrough, as it makes the use of inherently noisy current sources unnecessary.

Since the first superconducting traps, several groups have made advances towards the implementation of a hybrid quantum system of atoms and superconductors. The Paris group was the first to achieve Bose-Einstein condensation on a superconducting atom chip [88]. Several groups investigated the influence of flux penetration on the trap geometry and stability [89, 90]. This led to the generation of magnetic traps based on the field of Abrikosov vortices in superconducting thin films [91, 92]. These vortices were introduced by applying strong magnetic fields (larger than the critical field) to the superconductor. Using magnetic field pulses in alternating directions, the group of R. Dumke (Singapore) accomplished the formation of programmable vortex traps, which do not require external bias fields [93]. This approach has been studied for different geometries of the superconductor both theoretically [94, 95] and experimentally [96].

Abrikosov vortices can also lead to loss and decoherence of trapped atoms, as vortices can be moved by the driving force of a transport current or thermal excitation and hence generate fluctuations of the magnetic field [97, 98]. The limited lifetimes measured by the Paris group, however, are in agreement with Johnson noise generated by the gold layer on the superconducting chip [99] and do not need to be explained by vortex noise.

In the work presented in this thesis, we interface superconductors and cold atoms [1]. We study fundamental properties of superconducting traps, namely the influence of the Meissner effect on the trapping geometry [2, 6] and the suppression of Johnson noise in superconducting traps [3]. We trap atoms on a superconducting atom chip where we can create large Bose-Einstein condensates of up to 10^6 atoms. We bring the atoms into the gap of a superconducting quarter-wave resonator, where we measure the coherence of superposition states in the atoms to evaluate the applicability of this system as a quantum memory. The transport into the resonator is assisted by screening currents in the resonator, a finding which is corroborated by comparison with numerical simulations. The currents in the superconducting resonator can also be used to generate a persistent current trap.

This is a cumulative thesis which summarizes the work which has been done at the University of Tübingen on atoms and superconductors. Chapter 2.1 outlines the technical challenges involved in combining cryogenic technology with the demands of a cold atom experiment. Chapter 2.2 covers the measurements on the influence of the Meissner-Ochsenfeld effect on the magnetic trap, chapter 2.3 shows the suppression of Johnson noise in superconducting traps by comparison of atomic lifetimes near niobium and copper. Chapter 2.4 covers the results on coherence measurements in the gap of a superconducting resonator. Measurements on the excitation of Rydberg atoms near conducting surfaces [5] are presented in chapter 2.5. These measurements show the potential limits of experiments with Rydberg atoms and coplanar microwave resonators. This thesis has several appendices that cover some topics which are not found in the publications. Appendix A.1 gives a description of the superconducting atom chip and its implementation in the experiment. An explanation of the employed laser system can be found in appendix A.2. The foundations of Ramsey interferometry and a semiclassical treatment of one- and two-photon Rabi oscillations can be found in appendix B. Furthermore, some details on the numerical simulations of the transport into the gap of a coplanar resonator are given in appendix C. The publications this thesis is based on can be found at the very end of the document.

Contributions

This section outlines the main contributions that have been made to the manuscripts of this thesis. The experiments were proposed and supervised by József Fortágh, Claus Zimmermann, Reinhold Kleiner and Dieter Koelle. All authors discussed the results of the experiments and the manuscripts.

- **Publication 1**

  The experiment was set up by Daniel Cano, Brian Kasch and myself in joint work. I particularly contributed to the set-up of the laser system and the transport of atoms with optical tweezers. The entire experiment was later rebuilt in another laboratory by Florian Jessen and myself. The manuscript was mainly written by Daniel Cano and József Fortágh, with some contributions from myself.

- **Publication 2**

  The measurements on the Meissner effect were done by Daniel Cano, Brian Kasch and myself. We all set up the experiment, worked on the preparation of cold atomic samples and the transport into the superconducting microtrap. Daniel Cano did most of the data evaluation and wrote the manuscript, together with József Fortágh.

- **Publication 3**

  The experiment was set up by Daniel Cano, Brian Kasch and me. Brian Kasch and I made most of the lifetime measurements and their evaluation. The theoretical framework was developed by S. Scheel. Brian Kasch, József Fortágh and I wrote the manuscript.

- **Publication 4**

  The superconducting chip was designed by Daniel Bothner (resonator structures), Martin Knufinke (ring design) and myself (trapping structures). Simon Bernon, Matthias Kemmler, Martin Knufinke, Florian Jessen and I implemented the chip into the experiment. All measurements were done and evaluated by Simon Bernon, Patrizia Weiß and myself. Martin Knufinke, Simon Bernon, Daniel Cano and I did the magnetic field calculations. The manuscript was jointly written by Simon Bernon, József Fortágh and myself.

- **Publication 5**

  The measurements on the Rydberg atoms were done by Markus Mack, Florian Karlewski and myself. I did the evaluation of the measurements, based on Stark effect calculations by Markus Mack. Daniel Cano, József Fortágh and I wrote the manuscript.

2. Summary of publications

2.1. Publication 1: Experimental system for research on ultracold atomic gases near superconducting microstructures

The realization of a hybrid quantum system of ultracold atoms and superconducting quantum structures is a major technical challenge. Both systems have their respective requirements, which are very well controllable separately, but largely unexplored in combination. This is especially true for the incorporation of ultra-high vacuum (UHV) and cryogenic technologies. Thermal conductive epoxies or soft metals like indium are usually used in cryogenic apparatuses, but due to high outgassing are not suitable for ultra high vacuum. This particularly applies if the vacuum chamber needs to be baked at temperatures of 200 °C to reach a final pressure in the range of 10^{-11} mbar. On the other hand, one has to make sure that there is sufficient cooling power for the superconducting sample even in absence of any cryogenic liquids or buffer gases. This requires care in the screening of thermal radiation from the environment and in thermal anchoring of electrical contacts that are connected to room temperature devices outside of the chamber.

In **publication 1**, we describe our approach to meet these challenges. We have developed an experimental system which combines a room-temperature apparatus for the preparation of cold atoms with a helium flow cryostat used to cool the superconducting structure in a single vacuum chamber (Fig. 2.1). Atomic ensembles are prepared in the room temperature region by cooling in a magneto-optical trap (MOT). Atoms in the trap are subsequently transferred into a magnetic quadrupole trap generated by the MOT coils and transported into a Ioffe-Pritchard-type magnetic trap, where the atoms are cooled by radio frequency forced evaporation to temperatures of roughly 1.5 µK.

After cooling, the atomic cloud is brought from the room temperature electromagnets to the superconductor at 4.2 K by means of optical tweezers [100]. The atomic cloud is trapped in the focus of a red-detuned laser beam [75] and transported from the Ioffe trap to a position a few hundred µm below the superconducting structure by moving the focusing lens on an air bearing translation stage.

The superconducting structure is attached to the lower end of a UHV-compatible helium flow cryostat (Janis ST-400, Cooling power 2 W at 4.2 K), a double-walled stainless steel tube with a length of 1 m. Liquid helium flows through the inner tube, cools a copper surface at the lower end of the cryostat and flows out in gaseous form on the outer side. Temperatures down to 2 K can be achieved by pumping the

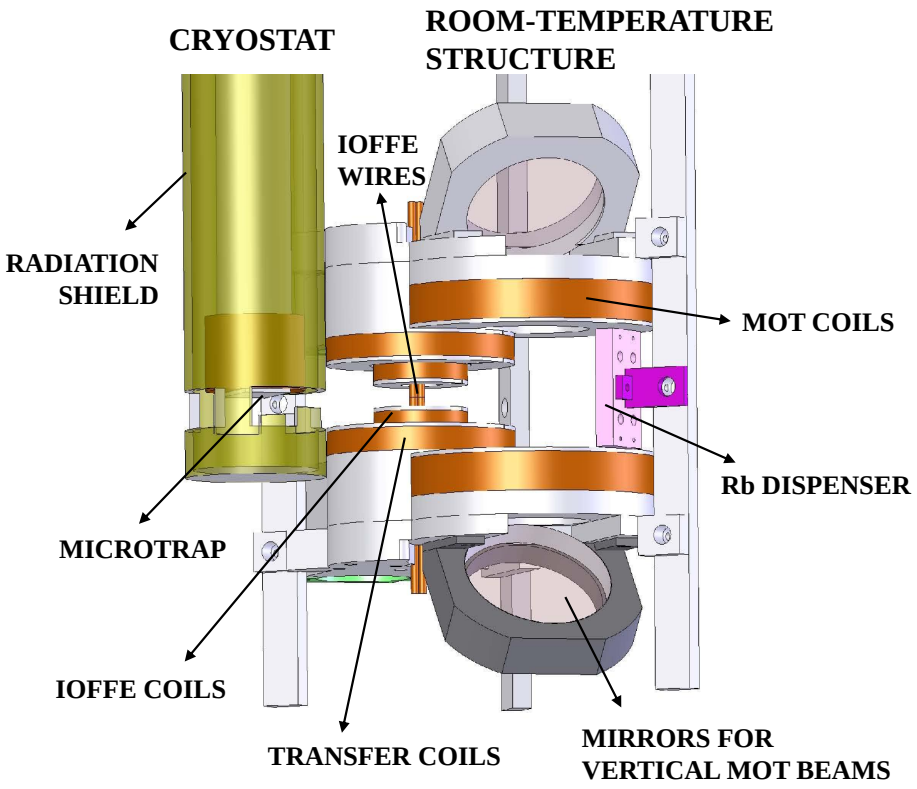

Figure 2.1.: Drawing of the *in-vacuo* set-up. The electromagnets on the right side are at room temperature, while the cryostat on the left side at a temperature of 4.2 K, surrounded by a radiation shield at 25 K. Figure taken from [1]. Reprints with kind permission of The European Physical Journal (EPJ)

helium return line. Due to the low thermal conductivity of steel, the temperature of the outer tube varies from 4.2 K at the bottom to room temperature at the upper flange, where the cryostat tube is attached to the outer vacuum chamber.

The lower end of the cryostat is surrounded by a radiation shield at $T \sim 25\,\mathrm{K}$ to minimize the impact of black body radiation from the environment on the superconducting sample. The shield is a gold plated copper cylinder with slits about 2 mm in height which allow optical access to the cryogenic region and makes transporting with optical tweezers to this environment possible.

This publication reports on the demonstration of superconducting cold atom microtraps based on a simple niobium wire ($\varnothing = 125\,\mu\mathrm{m}$), which was clamped between two copper surfaces to maximize the thermal contact (Fig. 2.2). By superimposing an external magnetic field with the field generated by a current in the wire, a line of vanishing magnetic field parallel to the wire is created. Axial confinement was ensured by two copper wires running perpendicular to the Nb wire. An additional

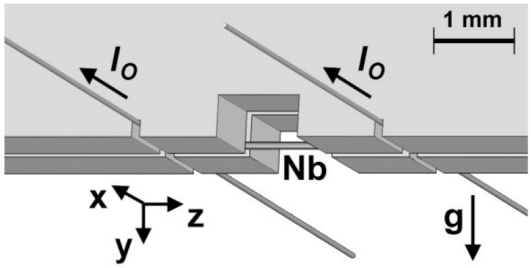

Figure 2.2.: Drawing of the superconducting microtrap generated by current in a Nb wire and a magnetic field applied perpendicular to the wire. The wire of 125 µm diameter is clamped between two copper plates to ensure thermal contact. A pair of wires perpendicular to the Nb wire provide axial confinement of the trap. Figure taken from [2]. Reprints with permission of the American Physical Society (AIP).

offset field parallel to the superconductor lifts the magnetic field zero in the center of the trap to avoid Majorana spin flips [101]. We load 10^6 atoms at a temperature of $T = 1\,\mu\text{K}$ into a trap with radial and horizontal oscillation frequencies of $\omega_r = 2\pi \cdot 135\,\text{s}^{-1}$ and $\omega_l = 2\pi \cdot 21\,\text{s}^{-1}$, respectively.

This system represents a major technical step in the realization of a superconducting/cold atom hybrid system. It allows the achievement of Bose-Einstein condensation and long lifetimes of trapped atoms, proving excellent vacuum conditions. Although the superconducting component in this experiment was extremely simple, it paves the way for the implementation of more complex devices, such as superconducting atom chips.

2.2. Publication 2: Meissner effect in superconducting microtraps

Coupling ultracold atoms to a superconducting solid state system requires trapping an atomic ensemble in close proximity to superconducting surfaces. This can be achieved in several ways, for instance with optical dipole potentials or magnetic traps. Magnetic trapping is a well understood technique that makes it possible to easily manipulate the trapping parameters, such as position and oscillation frequencies by simply changing currents in wires and coils. However, when using superconducting structures to create the trapping fields, the Meissner effect [102] plays a significant role that must be understood in order to allow the same degree of control that is obtained with normal conducting magnetic microtraps.

In **publication 2**, we study the impact of this field exclusion, when atoms are trapped at distances which are comparable to the width of the superconducting structure. We find that the Meissner effect significantly influences the magnetic trap both in position and in the depth of the potential.

To measure this effect, we trapped ensembles of cold atoms in a magnetic trap

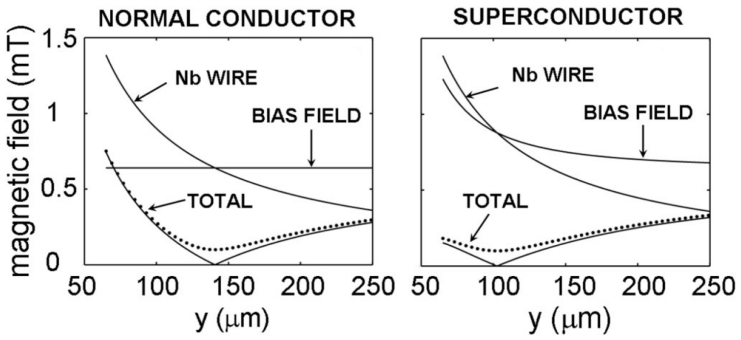

Figure 2.3.: Modulus of the magnetic-field profiles calculated for $I_{\mathrm{Nb}} = 0.45\,\mathrm{A}$ for the normal-conducting and the superconducting cases, respectively. The comparison shows that the Meissner effect strongly distorts the bias field while leaving the field of I_{Nb} unchanged. This results in a lower trap depth and a shorter distance to the Nb wire. The realization of the microtrap requires that the bias field is opposite in direction to B_{Nb}. The additional offset field $B_0 = 10^{-4}\,\mathrm{T}$ along the z direction changes the magnetic profile from linear to parabolic (dotted curve). Figure and caption taken from [2]. Reprints with permission of the American Physical Society (AIP).

formed by a Nb wire of 125 µm diameter (fig. 2.2) and measured their position by *in-situ* absorption imaging for different currents in the wire. While for a normal conductor the distance to the wire would be proportional to the current, we found significant deviation from this behavior in the case of a superconductor. The field exclusion leads to an inhomogeneous external field with an increased strength close to the wire. As a consequence, the line at which this field cancels the field of the wire is shifted towards the surface (fig. 2.3). The decreased distance of the trap to the conductor surface is associated with a decrease in the trap depth. Hence it was not possible to bring an the atoms to distances of less than $\sim 20\,\mu\mathrm{m}$ from the surface of the wire. The trap was found to open towards the surface and atoms were lost from the trap.

These measurements were performed for different temperatures. For temperatures $T < 6\,\mathrm{K}$ the wire was found to be in the pure Meissner state. For higher temperatures, we observe that the trap approaches the position expected in the normal conducting case. This finding can be explained by the penetration of magnetic flux at the borders of the wire, as the critical field decreases with higher temperatures.

In order to realize a hybrid system of atoms and superconductors, in which the coupling strongly depends on the distance, it is vital to take the reduction of the trap depth due to the Meissner effect into account. If possible, one should minimize the impact of the field expulsion by miniaturization of the superconducting structures. We have done so by implementing the superconducting atom chip described in appendix A.1, which is used for more sophisticated experiments, as described in section 2.4.

Complementary to the presented measurements, a numerical routine for the calculation of the Meissner effect for atom chips was developed [6, 103]. These numerical methods were used for the design and simulation of the chip presented in section 2.4.

The understanding of the Meissner effect is an important step in constructing a hybrid system of cold atoms and superconductors. Our results allow us to predict the impact of the superconductor on the magnetic trap and to design superconducting atom chips in a way that minimizes spurious influences of the Meissner effect on the trapping parameters.

2.3. Publication 3: Cold atoms near superconductors: atomic spin coherence beyond the Johnson noise limit

Trapping atoms at distances of a few µm to a solid-state system is necessary to achieve sufficiently strong interaction between the magnetic or electric dipole moment of the atoms and the fields of the investigated devices (microwave resonators, Josephson junctions, SQUIDs). This proximity, however, is a possible source of decoherence. While atoms magnetically trapped in a vacuum chamber are nearly perfectly isolated from the environment, they will be subject to losses when brought close to a conducting surface. These losses are caused by the thermal motion of the electrons in the material, which leads to a nearly white noise spectrum of the magnetic field in the vicinity (Johnson noise or Johnson-Nyquist noise [104]). Noise components at the atomic Larmor frequency ω_{L} lead to spin flips and hence loss of atoms from the magnetic trap [105, 82–84].

On the other hand, theoretical calculations have predicted the suppression of Johnson noise in superconducting traps [85, 106, 107]. Since all electronic excitations within the energy gap of superconductors are forbidden, spin flip lifetimes of $\tau \approx 5 \times 10^3\,\mathrm{s}$ for a distance of $d = 1\,\mu\mathrm{m}$ and $\tau \approx 10^7\,\mathrm{s}$ at $d = 10\,\mu\mathrm{m}$ can be expected close to a superconductor.

In **publication 3**, we give experimental proof of the suppression of Johnson noise in superconductors. Thermal clouds of ^{87}Rb were trapped in a magnetic trap and brought in proximity to the superconductor, and to a normal conductor for comparison. A magnetic trap was generated by a current in a 125 µm Nb wire and an external magnetic bias field perpendicular to the wire, as described in section 2.1. An offset field parallel to the wire was applied to lift the degeneracy of the Zeeman states of the hyperfine structure and to prevent Majorana losses at the trap minimum [101]. This field leads to a harmonic potential near the trap minimum and to a larmor frequency $\omega_L = \frac{1}{2}\mu_{\mathrm{B}}\, B_0/\hbar$, which corresponds to the energy distance between two adjacent Zeeman levels. To bring atoms close to the superconductor, the current in the Nb wire was reduced. Alternatively, the atoms were brought close to a normal conducting copper surface by turning the bias field about the wire axis. In doing so, care was taken to keep the offset field constant. After a variable holdtime, the trap was switched off and the number of remaining atoms

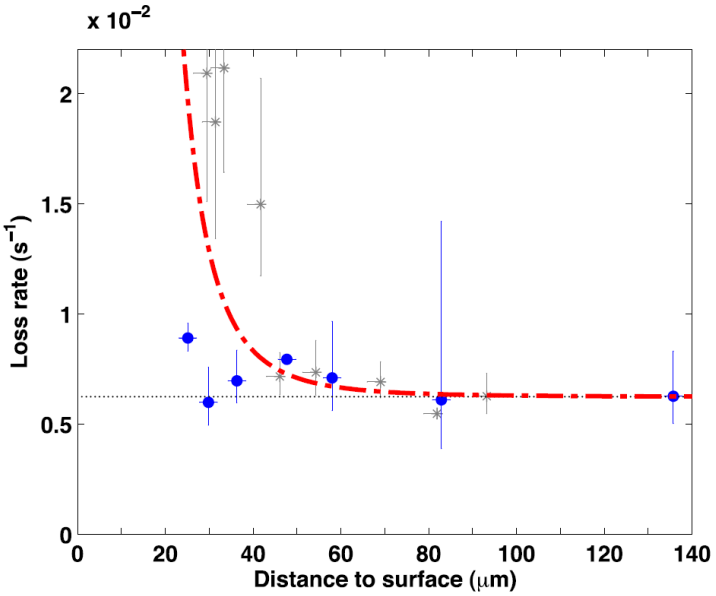

Figure 2.4.: Atom loss rate near superconducting niobium at 4.2 K (blue circles) as a function of the atom-surface separation. The dash-dotted line (red) is the Johnson noise loss rate near normal conducting copper at 4.2 K including the measured vacuum background loss (black dotted line). The data below the Johnson noise limit give evidence that magnetic field noise near superconductors is reduced compared with normal metals. A comparison measurement near copper is shown by the gray points. Figure and text taken from [3]. Reprinted with permission of the Institute of Physics and IOP Publishing Limited.

was determined in a time-of-flight image.

The measurements clearly showed a reduction of the lifetime of trapped atoms for distances $d < 40\,\mu\text{m}$ to the copper surface, with loss rates higher than predicted by Johnson noise theory (Fig. 2.4). In contrast, measurements close to the niobium surface showed loss rates on the order of the background gas collision rate at distances down to 20 µm, corresponding to lifetimes $\tau > 100\,\text{s}$. The measured loss rate lies well below the theoretical prediction for Johnson noise induced loss. This result provides the first experimental evidence that magnetic near-field noise near the superconductor is strongly suppressed.

Measurements at smaller distances were not feasible in the system presented, as the expulsion of the bias field from the niobium wire by the Meissner effect drastically changed the trapping geometry and the trap opened towards the wire surface. As this effect can be circumvented by using superconducting thin film structures, we have developed a superconducting atom chip (appendix A.1).

2.4. Publication 4: Manipulation and coherence of ultra-cold atoms on a superconducting atom chip

A hybrid quantum system, in which cold atoms are used as a quantum memory, requires not only long trapping times, but also a long-lived coherence of an ensemble in a quantum superposition state $|\Psi\rangle = c_0 |0\rangle + c_1 |1\rangle$ [51]. Coherence times of several seconds [108, 109] and even up to one minute [110, 111] have been reported in samples of trapped ^{87}Rb. However, the coherence of such a superposition in the presence of a superconducting resonator, which strongly impacts the trap properties by the Meissner effect, has never been studied before. To advance towards the realization of a cold atom quantum memory coupled to superconducting qubits, it is important to study the coherence in close proximity to a coplanar resonator structure.

In **publication 4**, we report on the trapping of atomic clouds on a superconducting atom chip and the magnetic transfer of the ensemble into the mode volume of a quarter-wave coplanar microwave resonator (Fig. 2.5(a-b)), where we study the coherence time of superposition states. Transporting the atoms into the resonator is facilitated by screening currents in the ground planes, which are induced when a field is applied perpendicular to the chip. These screening currents conserve the flux within the gaps of the resonator structure. The currents strongly modify the magnetic fields in the vicinity of the superconductor and lead to a focusing of the magnetic trap into the gap of the resonator. The observed behavior is in excellent agreement with numerical simulations of the chip which include magnetic flux conservation in the gaps as well as Meissner currents that keep the interior of the superconductors flux free (see Fig. 2.5(c), and appendix C for an extensive treatment).

We demonstrated the generation of a magnetic trap based on persistent currents in the resonator and an external bias field. The trap did not require driving currents on the chip with external current sources, hence avoiding a significant source of noise in cold atom experiments. These experiments are the first demonstration of magnetically trapped atoms in a superconducting resonator structure. In contrast to several proposals [112, 70], it does not require optical methods to trap atoms inside the gap and hence does not suffer from the detrimental influence of light on the functioning of the superconducting chip.

We performed Ramsey interferometry (see appendix B) to study the coherence properties of an atomic ensemble at different positions on the chip: at a reference position 60 µm below the chip, in the gap of the resonator 14 µm below the surface and in a persistent trap 25 µm below the central conductor of the cavity. In all three positions, we observed coherence on timescales of several seconds, revealing the effect of spin self rephasing mechanisms, as described in appendix B.4.2.

We found that the coherence of the state was significantly affected by the presence of a superconducting structure in proximity to the atoms, as the high trap frequencies caused by field focusing into the gap make it increasingly difficult to

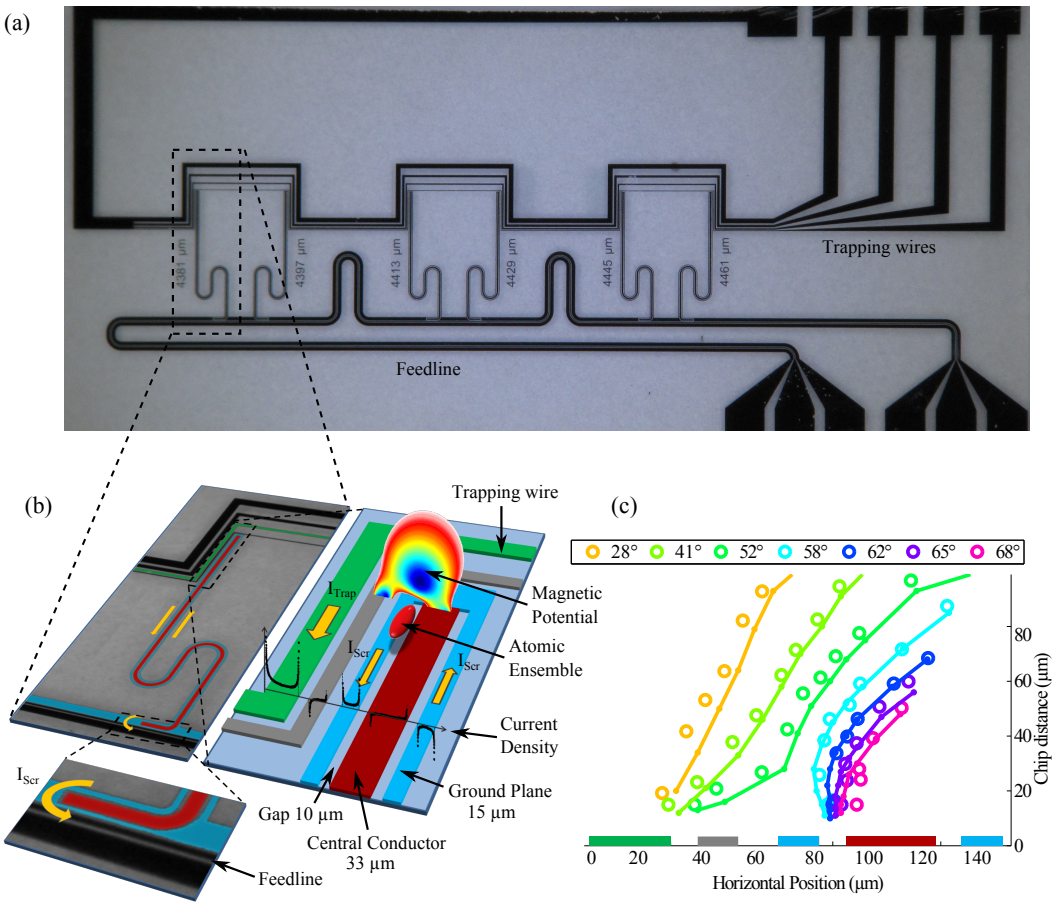

Figure 2.5.: (a) Microscope image of the superconducting atom chip. Atoms are magnetically trapped by currents in the trapping wires and subsequently transferred into the gap of the superconducting coplanar resonator. (b) Schematic trapping of atoms in a quarter-wave resonator. Atoms are trapped by the fields generated by the current I_{Trap} in the trapping wire and the external bias field. If this field has a component perpendicular to the chip, screening currents I_{Scr} in the closed loop of the ground planes are induced, which keep the flux inside the resonator gaps constant. These currents lead to a minimum of the magnetic field above the gap, as seen in the simulated potential plot. (c) Position of the trap as measured by in-situ absorpion imaging for different currents in the trapping wire and different angles of the external bias field. For large angles, the trap is focussed into the gap between the central conductor and the ground plane of the resonator. The measurements (circles) are in good agreement with simulations based on the Meissner effect and flux conservation in the gaps (solid lines and dots). Details on the simulations can be found in appendix C.

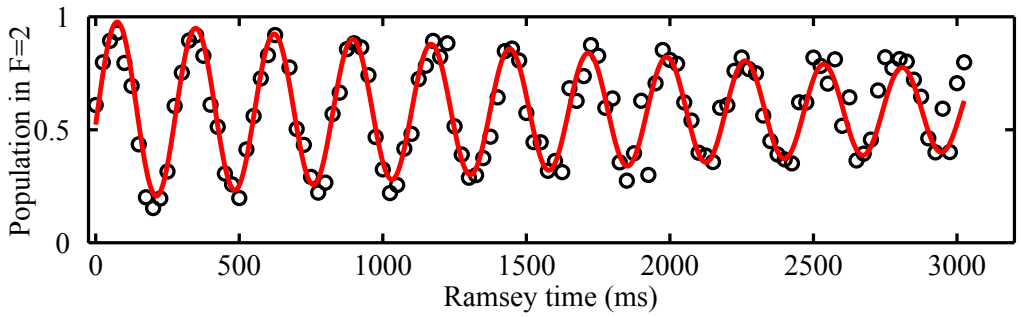

Figure 2.6.: Ramsey interferometry measurement in the gap of the coplanar waveguide resonator with a detuning of $\delta = 4.4\,\mathrm{Hz}$. The measurement was performed on a thermal cloud of 1.25×10^4 atoms at a temperature $T = 335\,\mathrm{nK}$ in a trap with frequencies $\vec{\omega} = 2\pi \cdot (17, 451, 390)\,\mathrm{Hz}$. The measurement shows a coherence time of $T_2 = 3.9\,\mathrm{s}$. The rather low contrast at the beginning of the measurement can be attributed to inhomogeneous Rabi frequencies due to the presence of superconducting structures and noise in the detection of small atom numbers.

reach the self rephasing regime. However, the observed coherence of $\sim$4 s in the gap of the cavity (Fig. 2.6) is still five orders of magnitude greater than of the best superconducting qubits, making atomic ensembles attractive as a quantum memory.

As a further step towards strong coupling between neutral atoms and superconducting coplanar resonators, we demonstrated the preparation of large thermal ensembles on the superconducting chip. We have generated thermal clouds of several million atoms at µK temperatures and pure Bose-Einstein condensates of 3.5×10^5 atoms on the chip, paving the way towards the observation of collectively enhanced cavity effects, such as superradiance and the generation of an on-chip micro maser.

2.5. Publication 5: Detrimental adsorbate fields in experiments with cold Rydberg gases near surfaces

The coupling strength between neutral atoms and coplanar cavities could be greatly enhanced by exciting atoms into Rydberg states, which are highly polarizable and have large electric dipole moments. Theoretical proposals suggest Rydberg atoms could strongly couple to the electric field of single microwave photons in the cavity [66], leading to long-range dipole interactions across the mode volume of the resonator [67].

As strong coupling requires the atom cloud to be trapped close to the atom chip, stray fields from the surface may become important. Particularly critical are electric fields created by atoms adsorbed at the surface. These atoms partly donate their valence electron into the material. The electron is still bound to the adsorbed atom and the spatial charge separation (~ 1 Å) forms a permanent electric dipole which is oriented perpendicular to the surface and leads to an inhomogeneous electric field in

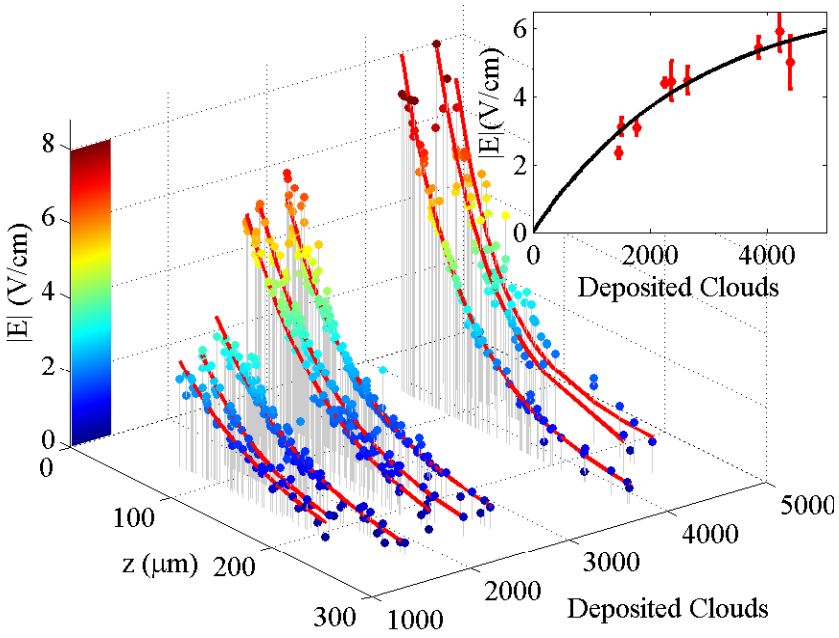

Figure 2.7.: Measured electrostatic field as a function of z and the number of experimental cycles carried out. Inset: Measured electrostatic field at a distance of 80 µm from the surface. We observe an increase of the electric field due to adsorption of rubidium onto the copper surface. The saturation builds up after the deposition of few thousand atomic clouds. Figure and caption taken from [5]. Reprints with permission of the American Physical Society (AIP).

its vicinity [113, 78]. This electric field again causes a perturbation of the energies of Rydberg states close to atom chips [114]. As the fields are spatially inhomogeneous, the Rydberg energies will also depend on the distance to the surface. Repetition of experiments close to the chip results in an additional deposition of adsorbates on the surface, which changes the electric field and thus the energy of the Rydberg states after each run of the experimental cycle. This could shift Rydberg atoms out of resonance of a coplanar microwave resonator.

In **publication 5** we systematically studied the effects of surface adsorbates on the energy of Rydberg states. Clouds of $N \approx 10^6$ atoms at a temperature of $T = 1.5\,\mu\text{K}$ were repeatedly dropped from an optical dipole trap onto a copper surface. The energy of the Rydberg states was measured during time of flight by absorption imaging of the atoms, which was performed on the atomic transition $5S_{1/2}F = 2$ to $5P_{3/2}F = 3$. A part of the ensemble was simultaneously illuminated by a *coupling laser* with a wavelength of $\lambda \sim 480\,\text{nm}$. When the coupling laser is resonant with the transition from the state $5P_{3/2}F = 3$ to a Rydberg level, the conditions for electromagnetically induced transparency (EIT) are fulfilled [115] and the absorption of the imaging light by the atoms is strongly reduced. Adsorbates on

the surface, however, lead to a Stark shift of the Rydberg states, so that the transparency conditions are changed with the distance to the surface. By determination of the distance of the transparency window for different coupling laser detunings and comparison with calculations of the Stark shift, it is possible to obtain a spatially resolved measurement of the electric field strength. The field was found to decay in good approximation exponentially with the distance to the surface.

Beginning with a surface clean of adsorbates, the temporal evolution of the field strength was measured by repeatedly depositing atomic clouds onto the metallic surface (Fig. 2.7). Continuous EIT measurements on Rydberg S- and D-states with principal quantum numbers ranging from $n = 31$ to $n = 48$ were performed. These experiments showed that adsorbates lead to an electric field strength of $1\,\mathrm{V/cm}$ at a surface distance of $30\,\mu\mathrm{m}$ after as little as 100 repetitions of the experimental cycle. This shows that adsorbates can make reproducible measurements on Rydberg atoms and microwave resonators impossible, as the adsorbate fields shift the atoms out of the cavity resonance after a very low number of experimental cycles. Hence it is absolutely essential to find strategies to impede or compensate the deposition of alkali atoms on the chip surface. Compensation is in principle possible by means of electrodes on the chip, however, it is very difficult to compensate the electric field over a large volume, due to the extreme inhomogeneity of the adsorbate fields.

The measurements indicated a saturation of the field strength after the deposition of a few thousand atomic clouds. It is still unclear if the variations in this saturation regime are small enough to permit measurements on coplanar microwave resonators. The line shift of Rydberg atoms is approximately quadratic with the field strength, so that already small variations could greatly affect the Rydberg energies. Hence, for the realization of cavity QED measurements with Rydberg atoms in microtraps, our measurements show the importance of finding methods that can completely remove adsorbates from the surface or prevent their deposition.

3. Conclusion and Outlook

3.1. Conclusion

This work has studied the feasibility of a hybrid quantum system of superconducting microstructures and ultracold atoms. Concluding this thesis is an assessment of the achievements and an outlook on the remaining steps required to realize such a solid state - quantum gas hybrid.

The combination of cryogenic technology with the requirements of an atomic physics apparatus is an experimental challenge par excellence. We have shown that it is possible to meet the requirements of such a system using a single vacuum chamber set-up including both room-temperature electromagnets and a helium flow cryostat. The achievement of Bose-Einstein condensates with up to 10^6 atoms on a superconducting atom chip proves the functioning of the experimental system. Care has been taken to choose only vacuum- and cryo-compatible materials which can also be baked to temperatures of 200°C. It would be possible to circumvent this experimental complexity by using a two-chamber system, where the atomic ensemble is prepared in one vacuum chamber and then transported into a cryogenic chamber. This could decrease the experimental challenges, as cryogenic pumping in the cold region would render baking of the superconducting region unnecessary, but would come with an increased difficulty in the transport of the atomic ensemble, which in our set-up is done very reliably by optical tweezers.

We have measured the influence of the Meissner effect on the parameters of the magnetic trap by bringing a cold atomic cloud into close proximity with a superconducting wire. Additionally, we have developed accurate numerical calculations on the impact of the field exclusion on magnetic traps. These simulations are also a key point in designing microtraps that avoid a deleterious consequence of the Meissner effect, namely the drastic reduction in trap depth close to superconductors. Using microstructured current leads for the generation of magnetic trapping potentials makes it possible to bring atoms within 5 µm of superconducting structures.

We have demonstrated the transport of cold atoms into the gap between the ground planes and the central conductor of a superconducting quarter-wave resonator, where the magnetic field of the microwave and hence the coupling strength is expected to be maximum. The transfer into the resonator gap was facilitated by screening currents in the closed superconducting loop of the resonator. It must be noted that these screening currents would not be present in a capacitively coupled half-wave resonator, as there is no closed loop. Flux conservation in our system has furthermore enabled the creation of persistent current traps, generated by shielding currents circulating in the resonator ground planes.

Comparing atomic lifetimes close to normal conductors and superconductors, we proved the strong suppression of Johnson-Nyquist noise in a superconducting wire. This is an important finding for the realization of superconductor - quantum gas hybrids, as it shows that the proximity to the surface does not limit the timescale on which quantum information could be stored within the atomic cloud. More important for the construction of a quantum memory, however, is the coherence time T_2 of a quantum superposition state. Our experiments have shown that we can reach coherence times of up to 20 s on a superconducting atom chip and up to 4 s in the gap of a superconducting coplanar resonator. While this is not yet in the regime reached by Deutsch *et al.* [110], it shows that quantum coherence on very long timescales can be achieved in the presence of superconducting structures. Reaching coherence times on the order of one minute is only a matter of optimizing the atomic density and temperature. As these are strongly dependent on the magnetic confinement, optimization will require precise design of superconducting magnetic structures, taking particular care that the Meissner effect and flux conservation in closed loops are included in the design calculations.

These results, proving that long coherence times can be achieved in the vicinity of a superconducting resonator, are the first and important steps towards the implementation of a cold atom quantum memory for microwave photons.

Additionally, we demonstrated the preparation of large thermal and Bose-Einstein condensed ensembles on the atom chip, which is an important step in increasing the coupling strength between atoms and superconducting devices. With the same goal of increasing the coupling between a coplanar resonator and cold atoms, we have furthermore measured the energy of Rydberg levels in the vicinity of a metallic surface. Our measurements show that the deposition of atoms on the surface results in spatially inhomogeneous electric fields in the vicinity, which also change over time. These fields could possibly shift Rydberg atoms out of the cavity resonance and need to be accounted for in cavity QED experiments.

3.2. Outlook

Long coherence times, as they have been demonstrated in this thesis, are necessary, but not sufficient to make a quantum memory, but there are further steps involved. For a functioning quantum memory, it is necessary to efficiently write a single photon into an atomic ensemble, preserve its coherence for long storage times and then efficiently retrieve the information of this single photon. Work in this direction has been done on storing single optical photons in cold atomic gases in free fall [116] and in optical lattices [117], which reported coherence times in the ms range. By compensating the light shift in the optical lattice, it was possible to increase the coherence time to up to 0.3 s [59, 60]. All the performed experiments so far, however, suffer from very low write/retrieval efficiency, which is on the order of one percent. The goal is to increase this efficiency by strongly coupling an atomic ensemble to a superconducting resonator, which transfers the information from a superconducting

qubit to the atomic cloud. This approach is similar to experiments which used used an optical resonator to enhance the coupling between the optical field and a single atom [61] and greatly increase the efficiency in this way.

In an atom - superconductor hybrid, an atomic ensemble is to be coupled to the quantum state of a superconducting circuit using the microwave cavity as a quantum bus. As the microwave couples to the magnetic moment of the neutral atom, the interaction will be weaker as in the case of atoms coupled to the electric field of optical photons. It will not be possible to use single atoms for this, but a collective enhancement of the interaction is necessary, which scales with the square root of the number of atoms.

In the experiments reported in this thesis, the microwave cavity was not on resonance with the atoms and the transitions were driven with microwave fields from an external helicoidal antenna. Hence, the first milestone to achieve is to bring atoms into the mode volume of a microwave resonator which is close to resonance and connected to a microwave generator. As the transition between the two states $|F = 1, m_F = -1\rangle$ and $|F = 2, m_F = 1\rangle$ must be driven with a two photon transition, the resonator does not need to be strictly 'on resonance'. Ideally, however, the microwave photon has a frequency of $f_{\mathrm{MW}} = 6.8333\,\mathrm{GHz}$, corresponding to a detuning of $\Delta \approx 1\,\mathrm{MHz}$ to the intermediate state and minimize the population of other states in the transfer process. Moreover, a detuning of the cavity to an atomic transition is desirable to reduce the probability of driving the atoms by thermal photons in the resonator whenever the radiofrequency control field is switched off.

Our group is currently developing superconducting atom chips with cavities close to the atomic resonance. Furthermore, we are working on the design of resonators whose frequency can be tuned by changing the capacity or inductivity of the stripline with ferroelectric or ferromagnetic materials, respectively.

One major challenge in coupling neutral atoms to microwave cavities are the rather dismal prospects of reaching the strong coupling regime. In order to reach the strong coupling regime, the coupling strength $g/2\pi$ needs to be much larger than any loss rate κ of photons from the cavity or decay of atoms into other channels. As estimated in ref. [68], a cloud of 10^6 atoms in the mode volume of a coplanar microwave resonator would yield a collectively enhanced coupling strength of $g/2\pi = 4 \times 10^4\,\mathrm{Hz}$. To achieve strong coupling, a resonator with a quality factor of $Q = \omega/\kappa = 10^6$ is required, yielding a loss rate of $\kappa/2\pi \approx 7\,\mathrm{kHz}$. At temperatures of 4 K, the quality factor of superconducting resonators is usually limited by quasiparticle excitations (resistive losses due to unpaired electrons) to a few 10^4. A Q of one million can hence only be reached at temperatures of tens of mK.

Therefore, a second cold atom - superconductor experiment is currently being set up in Tübingen, enabling temperatures of 25 mK in a dilution refrigerator. This system will bring the regime of strong coupling within reach. Furthermore, an environment of $T = 25\,\mathrm{mK}$ makes the realization of solid state qubits feasible, whose energy splitting is sufficiently low to drive transitions between ground and excited state by the thermal bath at 4 K. So far, this experiment has an operating magneto-optical trap in a cryogenic environment (4 K) loaded from a Zeeman

slower. Currently, effort is made to load atoms into a magnetic trap and transport atoms with a magnetic conveyor to an environment at mK temperatures.

Once atoms can be strongly coupled magnetically to a superconducting resonator which is not thermally occupied, the full potential of this hybrid quantum system can be exploited, particularly the storage of a single excitation from a superconducting qubit. It will be then necessary to study the read and write efficiency of such a hybrid system as well as the coherence time. Even in the case of strong coupling and efficient state transfer between the superconducting qubit and the atoms, it is questionable if a cold atom - superconductor hybrid will ever surpass the proof-of-principle state. One problem with respect to quantum information processing is the enormous technical complexity of the system, which combines a dilution refrigerator with a complex cold atom experiment. Another difficulty in systems which rely on cold atomic gases is the long duration of a single experimental cycle needed to prepare the atomic ensemble. In our experiment, the cycle time to bring a cold cloud into the superconducting trap was approximately 30 s. It might be possible to reduce this to about 10 s, but this still cannot compete with a solid state memory, whose initialization times are negligible.

On the other hand, as atoms can be moved and it is possible to transport the ensemble after storing photons in it, cold atoms have a major advantage with respect to solid state systems. Hence, atoms could provide the possibility to serve as a transportable quantum memory. Furthermore, atoms make it possible to convert static microwave qubits into flying qubits in the form of optical photons, which can be detected on a single photon counter and transferred to other locations through optical fibers. This is one of the major goals pursued in the µK-environment.

Despite the impossibility to reach strong coupling at 4 K, the performed experiments are essential for the experiments at colder temperatures. Furthermore, even at liquid helium temperatures, interesting cavity effects can be observed. Henschel *et al.* have proposed that it is possible to cool the resonator mode using the atomic ensemble [69]. In thermal equilibrium at 4 K the cavity is occupied with $n_{\mathrm{th}} \approx 13$ photons, but it could be depleted through absorption of cavity photons by the atoms. In this context, it is also important to study the influence of thermal photons on the coherence of atomic superposition states. In the absence of a radiofrequency field, the rate of off-resonant transitions should be negligible, but the presence of a thermal microwave field could lead to an AC Zeeman shift of the two states, which will influence the relative phase evolution of the two states. If this microwave field is spatially inhomogeneous, it will lead to a decrease in Ramsey contrast, which cannot be distinguished from decoherence.

Bringing an atomic ensemble in population inversion (all atoms in F = 2) into the resonator could give rise to superradiance into the cavity. The thermal photons in the cavity can transfer atoms from state $|1\rangle$ to state $|0\rangle$. This would increase the number of photons in the cavity and hence increase the decay rate of the upper state. This results in a self-amplification of the transition strength which also scales with the square of the atom number. Superradiance should be observable in a state selective detection of the atoms as well as in the emission of a microwave

pulse from the cavity. By repumping atoms into the state $|1\rangle$, using a Raman-type transfer scheme with two lasers, it would even be possible to create a narrow-band micromaser [69].

We are also investigating the use of atoms as magnetic field sensors in the 4 K-experiment. As described in appendix A.1, superconducting rings on the chip enable trapping of quantized magnetic flux. We study the influence of the trapped flux onto the trapping geometry and investigate how parameters such as the oscillation frequencies depend on the number of flux quanta. Forthcoming experiments will expand these studies towards Josephson junctions and SQUIDs, where the number of flux quanta can be modified dynamically. Proposals have suggested that this configuration could generate macroscopic entanglement states between an atomic cloud and the discrete number of flux quanta in a SQUID-based qubit [118]. Furthermore, we will investigate the possibility to measure the magnetic moment of an atomic cloud with a SQUID, paving the way towards experiments in which not only the superconductor affects the atomic ensemble, but there is a measurable back-action of the atoms on the superconducting circuit.

The interface between cold atoms and solid state systems is a research field which is technologically challenging, yet rich in physics. The wide variety of effects, ranging from fundamental interactions to possible applications in quantum sensing and information processing, makes this hybrid system an interesting research subject for several more years, which is reflected in the ever growing number of atom-superconductor experiments over the past years.

Appendix A. Experimental Details

This appendix contains some technical details not included in the publications. Section A.1 describes the superconducting atom chip used in publication [4], section A.2 briefly presents the laser system used for the experiment.

A.1. Superconducting atom chip

A number of changes have been made to the experimental set-up since the publication of article [1]. The experimental system was upgraded by the installation of a $2D^+$-MOT [119]. Loading the magneto-optical trap from a cold atomic beam allows high loading rates ($\sim 3 \times 10^8$ atoms/s) without adversely affecting the vacuum, as the use of pulsed dispensers [120] inevitably does. This also permits trouble-free adjustment of the duration of the experimental cycle. Furthermore, the wire trap used in [2, 3] was replaced by a microstructured chip (see Fig. A.1). The chip contains various niobium thin film structures, which were deposited by magnetron sputtering on a 330 µm thick monocrystalline sapphire substrate and patterned with optical lithography and reactive SF_6 ion etching [121]. The niobium film has a thickness of 500 nm.

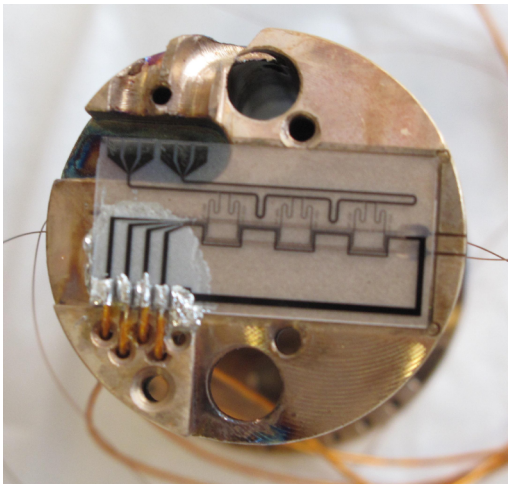

Figure A.1.: The superconducting chip on the copper mount. The chip is attached by ultrasonic soldering below the lead connections.

The implementation of this chip into the existing experimental set-up posed a number of challenges. Attaching the sapphire with thermally conductive and UHV compatible epoxy was not sufficient to cool the chip to temperatures below 9.2 K. The thermal conductivity of the glue at low temperatures was not sufficient to lead away the heat input by black body radiation and the electrical leads. Even the replacement of the supply wires with conductors of 100 µm diameter (minimizing the heat flow from the room temperature part) and very thin electrical insulation (15 µm Kapton), which were mechanically fixed to the cryostat at several temperature stages with metallic clamps (see fig. A.2), did not yield the desired result. Only by replacing the glue by flux-free solder alloy and direct ultrasonic soldering [122] of the sapphire to the copper holder could the

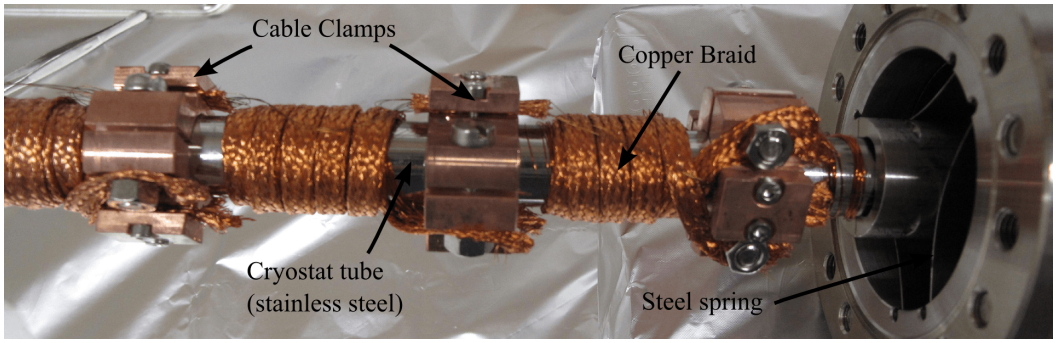

Figure A.2.: Photograph of the cryostat assembly. Mechanical clamping of the insulated current leads and contact to a copper braid was necessary to cool the Kapton insulated wires. Clamping of the cryostat to the outer vacuum tube with steel leaf springs was necessary to reduce mechanical vibrations of the chip.

desired thermal conductivity be achieved (see Fig. A.1). We measured a critical temperature of $T \approx 9.0\,\mathrm{K}$, suggesting a small temperature gradient between the chip surface and the helium reservoir. Measurements of the electric properties of the thin film structures yielded critical current densities of up to $5 \times 10^6\,\mathrm{A/cm}$.

The niobium structures on the chip are shown in Fig. A.3. The chip includes four trapping wires, which are 15, 30, 50, and 100 µm wide and shaped in several z-forms, allowing to generate traps at different locations on the chip. The largest wire can be driven with currents of up to 1 A and is used to load atoms from the optical dipole trap far from the chip surface. The smallest wires are implemented to reduce the impact of the Meissner effect and hence allow trapping of the atoms close to the chip surface. All of the current carrying wires are connected to a common ground lead. Additional axial confinement of the magnetic traps can be ensured by a pair of superconducting wires (NbTi in a Cu matrix) below the chip, running perpendicular to the trap axis. The confinement wires are visible through the chip in figure A.1.

The chip comprises several superconducting structures on which experiments can be performed. Superconducting microwave resonators of different lengths have been structured on the chip, whose ends are located next to the smallest trapping wires. The resonators were designed in a quarter-wave cavity configuration. At the end of the resonator which is close to the trapping region, the central conductor is connected to the ground planes, yielding a minimum of the electric field and a maximum of the magnetic field in order to maximize the coupling to the magnetic moment of the atoms. The resonators were designed with very narrow ground planes (15 µm) in order to facilitate magnetic transport of atoms into the gap despite of the influence of the Meissner effect. The resonator gap was chosen to be 10 µm wide, the width of the central conductor was adapted to 33 µm to match the impedance of the resonator to 50 Ω. In total, six of these resonators of different lengths were put onto the chip, because it was not possible to perfectly predict the frequency of the

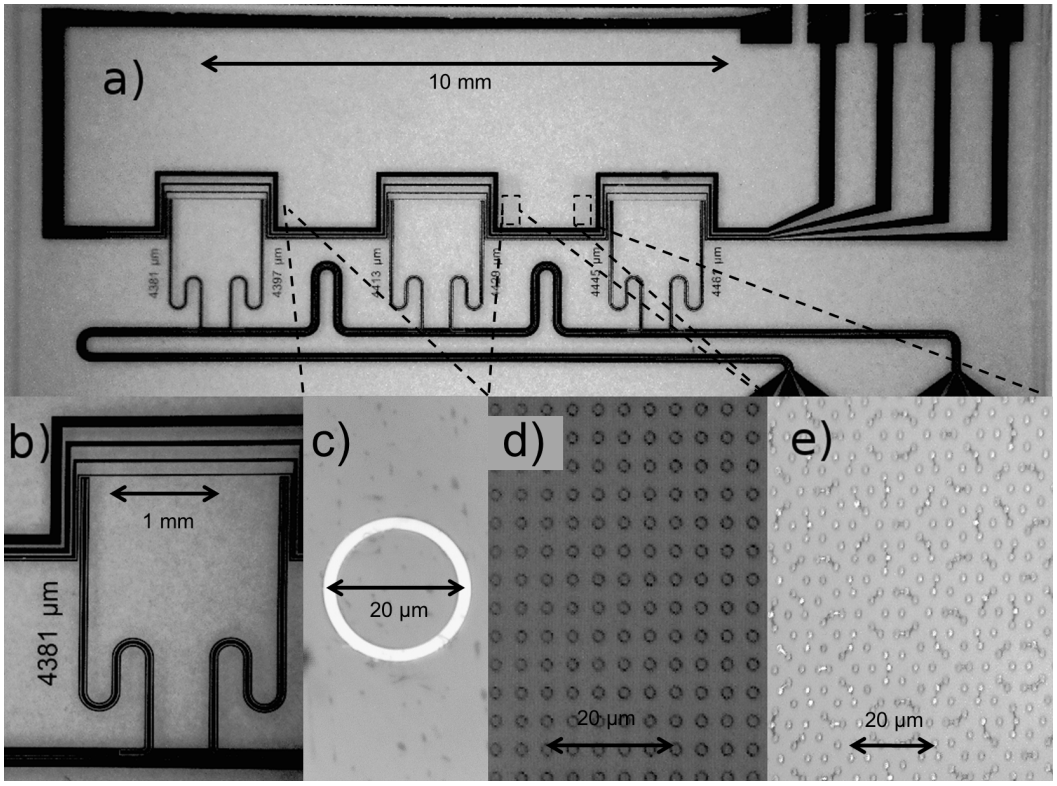

Figure A.3.: Overview and details of the superconducting chip. The angular structures visible at the top are the current-carrying wires for the generation of magnetic traps, the curved lines below are the microwave resonators and the feed line they are connected to. b) Two microwave resonators in detail. The capacitive coupling to the feed line gives rise to a node of the magnetic field, the short between center conductor and ground plane to an antinode of the magnetic field. c) Superconducting ring for the study of flux quantization. d) Square lattice and e) Penrose tiling of superconducting pillars.

resonators. The goal was to achieve one resonator with a resonance frequency of $f \approx 6.83\,\mathrm{GHz}$. All six resonators are capacitively connected to a common microwave feedline, which in principle makes readout of all six resonators possible. However, due to the thin ground planes and the presence of the trapping wires nearby, cross-talk between the different structures made the identification of single resonances impossible. For this reason, the resonators were left unconnected in the experiments described in section 2.4. Future chips will include single microwave resonators with frequencies matched to the atomic resonance or the possibility to tune the frequency.

The microwave cavities are not the only structures on the chip. Superconducting rings of 20 µm diameter allow trapping of magnetic flux, if they are cooled through the superconducting transition in an applied field. The flux in the ring is quantized and needs to be an integer multiple of the magnetic flux quantum $\Phi_0 = 2.068 \times 10^{-15}\,\mathrm{Wb}$. The goal in these experiments is the study of this flux

quantization using cold atoms as a probe and is related with proposals of entangling an atomic cloud with a superposition state of magnetic flux in such a ring [118] or coupling atoms to a superconducting quantum interference device (SQUID) [123]. On the chip, there are single rings as well as a chain of adjacent rings, which permit the study of one-dimensional periodic magnetic potentials. A further step in this direction are the periodic and quasi-periodic structures which were included on the chip. The periodic structure consists of niobium pillars with 1 µm radius, which are arranged in a square lattice of 4 µm pillar distance. In another structure, these pillars are arranged according to a Penrose tiling with the same pillar density. In an applied magnetic field, the Meissner effect in these two arrangements will give rise to a (quasi-)periodic modulation of the magnetic field, which is to be investigated by matter-wave diffraction of a Bose-Einstein condensate [124]. So far, only the coplanar resonator structures have been used for experiments, which are described in chapter 2.4.

A.2. Laser system

As there have been substantial changes to the laser system with respect to [103, 125], the set-up will be described briefly in this section. All lasers needed for cooling and imaging of ^{87}Rb (see Fig. A.4) are frequency stabilized with respect to a reference laser, which is locked to the $5S_{1/2}$, F = 1 → $5P_{3/2}$, F' = 1/F' = 2 crossover by frequency modulation spectroscopy [126, 127]. We use a grating stabilized diode laser

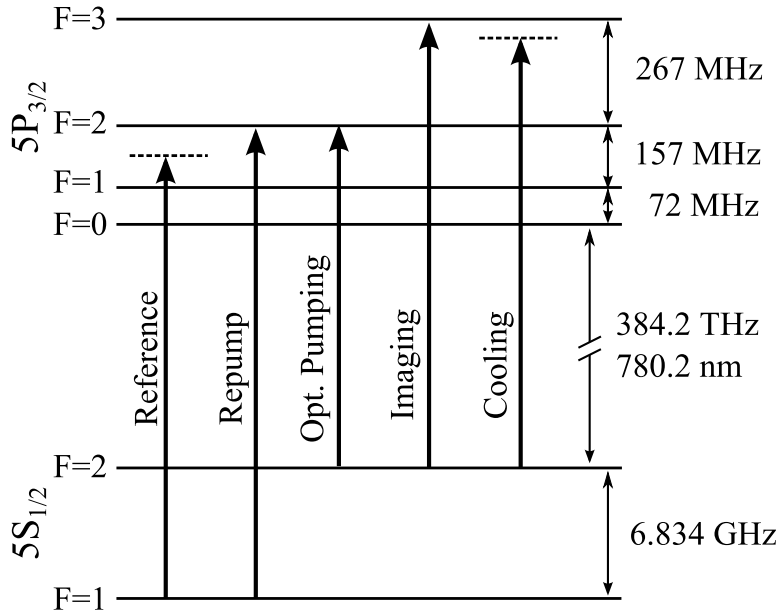

Figure A.4.: Laser frequencies used in the experimental cycle. The reference laser is locked to the F = 1/F = 2 crossover. The detuning of the cooling laser to the F = 3 level is 17 MHz.

in Littrow-configuration (Topica DL Pro 100) for this task. A radio frequency of 30 MHz is directly modulated onto the diode current. The error signal obtained from the spectroscopy is controlled to zero with a double-integrator regulation[1]. The fast signal is acting on the laser current, the integration with slow time constants is fed to a piezo which moves the grating.

Only a small fraction of the light is used for the spectroscopy, most of it is frequency shifted to the $5S_{1/2}$, F = 1 → $5P_{3/2}$, F' = 2 transition with a 78.5 MHz acousto-optical modulator and used for repumping atoms from the F=1 ground state into the cooling cycle. The repumping light is used for the MOT, the $2D^+$-MOT and to pump atoms into the F=2 ground state before imaging.

Another small part of the reference light is used to stabilize the imaging laser (Topica DL Pro 100) to the $5S_{1/2}$, F = 2 → $5P_{3/2}$, F' = 3 transition. The two lasers are superimposed on a fast photo diode where they produce a beating signal of

[1] Designed by Dr. Simon Bernon

$f_{\text{beat}} = 6.49\,\text{GHz}$. This signal is mixed with a 6.80 GHz reference signal from a local oscillator, resulting in a down-converted beating frequency of 310 MHz. This signal is sent to a frequency-to-voltage converter[2], which allows for regulation of the error signal with the double integration mentioned above and hence frequency-locking of this laser with respect to the reference.

This laser delivers three different frequencies: for imaging, optical pumping, and for referencing the cooling laser. A part of the light is shifted by -133 MHz with an AOM and subsequently split on a polarizing beam splitter. One of the beams is shifted by another -133 MHz, ending up with light resonant on the $5S_{1/2}$, F = 2 $\rightarrow$ $5P_{3/2}$, F' = 2 transition, which is used for optical pumping. The other beam is shifted by +133 MHz to be on the F = 2 $\rightarrow$ $5P_{3/2}$, F' = 3 transition again. The rather complex procedure of going through AOMs of opposite frequency shift is necessary because the AOMs are also used for switching on and off the laser on short timescales. Another beam from the laser is shifted by -267 MHz and gives the reference for the master laser of a tapered amplifier (Toptica TA pro, 1 W max. power). These two lasers are locked to a beating frequency of 250 MHz, yielding a cooling laser frequency 17 MHz ($\sim 3\Gamma$) below the $5S_{1/2}$, F = 2 $\rightarrow$ $5P_{3/2}$, F' = 3 transition. The master laser injects the tapered amplifier, which is set to deliver about 120 mW of cooling laser for the MOT after an optical fiber. Furthermore, the master laser injects a self-built diode laser (Sharp GH0781JA2C, 120 mW) providing the cooling light for the $2D^+$-MOT ($P \approx 45\,\text{mW}$ after the fiber).

[2]Developed by PD Dr. Martin Brendle

Appendix B. Measuring atomic coherence

B.1. Atomic qubit states

The idea of using atomic clouds as a memory for quantum information processing is based on the fact that atoms trapped in a vacuum chamber interact extremely weakly with their environment, which makes them only little susceptible for decoherence. However, there are additional requirements that the system we consider has to fulfill. First of all, we need a qubit state $|\Psi\rangle = c_0 |0\rangle + c_1 |1\rangle$, whose coherence properties we can investigate. This means that it must be possible to reduce the complex level structure of the atom to an effective two-level system. This works very well in the case of rubidium, whose hyperfine structure levels experience Zeeman splitting in an external field. In our experiment we would like to use the states $5S_{1/2}(F = 1, m_F = -1) := |0\rangle$ and $5S_{1/2}(F = 2, m_F = 1) := |1\rangle$ as qubit states, which have an energy splitting of $\Delta E/\hbar \approx 6.834\,\mathrm{GHz}$. These two levels have the same linear Zeeman shift $\Delta E/\hbar B = 0.7\,\mathrm{MHz/G}$, so their relative energy shift is only given by the quadratic Zeeman shift [128]. In a magnetic field of $B_\mathrm{m} = 3.23\,\mathrm{G}$, the so-called *magic* offset field, this differential Zeeman shift is minimized and can be calculated by the Breit-Rabi formula to be $\Delta E_\mathrm{diff}/\hbar = \beta \cdot (B - B_\mathrm{m})^2$, $\beta = 431\,\mathrm{Hz/G^2}$ [108].

In order to drive transitions between the states $|0\rangle$ and $|1\rangle$, two photons are necessary (as $\Delta m_F = 2$, see level scheme in Fig. B.3). In the experiment, this transition is driven by a combined excitation using one microwave ($\nu_\mathrm{MW} \approx 6.833378\,\mathrm{GHz}$) and one radio frequency photon ($\nu_\mathrm{RF} \approx 1.300\,\mathrm{MHz}$). If the detuning Δ of the two driving fields to the intermediate level (which can be the state $F = 1, m_F = 0$ or the state $F = 2, m_F = 0$) is larger than the Rabi frequencies Ω_MW and Ω_RF, the occupation probability of this level is negligible. After adiabatic elimination (see appendix B.2.2) one obtains an effective two-photon Rabi frequency of $\Omega = \Omega_\mathrm{MW}\Omega_\mathrm{RF}/2\Delta$ [129]. In the experiment, the irradiated microwave and radio frequency powers ($P_i \propto \Omega_i^2$) were chosen to yield a Rabi frequency of $\Omega/2\pi \approx 500\,\mathrm{Hz}$ - $1\,\mathrm{kHz}$ for a detuning of $\Delta = 960\,\mathrm{kHz}$. For the Rabi oscillations (see fig. B.1), we measured a contrast of about 0.95 and damping on the order of 20 ms, which we attribute to an inhomogeneity of the Rabi frequency over the size of the cloud.

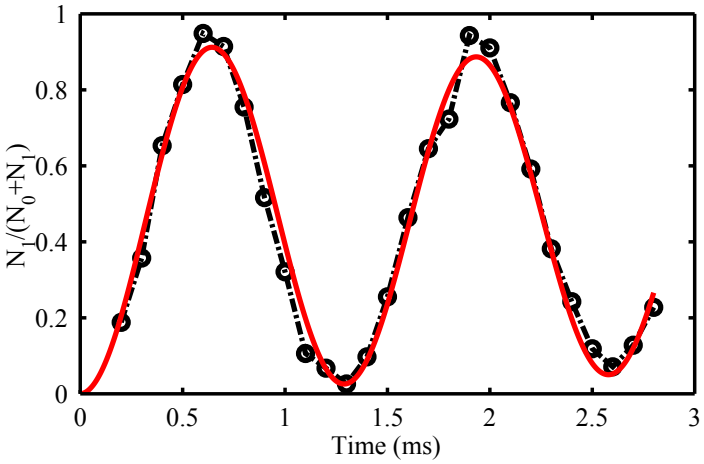

Figure B.1.: Two-photon Rabi oscillation with $\Omega/2\pi = 775\,\mathrm{Hz}$, contrast of 0.93 and a damping time of $T_{\mathrm{damp}} = 22.4\,\mathrm{ms}$.

B.2. One- and two-photon transitions

In this section, we will demonstrate how a three-level system can be reduced to an effective two-level system. Starting with the formalism of single photon Rabi oscillations, we will then do the adiabatic elimination of the intermediate level for a two-photon transition. The derivation of the transition equations is based on [129] and the lecture notes [130].

B.2.1. Two-level system

For the easiest case of a two level system $|i\rangle$ and $|f\rangle$ in the presence of a driving field $\Omega\cos\omega t$, the Hamiltonian can be written as:

$$H = \begin{pmatrix} E_i & \hbar\Omega\cos\omega t \\ \hbar\Omega\cos\omega t & E_f \end{pmatrix}, \tag{B.1}$$

where E_i and E_f are the energies of the levels $|i\rangle$ and $|f\rangle$, respectively. We can now arbitrarily set the energy $E_i = 0$, substitute $E_f - E_i = \hbar\omega_{if}$ and replace $\cos\omega t = \frac{1}{2}\left(e^{i\omega t} + e^{-i\omega t}\right)$, which yields

$$H = \begin{pmatrix} 0 & \hbar\Omega\frac{1}{2}\left(e^{i\omega t} + e^{-i\omega t}\right) \\ \hbar\Omega\frac{1}{2}\left(e^{i\omega t} + e^{-i\omega t}\right) & \hbar\omega_{if} \end{pmatrix}. \tag{B.2}$$

The wavefunction of the state can be expressed as a linear combination of its basis states

$$\Psi(t) = c_i \begin{pmatrix} 1 \\ 0 \end{pmatrix} + c_f \begin{pmatrix} 0 \\ 1 \end{pmatrix} e^{-i\omega_{if}t}, \tag{B.3}$$

which we can use in the Schrödinger equation

$$i\hbar\dot{\Psi}(t) = H\Psi(t) \tag{B.4}$$

to obtain the time derivative of the coefficients:

$$\dot{c_i} = -i\frac{\Omega}{2}\left(e^{i(\omega-\omega_{if})t} + e^{-i(\omega+\omega_{if})t}\right)c_f \tag{B.5a}$$

$$\dot{c_f} = -i\frac{\Omega}{2}\left(e^{-i(\omega-\omega_{if})t} + e^{i(\omega+\omega_{if})t}\right)c_i. \tag{B.5b}$$

We now make the rotating wave approximation (RWA), in which we neglect the terms oscillating with $\omega + \omega_{if}$, and consider a small detuning $\Delta = \omega - \omega_{if} \ll \omega$, which yields

$$\dot{c_i} = -i\frac{\Omega}{2}e^{i\Delta t}c_f \tag{B.6a}$$

$$\dot{c_f} = -i\frac{\Omega}{2}e^{-i\Delta t}c_i. \tag{B.6b}$$

If we solve the second equation for c_i, we can take its derivative and equate it with the first one to obtain the differential equation

$$\ddot{c_f} + i\Delta\dot{c_f} + \frac{\Omega^2}{4}c_f = 0, \tag{B.7}$$

which is solved by the ansatz $c_f = \alpha e^{-\beta t}$ and yields the solutions

$$\beta_{+,-} = \frac{\Delta \pm \sqrt{\Delta^2 + \Omega^2}}{2} = \frac{\Delta \pm \tilde{\Omega}}{2}. \tag{B.8}$$

If we insert this into the general form $c_f = \alpha_+ e^{-\beta_+ t} + \alpha_- e^{-\beta_- t}$ and use the starting conditions $c_i(t=0) = 1$, $c_f(t=0) = 0$, we arrive at the population probability of the excited state:

$$c_f c_f^* = \frac{\Omega}{\tilde{\Omega}}\sin^2(\frac{\tilde{\Omega}}{2}t), \tag{B.9}$$

which is the well known equation for the Rabi oscillation.

B.2.2. Three levels

Let's now switch to the case of a three-level system $|i\rangle$, $|a\rangle$, and $|f\rangle$, where $|a\rangle$ is the intermediate level to be eliminated (Fig. B.2a). If we consider the interaction

of these levels with two driving fields $\Omega_1 \cos(\omega_1 t)$ and $\Omega_2 \cos(\omega_2 t)$, we obtain the Hamiltonian:

$$H = \begin{pmatrix} E_i & \hbar\Omega_1 \cos\omega_1 t & 0 \\ \hbar\Omega_1 \cos\omega_1 t & E_a & \hbar\Omega_2 \cos\omega_2 t \\ 0 & \hbar\Omega_2 \cos\omega_2 t & E_f \end{pmatrix} \tag{B.10}$$

With

$$E_i = 0 \tag{B.11a}$$
$$E_a = \hbar\omega_{ia} \tag{B.11b}$$
$$E_f = \hbar\omega_{if} = \hbar(\omega_{ia} + \omega_{af}) \tag{B.11c}$$

and by using the mathematical identity

$$\cos\omega_\alpha t = \frac{1}{2}\left(e^{i\omega_\alpha t} + e^{-i\omega_\alpha t}\right) \tag{B.12}$$

the Hamilton operator is of the form

$$H = \hbar \begin{pmatrix} 0 & \frac{\Omega_1}{2}\left(e^{i\omega_1 t} + e^{-i\omega_1 t}\right) & 0 \\ \frac{\Omega_1}{2}\left(e^{i\omega_1 t} + e^{-i\omega_1 t}\right) & \omega_{ia} & \frac{\Omega_2}{2}\left(e^{i\omega_2 t} + e^{-i\omega_2 t}\right) \\ 0 & \frac{\Omega_2}{2}\left(e^{i\omega_2 t} + e^{-i\omega_2 t}\right) & \omega_{if} \end{pmatrix}. \tag{B.13}$$

The wavefunction of the state is of the form

$$\Psi(t) = c_i \begin{pmatrix} 1 \\ 0 \\ 0 \end{pmatrix} + c_a \begin{pmatrix} 0 \\ 1 \\ 0 \end{pmatrix} e^{-i\omega_{ia} t} + c_f \begin{pmatrix} 0 \\ 0 \\ 1 \end{pmatrix} e^{-i\omega_{if} t}, \tag{B.14}$$

and the time derivative is

$$\dot{\Psi}(t) = \dot{c_i} \begin{pmatrix} 1 \\ 0 \\ 0 \end{pmatrix} + \begin{pmatrix} 0 \\ 1 \\ 0 \end{pmatrix} e^{-i\omega_{ia} t}(\dot{c_a} - ic_a\omega_{ia}) + \begin{pmatrix} 0 \\ 0 \\ 1 \end{pmatrix} e^{-i\omega_{if} t}(\dot{c_f} - ic_f\omega_{if}). \tag{B.15}$$

If we insert this into the equation

$$i\hbar\dot{\Psi}(t) = H\Psi(t) \tag{B.16}$$

we obtain the following derivatives of the coefficients:

$$\dot{c_i} = -i\frac{\Omega_1}{2} c_a \left(e^{i(\omega_1 - \omega_{ia})t} + e^{-i(\omega_1 + \omega_{ia})t}\right) \tag{B.17a}$$
$$\dot{c_a} = -i\frac{\Omega_1}{2} c_i \left(e^{-i(\omega_1 - \omega_{ia})t} + e^{i(\omega_1 + \omega_{ia})t}\right) - i\frac{\Omega_2}{2} c_f \left(e^{i(\omega_2 - \omega_{af})t} + e^{-i(\omega_2 + \omega_{af})t}\right) \tag{B.17b}$$
$$\dot{c_f} = -i\frac{\Omega_2}{2} c_a \left(e^{i(\omega_2 + \omega_{af})t} + e^{-i(\omega_2 - \omega_{af})t}\right), \tag{B.17c}$$

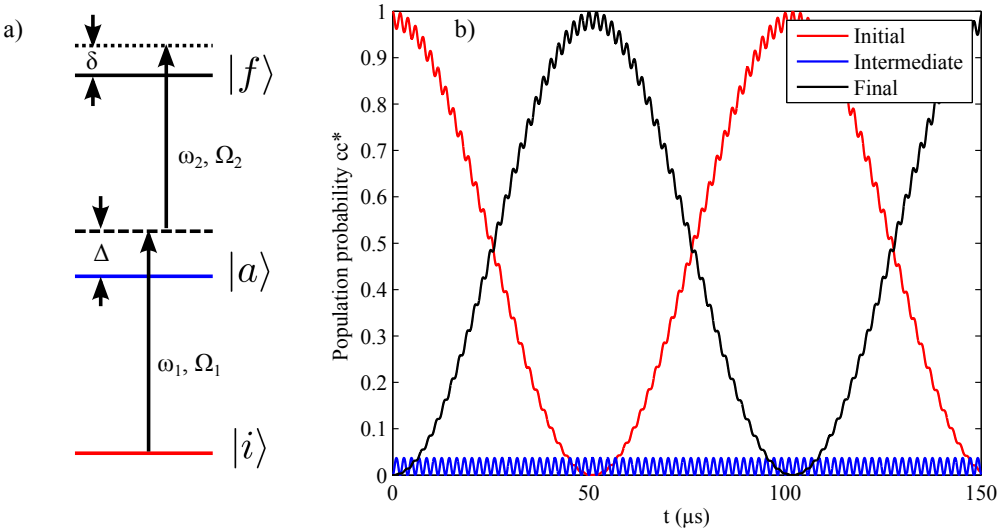

Figure B.2.: a) Three-level system in the presence of two driving fields. The notation is based on [129]. We seek to eliminate the intermediate level from the calculations. b) Numerical simulation of the population probability of the three levels for $\Omega_1 = \Omega_2 = 2\pi \cdot 100\,\mathrm{kHz}$, $\Delta = 2\pi \cdot 500\,\mathrm{kHz}$, and $\delta = 0$. As it can be seen, for small times, we can consider c_i and c_f as constant. For a large detuning Δ, the population probability of intermediate state is very small.

where we have used $\omega_{af} = \omega_{if} - \omega_{ia}$. By making the substitutions

$$\omega_1 - \omega_{ia} = \Delta \tag{B.18a}$$
$$\omega_2 - \omega_{af} = \delta - \Delta, \tag{B.18b}$$

we arrive at the final form of the differential equations:

$$\dot{c_i} = -i\frac{\Omega_1}{2} c_a e^{i\Delta t} \tag{B.19a}$$
$$\dot{c_a} = -i\frac{\Omega_1}{2} c_i e^{-i\Delta t} - i\frac{\Omega_2}{2} c_f e^{i(\delta-\Delta)t} \tag{B.19b}$$
$$\dot{c_f} = -i\frac{\Omega_2}{2} c_a e^{-i(\delta-\Delta)t}, \tag{B.19c}$$

where we have made the rotating wave approximation. If $\Delta \gg \Omega_1, \Omega_2, \delta$, the population probability of the intermediate state $|a\rangle$ will be very small and c_a will be varying quickly. The changes of c_i and c_f will be negligible and we can assume them to be constant (see fig B.2b). Making this ansatz, we can integrate $\dot{c_a}$, and obtain

$$c_a = \int \dot{c_a}\,\mathrm{d}t = \frac{\Omega_1}{2\Delta} c_i e^{-i\Delta t} + \frac{\Omega_2}{2(\delta-\Delta)} c_i e^{i(\delta-\Delta)t}, \tag{B.20}$$

which we plug into the equations B.19b and B.19c:

$$\dot{c_i} = -i\frac{\Omega_1^2}{4}c_i - i\frac{\Omega_1\Omega_2}{4}c_f e^{i\delta t} \tag{B.21a}$$

$$\dot{c_f} = -i\frac{\Omega_2^2}{4}c_f - i\frac{\Omega_1\Omega_2}{4}c_i e^{-i\delta t} \tag{B.21b}$$

We have neglected the δ term in the denominator, as it is much smaller than Δ. The solution of these coupled differential equations is similar to the one of the two-level system (which is why we have presented this calculation in detail). Again we solve B.21b for c_i, take its derivative and compare it to B.21a. Then we make the ansatz $c_f = \alpha e^{-\beta t}$, which leads to a quadratic equation with the two solutions:

$$\beta_{+,-} = -\frac{1}{2}\left(\delta + \Omega_0 \pm \sqrt{(\delta+\Omega_0)^2 - \frac{\Omega_2^2\delta}{\Delta}}\right) \tag{B.22}$$

where we have used

$$\Omega_0 = \frac{\Omega_1^2}{4\Delta} + \frac{\Omega_2^2}{4\Delta}, \tag{B.23}$$

following the notation in [129]. This leads us, after a somewhat lengthy conversion to

$$\beta_{+,-} = -\frac{1}{2}\left(\delta + \Omega_0 \pm \tilde{\Omega}\right), \tag{B.24}$$

with

$$\begin{aligned}\tilde{\Omega} &= \sqrt{\left(\frac{\Omega_1\Omega_2}{2\Delta}\right)^2 + \left(\delta + \frac{\Omega_1^2 - \Omega_2}{4\Delta}\right)^2} \\ &= \sqrt{\quad \Omega_{\text{eff}}^2 \quad + \quad \Delta_{\text{eff}}^2}.\end{aligned} \tag{B.25}$$

The starting conditions $c_i(t=0) = 1$, $c_f(t=0) = 0$ lead us to the population probability of the excited state:

$$c_f c_f^* = \frac{\Omega_{\text{eff}}}{\tilde{\Omega}}\sin^2(\frac{\tilde{\Omega}}{2}t), \tag{B.26}$$

which now is exactly the equation for a two-level Rabi oscillation, with the effective Rabi frequency

$$\Omega_{\text{eff}} = \frac{\Omega_1\Omega_2}{2\Delta} \tag{B.27}$$

and an effective detuning of

$$\Delta_{\text{eff}} = \delta + \frac{\Omega_1^2 - \Omega_2^2}{4\Delta}. \tag{B.28}$$

The last term in Δ_{eff} shifts the levels out of resonance, if the Rabi frequencies are different. This term is for optical fields known as light shift, or for electric fields

as AC Stark shift. As the transitions in this thesis are due to magnetic dipole transitions, we can analogously speak of an AC Zeeman shift.

The three-level system is still not covering the whole physics in the transition between the $|F = 1, m_F = -1\rangle$ and the $|F = 2, m_F = 1\rangle$ ground states of rubidium. A rigorous analysis of the transition, including all eight Zeeman sublevels, yields an effective Rabi frequency, which in first order is proportional to the product of the two single photon Rabi frequencies divided by the detuning. However, the result for the AC Zeeman shift strongly disagrees with the result above [131]. To lowest order, there is only a microwave shift

$$\Delta_{\text{eff}} \approx \frac{\Omega_{\text{MW}}^2}{2\Delta}. \tag{B.29}$$

The reason for this is that both the $|F = 1, m_F = -1\rangle$ and the $|F = 2, m_F = 1\rangle$ state experience the same radiofrequency shift as a result of their off-resonant coupling to their neighboring states.

B.3. The Bloch sphere

The two-level system $c_0 |0\rangle + c_1 |1\rangle$ introduced above can be described as a spin 1/2 in a magnetic field, a system widely use in nuclear magnetic resonance (NMR) experiments. For such a spin system, the projection of the spin onto the magnetic field axis can take two values, which have a different potential energy. The spin is best described in the picture of the Bloch sphere, which in a classical picture gives an exact representation of the magnetization vector in NMR. The equivalence of a two-level system and the representation on the Bloch sphere has first been shown by Feynman, Vernon and Hellwarth [132], introductions can be found in many textbooks, for example [133, 134]. The fact that $|c_0|^2 + |c_1|^2 = 1$ makes it easy to see that the state can be represented geometrically on a sphere with radius $r = 1$, in which case we have to use the angles θ and φ as coefficients. In this picture, the state $|0\rangle$ is the south pole, the state $|1\rangle$ the north pole of the sphere. An arbitrary state can be expressed in Cartesian coordinates as:

$$\begin{aligned} x &= c_0 c_1^* + c_1 c_0^* \\ y &= i(c_0 c_1^* - c_1 c_0^*) \\ z &= c_1 c_1^* - c_0 c_0^*, \end{aligned} \tag{B.30}$$

following the notation of [134]. The coefficients c_0 and c_1, which define the state $|\Psi\rangle$, can be expressed in polar coordinates by

$$\begin{aligned} c_0 &= \sin(\theta/2) \\ c_1 &= e^{i\varphi} \cos(\theta/2). \end{aligned} \tag{B.31}$$

The Bloch vector rotates around the z-axis with a constant frequency, which corresponds to the energy difference between the two levels $\omega_0 = (E_1 - E_0)/\hbar$. When we

apply an external frequency $\omega \gg \omega - \omega_0$ in order to drive transitions, it is therefore a convenient choice to consider the system in a coordinate system rotating with angular frequency ω and neglect any rapidly changing terms at $2\omega_0$. In such a system, the state vector precesses around the z-axis with a frequency of $\delta = \omega - \omega_0$. The application of an external frequency pulse rotates the state around the x- or the y-direction. After a $\pi/2$-pulse, the system is in a superposition of states $|0\rangle$ and $|1\rangle$ with equal population probability of the two states. In the Bloch picture, the state is transferred into the x-y-plane, in which it rotates with frequency δ.

B.4. Ramsey-Interferometry

The spin coherence of a superposition state is explored by means of Ramsey interferometry. This method was introduced by Norman Ramsey under the name of separated oscillatory fields method [135] and is the foundation of the atomic clock. The atomic ensemble is brought into the state $|\Psi\rangle = 1/\sqrt{2}(|0\rangle + |1\rangle)$ with a $\pi/2$-pulse at a time $t = 0$[1]. Let's assume, the $\pi/2$-pulse rotates the state by 90° around the y-axis on the Bloch sphere. After the pulse, the state is given by the two angles $\theta = \pi/2$ and $\varphi = 0$, or, in cartesian Coordinates:

$$|\Psi(t=0)\rangle = \begin{pmatrix} 1 \\ 0 \\ 0 \end{pmatrix} = \begin{pmatrix} \cos\pi/2 & 0 & -\sin\pi/2 \\ 0 & 1 & 0 \\ \sin\pi/2 & 0 & \cos\pi/2 \end{pmatrix} \cdot \begin{pmatrix} 0 \\ 0 \\ -1 \end{pmatrix} \tag{B.32}$$

In the frame rotating with $\omega = \omega_{\mathrm{MW}} + \omega_{\mathrm{RF}}$, the vector of the atomic systems precesses in the x-y-plane of the Bloch sphere with the angular frequency $\delta = \omega_0 - \omega$, which yields the state

$$|\Psi(t)\rangle = \begin{pmatrix} \cos\delta t \\ \sin\delta t \\ 0 \end{pmatrix}. \tag{B.33}$$

After a time T_{R}, the state has rotated in the plane by an angle $\varphi = \delta \cdot T_{\mathrm{R}}$. A second $\pi/2$-pulse rotates the vector of the atomic state by 90° about the y axis again:

$$|\Psi(T_{\mathrm{R}})\rangle = \begin{pmatrix} 0 \\ \sin\delta T_{\mathrm{R}} \\ \cos\delta T_{\mathrm{R}} \end{pmatrix} \tag{B.34}$$

In spherical coordinates, we obtain the angles $\theta = \delta T_{\mathrm{R}}$ and $\varphi = \mathrm{sgn}(\sin\delta T_{\mathrm{R}})$, which leads us to the coefficients

$$\begin{pmatrix} c_0 \\ c_1 \end{pmatrix} = \begin{pmatrix} \sin(\delta T_{\mathrm{R}}/2) \\ e^{\pm 1}\cos(\delta T_{\mathrm{R}}/2) \end{pmatrix}. \tag{B.35}$$

[1] For the sake of simplicity we neglect the length of the pulse, which is much smaller than the interrogation time T_R

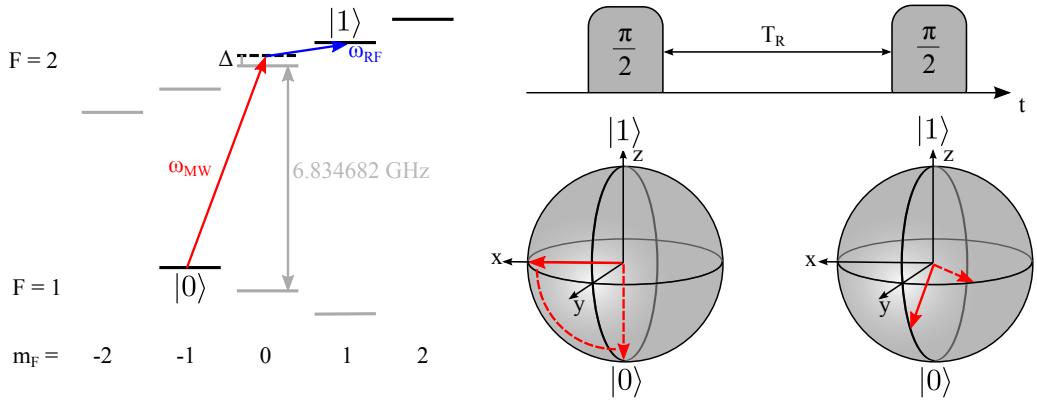

Figure B.3.: *Left*: Level structure of the ^{87}Rb ground state in a magnetic field. The states with black lines can be trapped magnetically, the grey ones not. We prepare atoms in the $|0\rangle = |F = 1, m_F = -1\rangle$ state. A two-photon transition brings the atom into the state $|1\rangle = |F = 2, m_F = 1\rangle$, which is used because it has in first order the same Zeeman shift as $|0\rangle$, making these clock states almost insensitive to magnetic fields. *Right*: Ramsey interrogation scheme and its representation on the Bloch sphere. The first $\pi/2$-pulse rotates the population around the (arbitrarily chosen) y-axis from $|0\rangle$ (dashed arrow) into a superposition $1/\sqrt{2}(|0\rangle + |1\rangle)$ (solid red arrow). In a coordinate system which rotates with the driving frequency $\omega = \omega_{\mathrm{MW}} + \omega_{\mathrm{RF}}$, the vector precesses in the horizontal plane with the difference frequency between the atomic frequency and the driving frequency $\delta = \omega - \omega_0$. After an interrogation time T_{R}, a second pulse rotates the population 90° about the x-axis again. Subsequently, we measure the population of the basis states $|0\rangle$ and $|1\rangle$ by state selective absorption imaging.

Depending on the angle $\delta T_{\mathrm{R}}/2$ of the rotating vector to the y-axis, one obtains a different population of the two states after the second pulse. For a Ramsey measurement with N_{tot} atoms, we measure

$$N_1 = N_{\mathrm{tot}} \cdot c_1 c_1^* = \frac{N_{\mathrm{tot}}}{2} \left(1 + \cos(\delta T_{\mathrm{R}})\right) \tag{B.36}$$

atoms in the excited state if the detuning $\delta = \omega_0 - \omega$ is sufficiently small to fulfill the conditions for a $\pi/2$-pulse.

In the case of decoherence, the spins dephase with respect to each other. In the Bloch picture, the individual spins in the x-y-plane will not be aligned along the direction of the average spin vector anymore. As a consequence, the length of this vector will decrease, leading to a damping of the Ramsey oscillation amplitude with increasing time T_{R}.

B.4.1. Mechanisms of dephasing and decoherence

In a Ramsey type experiment with cold atoms there are several mechanisms which all lead to a decay of the Ramsey contrast. In an experiment with trapped atoms, the two most important sources that cause the spins to dephase are the position

dependency of the magnetic field and the density dependent shift of the transition frequency. The first mechanism stems from the fact that the atoms are trapped in a minimum of magnetic potential, so there has to be spatially varying magnetic field. Due to the differential Zeeman shift, the curvature of the potential does not look equally for the two states, and there will be a spatially varying clock frequency. An atom with higher kinetic energy will be able to further climb up the potential than one at the lower end of the Boltzmann distribution. Hence, the two atoms will dephase with respect to each other [136]. For a cloud at T = 500 nK in a trap with the magic offset field $B_{\mathrm{m}} = 3.23\,\mathrm{G}$, the differential shift over the size of the cloud is on the order of 1 Hz [108].

A different shift of the two states arises from atomic collisions. If the de-Broglie wavelength of the atoms is larger than their scattering length (s-wave regime), the shift of each state can be expressed in form of a mean field interaction merely depending on the scattering length a_{ij} [108]. As the two states have slightly different scattering lengths [137, 138] and the density varies across the cloud, we again obtain a spatially varying clock frequency. The density dependent shift is proportional to the atomic density n and can be calculated to $\Delta\nu_{\mathrm{coll}} = n \cdot (-4 \times 10^{-13})\,\mathrm{cm}^3/\mathrm{s}$.

As the mean field shift is always negative, there is a regime $B < B_{\mathrm{m}}$, where the collisional shift partly compensates the differential Zeeman shift. In this regime, the dephasing of the two states is minimized and one can obtain coherence times of 2-3 s [108, 109] without the use of any spin echo techniques.

B.4.2. Spin self-rephasing

In two recent experiments, researchers have observed coherence on timescales far beyond the 3 s stated above. These coherence times are a result of spin self-rephasing collisions [110, 111]. The underlying mechanism has been described before under the name "identical spin rotation effect" (ISRE) [139, 140]. If we consider two atoms oscillating along the same axis in the trapping potential, which have different kinetic energies, they will accumulate a phase difference, i.e. the two spins separate on the Bloch sphere. If these two atoms collide and scatter in the forward direction, i.e. the direction they both move in, they do not change their velocity class, but their spins are rotated about the sum axis. This is a consequence of the indistinguishability of the two identical particles participating in this collision [141]. As a result, the spin of the faster atom will catch up with the slower one some time after the collision. The effect is the same as in a spin echo experiment, but without the need for any pulse sequences. Moreover, the self-rephasing is a continuous effect: the atoms exchange their spin whenever they go through a forward collision.

There are a few conditions that need to be satisfied to obtain self-rephasing. First, the rate at which this spin rotation occurs, $\omega_{\mathrm{ex}}/2\pi = 2\hbar|a_{ij}|\bar{n}/m_{\mathrm{Rb}}$, needs to be larger than the rate at which atoms change their velocity class due to lateral collisions, $\gamma_c = 32\sqrt{\pi}/3 \cdot a_{ij}^2 \bar{n}\sqrt{k_{\mathrm{B}}T/m_{\mathrm{Rb}}}$ [110], where $\bar{n}$ is the mean density of the atoms in the trap, a_{ij} is the scattering length and T is the temperature of the ensemble. This condition, the so-called Knudsen regime, can be fulfilled if the atoms

are at very low energies [142]. Secondly, the spin exchange rate must be larger than the frequency inhomogeneity across the cloud, so that atoms can exchange their spins before they acquire a considerable phase difference.

Appendix C. Numerical simulations: Atoms in a superconducting resonator

C.1. Magnetic transport into a flux reservoir

To bring atoms close to the chip surface, the external magnetic field B_{Bias} is turned from the y- to the z-direction by simultaneously changing the currents in two external pairs of coils. In doing so, the distance of the trap to the conductor carrying a current in the x-direction is kept constant and the trap is turned about the conductor axis. In an atom chip with superconducting thin films, the field perpendicular to the chip is strongly modified by the Meissner effect and flux conservation in closed superconducting loops. The quarter-wave resonator on this chip is such a closed loop with extended thin film structures. When changing the magnetic field in the z-direction, B_z, the flux inside the resonator has to stay constant, as it was during cooling the chip through T_{c}. Hence, screening currents are induced in the resonator ground planes, so as to compensate the external flux. Furthermore, currents will flow at the edges of the superconducting structures to keep the interior of the thin films field free.[1]

In order to come to an understanding of what is happening during the transport of the atoms, we perform numerical calculations based on the routine developed in [6]. The simulations include both the Meissner effect as well as the conservation of flux in the cavity gaps. As the program is only capable of calculating two-dimensional fields and current distributions for infinitely long conductors, it cannot simulate currents in a loop. Hence, the flux conservation in the closed resonator loop is included in the simulation by transport currents in the ground planes of the structure. The currents in the two ground planes flow in opposite directions. These currents cause a magnetic flux in the gap which is opposed to the external magnetic field direction. The current was chosen so that the total flux in the resonator gap yielded zero (not the local field, however).

The magnetic field of these screening currents results in a second minimum above the resonator gap, which merges with the trap minimum and leads to a localization

[1] This is a simplification, which is only valid for a superconductor in the Meissner state. Considering a lower critical field of $B_{\mathrm{c1}} \sim \Phi_0/(4\pi\lambda_{\mathrm{L}}^2) \approx 10\,\mathrm{mT}$ for niobium with the London penetration depth $\lambda_{\mathrm{L}} = 120\,\mathrm{nm}$ [143]($B_{\mathrm{c1}} = 0.17\,\mathrm{T}$ for highly pure niobium [144]), the assumption of complete field expulsion from the resonator structure seems reasonable. Numerical simulations suggest that the value B_{c1} is never reached, not even at the edges of the resonator structures.

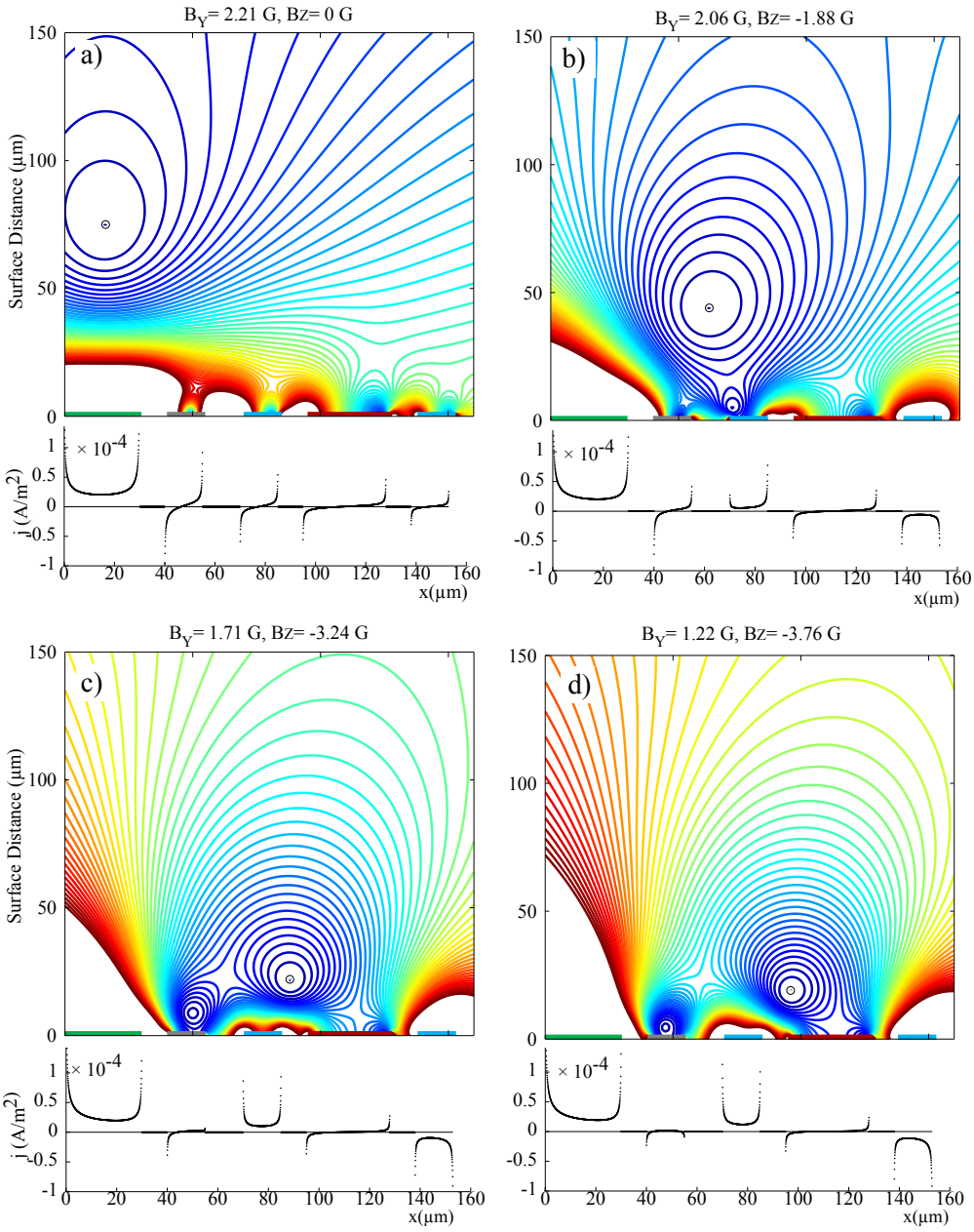

Figure C.1.: Contour plot of simulated potentials (including gravity) for the transfer of atoms into the resonator. Each contour line corresponds to a potential difference of $U/k_B = 2\,\mu\mathrm{K}$. Below each picture, the calculated current densities in the superconducting strips are given. The flux conservation in the resonator structure is modeled by screening currents in the ground planes (blue) of the resonator. When there is no field perpendicular to the chip (a), no net current is flowing in the resonator, but Meissner currents keep the interior of the strips field free. b-d) Field and current distributions for different bias field angles. The current in the trapping wire (green) is 80 mA, the offset field perpendicular to the image plane $B_x = 1\,\mathrm{G}$.

of the atoms within the gap. The atoms are focused into the gap which is close to the trapping conductor (see Fig. C.1). The field minimum of the far ground plane is located on the other side of the niobium film (that is within the sapphire substrate), which is why atoms are not drawn into this gap.

To elucidate the effect of the screening currents, a series of measurements was taken, in which the horizontal position and the distance of the cloud to the surface was determined for different angles of the external field. The location of the cloud was measured *in-situ* by means of reflection imaging of the trapped atoms. The distance to the chip is given to a very good approximation by half of the distance between the two clouds in the image [145]. For a fixed external field B_x, B_y, B_z, the current in the trapping wire was varied and the position of the cloud measured. This series was repeated for different values of B_z (while B_x, B_y =const.). For small angles of the bias field to the surface, the cloud approaches the trapping wire if the current is reduced, as it is expected. For large angles, however, the measurements showed a clear focusing of the trajectories into the resonator gap (Fig. 2.5). The results of the simulations, which were performed without any free parameters, showed very good agreement with the measured data, despite of the simplicity of the model. The simulations are furthermore in excellent agreement with the results obtained using a commercial program which calculates the current distribution in arbitrary planar superconducting geometries [146, 147]. The agreement with the measurements also justifies the assumption that the superconductor is in the Meissner state and that flux penetration of the superconducting strips can be neglected.

C.2. Persistent current trap in a $\lambda/4$-resonator

With aid of the flux conservation in the resonator structure, it is also possible to generate a trap without currents in the trapping wires, based on persistent currents in the resonator. To do so, one has to apply a field $\vec{B_{\mathrm{F}}} = -B_F \cdot \vec{e_z}$ in the $-z$-direction during the cooldown of the superconductor. After cooling through T_c, a field in the positive z-direction is applied. Screening currents in the ground planes will keep the flux in the resonator gaps $\Phi_{\mathrm{F}} \approx B_{\mathrm{F}} A_{\mathrm{Gap}}$ constant. As a result, a potential minimum is formed in the center between the ground planes, below the center conductor. The gravitational potential shifts this minimum away from the surface, resulting in a shallow magnetic trap in which cold atomic clouds can be trapped (see Fig. C.2).

When the resonator structure is cooled in an applied field, it is no longer correct to treat the superconductor as an ideal diamagnet. The critical flux density, below which all fields are expelled from the superconductor, is of the order of $B_{\mathrm{c}} < 100\,\mu\mathrm{T} = 1\,\mathrm{G}$ for a 10 µm wide strip and decreases quadratically with the width of thin film structure [148]. If larger fields are applied during cooling, flux in the form of Abrikosov vortices is frozen inside the superconductor. In order to include this flux $\Phi = A_{\mathrm{SC}} \cdot (B_{\mathrm{F}} - B_{\mathrm{c}})$ into the simulations, we made a simple model that assumes

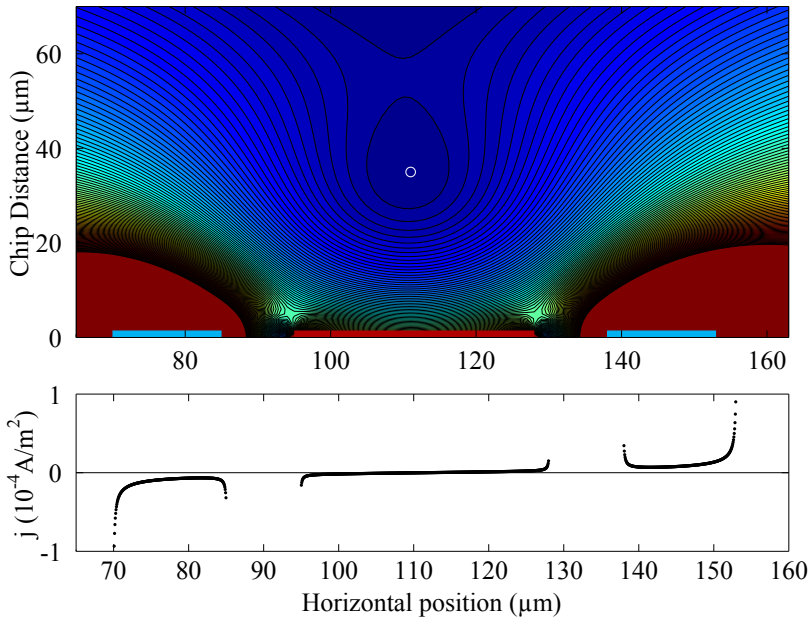

Figure C.2.: Numerical simulation of a persistent trap and the current density in the superconducting structures. In the simulation, a flux density of $B_{\mathrm{F}} = -0.88\,\mathrm{G}$ was used as freezing field in the z-direction. A field of 1.54 G is applied to generate the trap. The offset field was chosen to be 3.2 G, yielding trap oscillation frequencies of $\omega_y = 2\pi \cdot 128\,\mathrm{s}^{-1}$, $\omega_z = 2\pi \cdot 144\,\mathrm{s}^{-1}$. The origin of the axes is chosen as in fig. C.1. The total screening current in the ground planes is 13.4 mA. Each contour line corresponds to a potential difference $U/k_B = 1\,\mu\mathrm{K}$.

a homogeneous penetration of the superconducting thin films by the magnetic field. More specifically, we simulated the Meissner effect including flux conservation in the gaps with a field $B_{\mathrm{bias}} + B_{\mathrm{F}}$. We added a homogeneous magnetic field $-B_{\mathrm{F}}$ to the result of the calculation, which is justifiable, as this approach fulfills the following conditions: 1. A homogeneous field slightly above the superconductors, assuming uniform distribution of vortices, 2. the conservation of the flux in the resonator $\Phi_{\mathrm{F}} = B_{\mathrm{F}} A_{\mathrm{Gap}}$, and 3. a magnetic flux density, which takes the value B_{bias} in a region far away from the superconducting structures. The model has obviously the shortcoming that it does not reproduce the real flux distribution in the superconductor, which is not known exactly.

Given the simplicity of the model, it reproduces the position of the trap with respect to the surface and the measured trap frequencies pretty well. In the case of the persistent current trap described in section 2.4, it was necessary to adjust the input parameters of the simulations by less than 20% in order to match the measured position and oscillation frequencies.

Appendix D. List of physical quantities and acronyms

Acronyms

Abbreviations used in the thesis, in alphabetical order

Acronym	**Signification**
Cu	Copper
EIT	Electromagnetically induced transparency
JJ	Josephson junction
MOT	Magneto-optical trap
MW	Microwave
Nb	Niobium
NMR	Nuclear magnetic resonance
NV	Nitrogen vacancy
QED	Quantum electrodynamics
Rb	Rubidium
RF	Radio frequency
RWA	Rotating wave approximation
SQUID	Superconducting quantum interference device
Ti	Titanium
UHV	Ultra-high vacuum

Physical quantities

The following table lists symbols and physical quantities used in this thesis, listed in alphabetical order.

Symbol	Signification
B_0	Magnetic offset field at the minimum of the magnetic trap
B_{Bias}	Magnetic bias field perpendicular to the current in the trapping wire
B_{F}	Freezing field, magnetic field applied perpendicular to the chip during cooling
B_{m}	Magic offset field $B_{\mathrm{m}} \approx 3.23\,\mathrm{G}$
d	Atom-surface separation
Δ	Detuning of the radio-frequency and microwave to the intermediate level of the two-photon transition
δ	Detuning of the sum frequency of microwave and radio-frequency from the atomic transition $\delta = \omega_{\mathrm{MW}} + \omega_{\mathrm{RF}} - \omega_0$
Γ	Rubidium D-line width, $\Gamma \approx 2\pi \cdot 6\,\mathrm{MHz}$
$\hbar$	Reduced Planck constant $\hbar = 1.05457148 \times 10^{-34}\,\mathrm{m^2kg/s}$
I_{Nb}	Current in the niobium wire
I_{Scr}	Screening current in the resonator ground planes, which keeps the flux in the resonator gaps constant
I_{Trap}	Current in the trapping wire on the atom chip
k_{B}	Boltzmann constant, $k_{\mathrm{B}} = 1.3806488(13) \times 10^{-23}\,\mathrm{J/K}$
λ	Wavelength
N	Number of atoms
$\nu_{\mathrm{MW}}, \nu_{\mathrm{RF}}$	Microwave frequency, radio frequency
P	Power
Q	Quality factor of a resonator, defined as ratio between resonance frequency and resonance width $Q = \omega/\Delta\omega$
T	Temperature
T_{c}	Critical temperature, below which the material becomes superconducting
T_2	Coherence time of superposition states
T_{R}	Ramsey interrogation time, i.e. time between two $\pi/2$-pulses in Ramsey interferometry
τ	Spin flip lifetime
Φ_0	Magnetic flux quantum $\Phi_0 = 2.068 \times 10^{-15}\,\mathrm{Wb}$
Φ_{F}	Flux in the resonator gaps
ω_r, ω_l	Radial and longitudinal trap oscillation frequencies
ω_{L}	Larmor frequency
Ω	Rabi frequency (used with different indices, depending on the context)

Bibliography

[1] D. Cano, H. Hattermann, B. Kasch, C. Zimmermann, R. Kleiner, D. Koelle, and J. Fortágh, "Experimental system for research on ultracold atomic gases near superconducting microstructures," Eur. Phys. J. D **63**, 17 (2011).

[2] D. Cano, B. Kasch, H. Hattermann, R. Kleiner, C. Zimmermann, D. Koelle, and J. Fortágh, "Meissner Effect in Superconducting Microtraps," Phys. Rev. Lett. **101**, 183006 (2008).

[3] B. Kasch, H. Hattermann, D. Cano, T. E. Judd, S. Scheel, C. Zimmermann, R. Kleiner, D. Koelle, and J. Fortágh, "Cold atoms near superconductors: atomic spin coherence beyond the Johnson noise limit," New J. Phys. **12**, 065024 (2010).

[4] S. Bernon, H. Hattermann, D. Bothner, M. Knufinke, P. Weiss, F. Jessen, D. Cano, M. Kemmler, R. Kleiner, D. Koelle, and J. Fortágh, "Manipulation and coherence of ultra-cold atoms on a superconducting atom chip," Nat. Commun. **4**, 2380 (2013).

[5] H. Hattermann, M. Mack, F. Karlewski, F. Jessen, D. Cano, and J. Fortágh, "Detrimental adsorbate fields in experiments with cold Rydberg gases near surfaces," Phys. Rev. A **86**, 022511 (2012).

[6] D. Cano, B. Kasch, H. Hattermann, D. Koelle, R. Kleiner, C. Zimmermann, and J. Fortágh, "Impact of the Meissner effect on magnetic microtraps for neutral atoms near superconducting thin films," Phys. Rev. A **77**, 063408 (2008).

[7] M. Mack, F. Karlewski, H. Hattermann, S. Höckh, F. Jessen, D. Cano, and J. Fortágh, "Measurement of absolute transition frequencies of ^{87}Rb to nS and nD Rydberg states by means of electromagnetically induced transparency," Phys. Rev. A **83**, 052515 (2011).

[8] C. L. Hernández-Cedillo, S. Bernon, H. Hattermann, J. Fortágh, and R. Jáuregui, "Scattering of dilute thermal atom clouds on optical Weber beams," Phys. Rev. A **87**, 023404 (2013).

[9] R. Feynman, "Simulating physics with computers," International Journal of Theoretical Physics **21**, 467 (1982).

[10] D. R. Simon, "On the Power of Quantum Computation," SIAM Journal on Computing **26**, 116 (1994).

[11] D. Deutsch and R. Jozsa, "Rapid Solution of Problems by Quantum Computation," Proceedings of the Royal Society of London. Series A: Mathematical and Physical Sciences **439**, 553 (1992).

[12] P. Shor, "Polynomial-Time Algorithms for Prime Factorization and Discrete Logarithms on a Quantum Computer," SIAM Journal on Computing **26**, 1484 (1997).

[13] L. K. Grover, "A fast quantum mechanical algorithm for database search," in *Proceedings of the twenty-eighth annual ACM symposium on Theory of computing*, STOC '96 (ACM, New York, NY, USA, 1996) pp. 212–219.

[14] H. Häffner, C. F. Roos, and R. Blatt, "Quantum computing with trapped ions," Phys. Rep. **469**, 155 (2008).

[15] R. Blatt and D. Wineland, "Entangled states of trapped atomic ions," Nature **453**, 1008 (2008).

[16] J. I. Cirac and P. Zoller, "Quantum Computations with Cold Trapped Ions," Phys. Rev. Lett. **74**, 4091 (1995).

[17] C. Monroe, D. M. Meekhof, B. E. King, W. M. Itano, and D. J. Wineland, "Demonstration of a Fundamental Quantum Logic Gate," Phys. Rev. Lett. **75**, 4714 (1995).

[18] T. Monz, K. Kim, W. Hänsel, M. Riebe, A. S. Villar, P. Schindler, M. Chwalla, M. Hennrich, and R. Blatt, "Realization of the Quantum Toffoli Gate with Trapped Ions," Phys. Rev. Lett. **102**, 040501 (2009).

[19] J. Chiaverini, J. Britton, D. Leibfried, E. Knill, M. D. Barrett, R. B. Blakestad, W. M. Itano, J. D. Jost, C. Langer, R. Ozeri, T. Schaetz, and D. J. Wineland, "Implementation of the Semiclassical Quantum Fourier Transform in a Scalable System," Science **308**, 997 (2005).

[20] T. Monz, P. Schindler, J. T. Barreiro, M. Chwalla, D. Nigg, W. A. Coish, M. Harlander, W. Hänsel, M. Hennrich, and R. Blatt, "14-Qubit Entanglement: Creation and Coherence," Phys. Rev. Lett. **106**, 130506 (2011).

[21] J. A. Jones and M. Mosca, "Implementation of a quantum algorithm on a nuclear magnetic resonance quantum computer," J. Chem. Phys. **109**, 1648 (1998).

[22] L. M. K. Vandersypen, M. Steffen, G. Breyta, C. S. Yannoni, M. H. Sherwood, and I. L. Chuang, "Experimental realization of Shor's quantum factoring algorithm using nuclear magnetic resonance," Nature **414**, 883 (2001).

[23] W. S. Warren, "The Usefulness of NMR Quantum Computing," Science **277**, 1688 (1997).

[24] J. L. O'Brien, "Optical Quantum Computing," Science **318**, 1567 (2007).

[25] A. Politi, M. J. Cryan, J. G. Rarity, S. Yu, and J. L. O'Brien, "Silica-on-Silicon Waveguide Quantum Circuits," Science **320**, 646 (2008).

[26] J. L. O'Brien, G. J. Pryde, A. G. White, and T. C. Ralph, "High-fidelity Z-measurement error encoding of optical qubits," Phys. Rev. A **71**, 060303 (2005).

[27] A. Politi, J. C. F. Matthews, and J. L. O'Brien, "Shor's Quantum Factoring Algorithm on a Photonic Chip," Science **325**, 1221 (2009).

[28] D. Loss and D. P. DiVincenzo, "Quantum computation with quantum dots," Phys. Rev. A **57**, 120 (1998).

[29] A. Imamoğlu, D. D. Awschalom, G. Burkard, D. P. DiVincenzo, D. Loss, M. Sherwin, and A. Small, "Quantum Information Processing Using Quantum Dot Spins and Cavity QED," Phys. Rev. Lett. **83**, 4204 (1999).

[30] X. Li, Y. Wu, D. Steel, D. Gammon, T. H. Stievater, D. S. Katzer, D. Park, C. Piermarocchi, and L. J. Sham, "An All-Optical Quantum Gate in a Semiconductor Quantum Dot," Science **301**, 809 (2003).

[31] A. Wallraff, D. Schuster, A. Blais, L. Frunzio, R. Huang, J. Majer, S. Kumar, S. Girvin, and R. Schoelkopf, "Strong coupling of a single photon to a superconducting qubit using circuit quantum electrodynamics," Nature **431**, 162 (2004).

[32] M. A. Sillanpää, J. I. Park, and R. W. Simmonds, "Coherent quantum state storage and transfer between two phase qubits via a resonant cavity," Nature **449**, 438 (2007).

[33] J. Majer, J. M. Chow, J. M. Gambetta, J. Koch, B. R. Johnson, J. A. Schreier, L. Frunzio, D. I. Schuster, A. A. Houck, A. Wallraff, A. Blais, M. H. Devoret, S. M. Girvin, and R. J. Schoelkopf, "Coupling superconducting qubits via a cavity bus," Nature **449**, 443 (2007).

[34] L. DiCarlo, M. D. Reed, L. Sun, B. R. Johnson, J. M. Chow, J. M. Gambetta, L. Frunzio, S. M. Girvin, M. H. Devoret, and R. J. Schoelkopf, "Preparation and measurement of three-qubit entanglement in a superconducting circuit," Nature **467**, 574 (2010).

[35] L. DiCarlo, J. M. Chow, J. M. Gambetta, L. S. Bishop, B. R. Johnson, D. I. Schuster, J. Majer, A. Blais, L. Frunzio, S. M. Girvin, and R. J. Schoelkopf, "Demonstration of two-qubit algorithms with a superconducting quantum processor," Nature **460**, 240 (2009).

[36] A. Fedorov, L. Steffen, M. Baur, M. P. da Silva, and A. Wallraff, "Implementation of a Toffoli gate with superconducting circuits," Nature **481**, 170 (2012).

[37] M. D. Reed, L. Dicarlo, S. E. Nigg, L. Sun, L. Frunzio, S. M. Girvin, and R. J. Schoelkopf, "Realization of three-qubit quantum error correction with superconducting circuits," Nature **482**, 382 (2012).

[38] E. Lucero, R. Barends, Y. Chen, J. Kelly, M. Mariantoni, A. Megrant, P. O'Malley, D. Sank, A. Vainsencher, J. Wenner, T. White, Y. Yin, A. N. Cleland, and J. M. Martinis, "Computing prime factors with a Josephson phase qubit quantum processor," Nat. Phys. **8**, 719 (2012).

[39] M. Saffman, T. G. Walker, and K. Mølmer, "Quantum information with Rydberg atoms," Rev. Mod. Phys. **82**, 2313 (2010).

[40] E. Urban, T. A. Johnson, T. Henage, L. Isenhower, D. D. Yavuz, T. G. Walker, and M. Saffman, "Observation of Rydberg blockade between two atoms," Nat. Phys. **5**, 110 (2009).

[41] A. Gaëtan, Y. Miroshnychenko, T. Wilk, A. Chotia, M. Viteau, D. Comparat, P. Pillet, A. Browaeys, and P. Grangier, "Observation of collective excitation of two individual atoms in the Rydberg blockade regime," Nat. Phys. **5**, 115 (2009).

[42] D. Jaksch, J. I. Cirac, P. Zoller, S. L. Rolston, R. Côté, and M. D. Lukin, "Fast Quantum Gates for Neutral Atoms," Phys. Rev. Lett. **85**, 2208 (2000).

[43] M. D. Lukin, M. Fleischhauer, R. Cote, L. M. Duan, D. Jaksch, J. I. Cirac, and P. Zoller, "Dipole Blockade and Quantum Information Processing in Mesoscopic Atomic Ensembles," Phys. Rev. Lett. **87**, 037901 (2001).

[44] T. Wilk, A. Gaëtan, C. Evellin, J. Wolters, Y. Miroshnychenko, P. Grangier, and A. Browaeys, "Entanglement of Two Individual Neutral Atoms Using Rydberg Blockade," Phys. Rev. Lett. **104**, 010502 (2010).

[45] L. Isenhower, E. Urban, X. L. Zhang, A. T. Gill, T. Henage, T. A. Johnson, T. G. Walker, and M. Saffman, "Demonstration of a Neutral Atom Controlled-NOT Quantum Gate," Phys. Rev. Lett. **104**, 010503 (2010).

[46] D. P. DiVincenzo, "The Physical Implementation of Quantum Computation," Fortschritte der Physik **48**, 771 (2000).

[47] Z. Kim, B. Suri, V. Zaretskey, S. Novikov, K. D. Osborn, A. Mizel, F. C. Wellstood, and B. S. Palmer, "Decoupling a Cooper-Pair Box to Enhance the Lifetime to 0.2 ms," Phys. Rev. Lett. **106**, 120501 (2011).

[48] H. Paik, D. I. Schuster, L. S. Bishop, G. Kirchmair, G. Catelani, A. P. Sears, B. R. Johnson, M. J. Reagor, L. Frunzio, L. I. Glazman, S. M. Girvin, M. H. Devoret, and R. J. Schoelkopf, "Observation of High Coherence in Josephson Junction Qubits Measured in a Three-Dimensional Circuit QED Architecture," Phys. Rev. Lett. **107**, 240501 (2011).

[49] S. Camerer, M. Korppi, A. Jöckel, D. Hunger, T. W. Hänsch, and P. Treutlein, "Realization of an Optomechanical Interface Between Ultracold Atoms and a Membrane," Phys. Rev. Lett. **107**, 223001 (2011).

[50] A. D. O'Connell, M. Hofheinz, M. Ansmann, R. C. Bialczak, M. Lenander, E. Lucero, M. Neeley, D. Sank, H. Wang, M. Weides, J. Wenner, J. M. Martinis, and A. N. Cleland, "Quantum ground state and single-phonon control of a mechanical resonator," Nature **464**, 697 (2010).

[51] C. Simon, M. Afzelius, J. Appel, A. Boyer de la Giroday, S. J. Dewhurst, N. Gisin, C. Y. Hu, F. Jelezko, S. Kröll, J. H. Müller, J. Nunn, E. S. Polzik, J. G. Rarity, H. De Riedmatten, W. Rosenfeld, A. J. Shields, N. Sköld, R. M. Stevenson, R. Thew, I. A. Walmsley, M. C. Weber, H. Weinfurter, J. Wrachtrup, and R. J. Young, "Quantum memories," Eur. Phys. J. D **58**, 1 (2010).

[52] H.-J. Briegel, W. Dür, J. I. Cirac, and P. Zoller, "Quantum Repeaters: The Role of Imperfect Local Operations in Quantum Communication," Phys. Rev. Lett. **81**, 5932 (1998).

[53] H. J. Kimble, "The quantum internet," Nature **453**, 1023 (2008).

[54] D. I. Schuster, A. P. Sears, E. Ginossar, L. DiCarlo, L. Frunzio, J. J. L. Morton, H. Wu, G. A. D. Briggs, B. B. Buckley, D. D. Awschalom, and R. J. Schoelkopf, "High-Cooperativity Coupling of Electron-Spin Ensembles to Superconducting Cavities," Phys. Rev. Lett. **105**, 140501 (2010).

[55] Y. Kubo, F. R. Ong, P. Bertet, D. Vion, V. Jacques, D. Zheng, A. Dréau, J.-F. Roch, A. Auffeves, F. Jelezko, J. Wrachtrup, M. F. Barthe, P. Bergonzo, and D. Esteve, "Strong Coupling of a Spin Ensemble to a Superconducting Resonator," Phys. Rev. Lett. **105**, 140502 (2010).

[56] R. Amsüss, C. Koller, T. Nöbauer, S. Putz, S. Rotter, K. Sandner, S. Schneider, M. Schramböck, G. Steinhauser, H. Ritsch, J. Schmiedmayer, and J. Majer, "Cavity QED with Magnetically Coupled Collective Spin States," Phys. Rev. Lett. **107**, 060502 (2011).

[57] P. C. Maurer, G. Kucsko, C. Latta, L. Jiang, N. Y. Yao, S. D. Bennett, F. Pastawski, D. Hunger, N. Chisholm, M. Markham, D. J. Twitchen, J. I. Cirac, and M. D. Lukin, "Room-Temperature Quantum Bit Memory Exceeding One Second," Science **336**, 1283 (2012).

[58] P. Bushev, A. K. Feofanov, H. Rotzinger, I. Protopopov, J. H. Cole, C. M. Wilson, G. Fischer, A. Lukashenko, and A. V. Ustinov, "Ultralow-power spectroscopy of a rare-earth spin ensemble using a superconducting resonator," Phys. Rev. B **84**, 060501 (2011).

[59] A. G. Radnaev, Y. O. Dudin, R. Zhao, H. H. Jen, S. D. Jenkins, A. Kuzmich, and T. A. B. Kennedy, "A quantum memory with telecom-wavelength conversion," Nat. Phys. **6**, 894 (2010).

[60] Y. O. Dudin, R. Zhao, T. A. B. Kennedy, and A. Kuzmich, "Light storage in a magnetically dressed optical lattice," Phys. Rev. A **81**, 041805 (2010).

[61] H. P. Specht, C. Nölleke, A. Reiserer, M. Uphoff, E. Figueroa, S. Ritter, and G. Rempe, "A single-atom quantum memory," Nature **473**, 190 (2011).

[62] M. Lettner, M. Mücke, S. Riedl, C. Vo, C. Hahn, S. Baur, J. Bochmann, S. Ritter, S. Dürr, and G. Rempe, "Remote Entanglement between a Single Atom and a Bose-Einstein Condensate," Phys. Rev. Lett. **106**, 210503 (2011).

[63] S. Ritter, C. Nölleke, C. Hahn, A. Reiserer, A. Neuzner, M. Uphoff, M. Mücke, E. Figueroa, J. Bochmann, and G. Rempe, "An elementary quantum network of single atoms in optical cavities," Nature **484**, 195 (2012).

[64] A. André, D. Demille, J. M. Doyle, M. D. Lukin, S. E. Maxwell, P. Rabl, R. J. Schoelkopf, and P. Zoller, "A coherent all-electrical interface between polar molecules and mesoscopic superconducting resonators," Nat. Phys. **2**, 636 (2006).

[65] P. Rabl, D. DeMille, J. M. Doyle, M. D. Lukin, R. J. Schoelkopf, and P. Zoller, "Hybrid Quantum Processors: Molecular Ensembles as Quantum Memory for Solid State Circuits," Phys. Rev. Lett. **97**, 033003 (2006).

[66] D. Petrosyan, G. Bensky, G. Kurizki, I. Mazets, J. Majer, and J. Schmiedmayer, "Reversible state transfer between superconducting qubits and atomic ensembles," Phys. Rev. A **79**, 040304 (2009).

[67] D. Petrosyan and M. Fleischhauer, "Quantum Information Processing with Single Photons and Atomic Ensembles in Microwave Coplanar Waveguide Resonators," Phys. Rev. Lett. **100**, 170501 (2008).

[68] J. Verdú, H. Zoubi, C. Koller, J. Majer, H. Ritsch, and J. Schmiedmayer, "Strong Magnetic Coupling of an Ultracold Gas to a Superconducting Waveguide Cavity," Phys. Rev. Lett. **103**, 043603 (2009).

[69] K. Henschel, J. Majer, J. Schmiedmayer, and H. Ritsch, "Cavity QED with an ultracold ensemble on a chip: Prospects for strong magnetic coupling at finite temperatures," Phys. Rev. A **82**, 033810 (2010).

[70] M. Hafezi, Z. Kim, S. L. Rolston, L. A. Orozco, B. L. Lev, and J. M. Taylor, "Atomic interface between microwave and optical photons," Phys. Rev. A **85**, 020302 (2012).

[71] A. Zagoskin and A. Blais, "Superconducting qubits," ArXiv e-prints , 0805.0164 (2008).

[72] E. L. Raab, M. Prentiss, A. Cable, S. Chu, and D. E. Prichard, "Trapping of Neutral Sodium Atoms with Radiation Pressure," Phys. Rev. Lett. **59**, 2631 (1987).

[73] M. H. Anderson, J. R. Ensher, M. R. Matthews, C. E. Wieman, and E. A. Cornell, "Observation of Bose-Einstein Condensation in a Dilute Atomic Vapor," Science **269**, 198 (1995).

[74] K. B. Davis, M.-O. Mewes, M. R. Andrews, N. J. van Druten, D. S. Durfee, D. Kurn, and W. Ketterle, "Bose-Einstein Condensation in an Gas of Sodium Atoms," Phys. Rev. Lett. **75**, 3969 (1995).

[75] R. Grimm, M. Weidemüller, and Y. B. Ovchinnikov, "Optical Dipole Traps for Neutral Atoms," Adv. At. Mol. Opt. Phys. **42**, 95 (2000).

[76] J. Fortágh and C. Zimmermann, "Magnetic microtraps for ultracold atoms," Rev. Mod. Phys. **79**, 235 (2007).

[77] J. Fortágh, H. Ott, S. Kraft, A. Günther, and C. Zimmermann, "Surface effects in magnetic microtraps," Phys. Rev. A **66**, 041604 (2002).

[78] J. M. Obrecht, R. J. Wild, and E. A. Cornell, "Measuring electric fields from surface contaminants with neutral atoms," Phys. Rev. A **75**, 062903 (2007).

[79] D. M. Harber, J. M. Obrecht, J. M. McGuirk, and E. A. Cornell, "Measurement of the Casimir-Polder force through center-of-mass oscillations of a Bose-Einstein condensate," Phys. Rev. A **72**, 033610 (2005).

[80] J. M. Obrecht, R. J. Wild, M. Antezza, L. P. Pitaevskii, S. Stringari, and E. A. Cornell, "Measurement of the Temperature Dependence of the Casimir-Polder Force," Phys. Rev. Lett. **98**, 063201 (2007).

[81] M. Gierling, P. Schneeweiss, G. Visanescu, P. Federsel, M. Häffner, D. P. Kern, T. E. Judd, A. Günther, and J. Fortágh, "Cold-atom scanning probe microscopy," Nature Nanotechnology **6**, 446 (2011).

[82] M. P. A. Jones, C. J. Vale, D. Sahagun, B. V. Hall, and E. A. Hinds, "Spin Coupling between Cold Atoms and the Thermal Fluctuations of a Metal Surface," Phys. Rev. Lett. **91**, 080401 (2003).

[83] D. M. Harber, J. M. McGuirk, J. M. Obrecht, and E. A. Cornell, "Thermally Induced Losses in Ultra-Cold Atoms Magnetically Trapped Near Room-Temperature Surfaces," J. Low Temp. Phys. **133**, 229 (2003).

[84] Y.-j. Lin, I. Teper, C. Chin, and V. Vuletić, "Impact of the Casimir-Polder Potential and Johnson Noise on Bose-Einstein Condensate Stability Near Surfaces," Phys. Rev. Lett. **92**, 050404 (2004).

[85] S. Scheel, P. K. Rekdal, P. L. Knight, and E. A. Hinds, "Atomic spin decoherence near conducting and superconducting films," Phys. Rev. A **72**, 042901 (2005).

[86] T. Nirrengarten, A. Qarry, C. Roux, A. Emmert, G. Nogues, M. Brune, J.-M. Raimond, and S. Haroche, "Realization of a Superconducting Atom Chip," Phys. Rev. Lett **97**, 200405 (2006).

[87] T. Mukai, C. Hufnagel, A. Kasper, T. Meno, A. Tsukada, K. Semba, and F. Shimizu, "Persistent Supercurrent Atom Chip," Phys. Rev. Lett **98**, 260407 (2007).

[88] C. Roux, A. Emmert, A. Lupascu, T. Nirrengarten, G. Nogues, M. Brune, J. M. Raimond, and S. Haroche, "Bose-Einstein condensation on a superconducting atom chip," Europhys. Lett. **81**, 56004 (2008).

[89] A. Emmert, A. Lupaşcu, M. Brune, J.-M. Raimond, S. Haroche, and G. Nogues, "Microtraps for neutral atoms using superconducting structures in the critical state," Phys. Rev. A **80**, 061604 (2009).

[90] C. Hufnagel, T. Mukai, and F. Shimizu, "Stability of a superconductive atom chip with persistent current," Phys. Rev. A **79**, 053641 (2009).

[91] F. Shimizu, C. Hufnagel, and T. Mukai, "Stable Neutral Atom Trap with a Thin Superconducting Disc," Phys. Rev. Lett. **103**, 253002 (2009).

[92] T. Müller, B. Zhang, R. Fermani, K. S. Chan, Z. W. Wang, C. B. Zhang, M. J. Lim, and R. Dumke, "Trapping of ultra-cold atoms with the magnetic field of vortices in a thin-film superconducting micro-structure," New J. Phys. **12**, 043016 (2010).

[93] T. Müller, B. Zhang, R. Fermani, K. S. Chan, M. J. Lim, and R. Dumke, "Programmable trap geometries with superconducting atom chips," Phys. Rev. A **81**, 053624 (2010).

[94] B. Zhang, R. Fermani, T. Müller, M. J. Lim, and R. Dumke, "Design of magnetic traps for neutral atoms with vortices in type-II superconducting microstructures," Phys. Rev. A **81**, 063408 (2010).

[95] B. Zhang, M. Siercke, K. S. Chan, M. Beian, M. J. Lim, and R. Dumke, "Magnetic confinement of neutral atoms based on patterned vortex distributions in superconducting disks and rings," Phys. Rev. A **85**, 013404 (2012).

[96] M. Siercke, K. S. Chan, B. Zhang, M. Beian, M. J. Lim, and R. Dumke, "Reconfigurable self-sufficient traps for ultracold atoms based on a superconducting square," Phys. Rev. A **85**, 041403 (2012).

[97] S. Scheel, R. Fermani, and E. A. Hinds, "Feasibility of studying vortex noise in two-dimensional superconductors with cold atoms," Phys. Rev. A **75**, 064901 (2007).

[98] G. Nogues, C. Roux, T. Nirrengarten, A. Lupaşcu, A. Emmert, M. Brune, J.-M. Raimond, S. Haroche, B. Plaçais, and J.-J. Greffet, "Effect of vortices on the spin-flip lifetime of atoms in superconducting atom-chips," Eur. Phys. Lett. **87**, 13002 (2009).

[99] A. Emmert, A. Lupaşcu, G. Nogues, M. Brune, J.-M. Raimond, and S. Haroche, "Measurement of the trapping lifetime close to a cold metallic surface on a cryogenic atom-chip," Eur. Phys. J. D **51**, 173 (2009).

[100] T. L. Gustavson, A. P. Chikkatur, A. E. Leanhardt, A. Görlitz, S. Gupta, D. E. Pritchard, and W. Ketterle, "Transport of Bose-Einstein Condensates with Optical Tweezers," Phys. Rev. Lett. **88**, 020401 (2001).

[101] C. V. Sukumar and D. M. Brink, "Spin-flip transitions in a magnetic trap," Phys. Rev. A **56**, 2451 (1997).

[102] W. Meissner and R. Ochsenfeld, "Ein neuer Effekt bei Eintritt der Supraleitfähigkeit," Naturwissenschaften **21**, 787 (1933).

[103] D. Cano, *Meissner effect in superconducting microtraps*, Ph.D. thesis, Universität Tübingen (2008).

[104] J. B. Johnson, "Thermal Agitation of Electricity in Conductors," Phys. Rev. **32**, 97 (1928).

[105] C. Henkel, S. Pötting, and M. Wilkens, "Loss and heating of particles in small and noisy traps," Appl. Phys. B **69**, 379 (1999).

[106] B. K. Skagerstam, U.Hohenester, A. Eiguren, and P. K. Rekdal, "Spin Decoherence in Superconducting Atom Chips," Phys. Rev. Lett **97**, 070401 (2006).

[107] U. Hohenester, A. Eiguren, S. Scheel, and E. A. Hinds, "Spin-flip lifetimes in superconducting atom chips: Bardeen-Cooper-Schrieffer versus Eliashberg theory," Phys. Rev. A **76**, 033618 (2007).

[108] D. M. Harber, H. J. Lewandowski, J. M. McGuirk, and E. A. Cornell, "Effect of cold collisions on spin coherence and resonance shifts in a magnetically trapped ultracold gas," Phys. Rev. A **66**, 053616 (2002).

[109] P. Treutlein, P. Hommelhoff, T. Steinmetz, T. W. Hänsch, and J. Reichel, "Coherence in Microchip Traps," Phys. Rev. Lett. **92**, 203005 (2004).

[110] C. Deutsch, F. Ramirez-Martinez, C. Lacroûte, F. Reinhard, T. Schneider, J. N. Fuchs, F. Piéchon, F. Laloë, J. Reichel, and P. Rosenbusch, "Spin Self-Rephasing and Very Long Coherence Times in a Trapped Atomic Ensemble," Phys. Rev. Lett. **105**, 020401 (2010).

[111] G. Kleine Büning, J. Will, W. Ertmer, E. Rasel, J. Arlt, C. Klempt, F. Ramirez-Martinez, F. Piéchon, and P. Rosenbusch, "Extended Coherence Time on the Clock Transition of Optically Trapped Rubidium," Phys. Rev. Lett. **106**, 240801 (2011).

[112] J. Hoffman, J. Grover, Z. Kim, A. Wood, J. Anderson, A. Dragt, M. Hafezi, C. Lobb, L. Orozco, S. Rolston, J. Taylor, C. Vlahacos, and F. Wellstood, "Atoms talking to SQUIDs," Rev. Mex. Fis. S **57(3)**, 1 (2011).

[113] J. M. McGuirk, D. M. Harber, J. M. Obrecht, and E. A. Cornell, "Alkali-metal adsorbate polarization on conducting and insulating surfaces probed with Bose-Einstein condensates," Phys. Rev. A **69**, 062905 (2004).

[114] A. Tauschinsky, R. M. T. Thijssen, S. Whitlock, H. B. van Linden van den Heuvell, and R. J. C. Spreeuw, "Spatially resolved excitation of Rydberg atoms and surface effects on an atom chip," Phys. Rev. A **81**, 063411 (2010).

[115] M. Fleischhauer, A. Imamoglu, and J. P. Marangos, "Electromagnetically induced transparency: Optics in coherent media," Rev. Mod. Phys. **77**, 633 (2005).

[116] B. Zhao, Y.-A. Chen, X.-H. Bao, T. Strassel, C.-S. Chuu, X.-M. Jin, J. Schmiedmayer, Z.-S. Yuan, S. Chen, and J.-W. Pan, "A millisecond quantum memory for scalable quantum networks," Nat. Phys. **5**, 95 (2009).

[117] R. Zhao, Y. O. Dudin, S. D. Jenkins, C. J. Campbell, D. N. Matsukevich, T. A. B. Kennedy, and A. Kuzmich, "Long-lived quantum memory," Nat. Phys. **5**, 100 (2009).

[118] M. Singh, "Macroscopic entanglement between a Bose Einstein condensate and a superconducting loop," Opt. Express **17**, 2600 (2009).

[119] K. Dieckmann, R. J. C. Spreeuw, M. Weidemüller, and J. T. M. Walraven, "Two-dimensional magneto-optical trap as a source of slow atoms," Phys. Rev. A **58**, 3891 (1998).

[120] J. Fortágh, A. Grossmann, T. W. Hänsch, and C. Zimmermann, "Fast loading of a magneto-optical trap from a pulsed thermal source," J. Appl. Phys. **84**, 6499 (1998).

[121] C. Back, *UHV-Cluster-Anlage zur Herstellung von Dünnfilmstrukturen und Transport- und Rauscheigenschaften von $YBa_2Cu_3O_7$-d-Korngrenzen-SQUIDs*, Ph.D. thesis, Universität Tübingen, Wilhelmstr. 32, 72074 Tübingen (2007).

[122] Cerasolzer, MBR ELECTRONICS GmbH, Jonastrasse 8, CH-8636 Wald - Switzerland.

[123] K. R. Patton and U. R. Fischer, "Hybrid of superconducting quantum interference device and atomic Bose-Einstein condensate: An architecture for quantum information processing," Phys. Rev. A **87**, 052303 (2013).

[124] A. Günther, S. Kraft, M. Kemmler, D. Koelle, R. Kleiner, C. Zimmermann, and J. Fortágh, "Diffraction of a Bose-Einstein Condensate from a Magnetic Lattice on a Microchip," Phys. Rev. Lett. **95**, 170405 (2005).

[125] B. Kasch, *Atomic spin coherence in superconductiong microtraps*, Ph.D. thesis, Universität Tübingen (2010).

[126] G. C. Bjorklund, "Frequency-modulation spectroscopy: a new method for measuring weak absorptions and dispersions," Opt. Lett. **5**, 15 (1980).

[127] G. Bjorklund, M. Levenson, W. Lenth, and C. Ortiz, "Frequency modulation (FM) spectroscopy," Applied Physics B **32**, 145 (1983).

[128] D. Steck, "Rubidium 87 D line data," (2010).

[129] T. R. Gentile, B. J. Hughey, D. Kleppner, and T. W. Ducas, "Experimental study of one- and two-photon Rabi oscillations," Phys. Rev. A **40**, 5103 (1989).

[130] C. Zimmermann, "Atome, Moleküle und Licht," Lecture Notes, Universtät Tübingen (2012).

[131] R. P. Anderson, *Nonequilibrium dynamics and relative phase evolution of two-component Bose-Einstein condensates*, Ph.D. thesis, Swinburne University (2010).

[132] R. P. Feynman, J. Frank L. Vernon, and R. W. Hellwarth, "Geometrical Representation of the Schrödinger Equation for Solving Maser Problems," Journal of Applied Physics **28**, 49 (1957).

[133] S. Haroche and J. Raimond, *Exploring the Quantum: Atoms, Cavities, and Photons*, Oxford graduate texts in mathematics (OUP Oxford, 2006).

[134] M. Fox, *Quantum Optics : An Introduction: An Introduction*, Oxford Master Series in Physics (OUP Oxford, 2006).

[135] N. Ramsey, "A New Molecular Beam Method," Phys. Rev. **76**, 996 (1949).

[136] P. Rosenbusch, "Magnetically trapped atoms for compact atomic clocks," Applied Physics B **95**, 227 (2009).

[137] K. M. Mertes, J. W. Merrill, R. Carretero-González, D. J. Frantzeskakis, P. G. Kevrekidis, and D. S. Hall, "Nonequilibrium Dynamics and Superfluid Ring Excitations in Binary Bose-Einstein Condensates," Phys. Rev. Lett. **99**, 190402 (2007).

[138] M. Egorov, B. Opanchuk, P. Drummond, B. V. Hall, P. Hannaford, and A. I. Sidorov, "Precision measurements of s-wave scattering lengths in a two-component Bose-Einstein condensate," ArXiv:1204.1591 (2012).

[139] Lhuillier, C. and Laloë, F., "Transport properties in a spin polarized gas, I," J. Phys. France **43**, 197 (1982).

[140] Lhuillier, C. and Laloë, F., "Transport properties in a spin polarized gas, II," J. Phys. France **43**, 225 (1982).

[141] J. N. Fuchs, D. M. Gangardt, and F. Laloë, "Internal State Conversion in Ultracold Gases," Phys. Rev. Lett. **88**, 230404 (2002).

[142] K. Gibble, "Keeping atoms synchronized for better timekeeping," Physics **3**, 55 (2010).

[143] W. Buckel and R. Kleiner, *Superconductivity: fundamentals and applications* (Wiley-VCH, 2004).

[144] D. K. Finnemore, T. F. Stromberg, and C. A. Swenson, "Superconducting Properties of High-Purity Niobium," Phys. Rev. **149**, 231 (1966).

[145] D. A. Smith, S. Aigner, S. Hofferberth, M. Gring, M. Andersson, S. Wildermuth, P. Krüger, S. Schneider, T. Schumm, and J. Schmiedmayer, "Absorption imaging of ultracold atoms on atom chips," Opt. Express **19**, 8471 (2011).

[146] M. M. Khapaev, M. Y. Kupriyanov, E. Goldobin, and M. Siegel, "Current distribution simulation for superconducting multi-layered structures," Superconductor Science and Technology **16**, 24 (2003).

[147] M. Knufinke, *Aufbau und Entwicklung von Experimenten an Supraleiter-Atom-Hybridsystemen*, Ph.D. thesis, Universität Tübingen, Wilhelmstr. 32, 72074 Tübingen (2013).

[148] G. Stan, S. B. Field, and J. M. Martinis, "Critical Field for Complete Vortex Expulsion from Narrow Superconducting Strips," Phys. Rev. Lett. **92**, 097003 (2004).

Appended publications

Publication 1

D. Cano, H. Hattermann, B. Kasch, C. Zimmermann, R. Kleiner, D. Koelle, and J. Fortágh,
Experimental system for research on ultracold atomic gases near superconducting microstrucures,
Eur. Phys. J. D **63**, 17-23 (2011).

Eur. Phys. J. D **63**, 17–23 (2011)
DOI: 10.1140/epjd/e2011-10680-8

THE EUROPEAN PHYSICAL JOURNAL D

Regular Article

Experimental system for research on ultracold atomic gases near superconducting microstructures

D. Cano[a], H. Hattermann, B. Kasch, C. Zimmermann, R. Kleiner, D. Koelle, and J. Fortágh

CQ Center for Collective Quantum Phenomena and their Applications, Physikalisches Institut, Eberhard-Karls-Universität Tübingen, Auf der Morgenstelle 14, 72076 Tübingen, Germany

Received 30 November 2010 / Received in final form 14 January 2011
Published online 27 April 2011 –

Abstract. We describe an experimental system that integrates the techniques for producing ultracold atomic gases with the techniques for cooling solid bodies to cryogenic temperatures. Ultracold clouds of ^{87}Rb are prepared in a trap setup based on room-temperature coils and subsequently transported to a superconducting microstructure by means of optical tweezers. The superconducting microstructure generates a magnetic microtrap and is cooled by a helium-flow cryostat that can achieve temperatures down to 2 K. Both the room-temperature trap setup and the superconducting microtrap are installed in the same ultra-high-vacuum chamber. The presented system is well suited to create hybrid quantum systems by combining ultracold atomic gases and superconducting devices.

1 Introduction

The idea of combining ultracold atomic gases and superconducting devices to create hybrid quantum systems has attracted considerable scientific interest in the last years. This is reflected by the number of recent theoretical proposals on the quantum state control of these systems [1–15]. Most of them examine the coherent coupling between ultracold gaseous clouds and superconducting circuits by means of the electromagnetic modes of a superconducting coplanar resonator. Important efforts are currently being put into the development of experimental systems to achieve such goals. Recently, different laboratories have been able to trap ultracold atoms near superconducting microstructures [16–26]. The first published results include the realization of a magnetic microtrap with a persistent current loop [17], the production of a Bose-Einstein condensate on a superconducting chip [18], the usage of magnetically trapped atoms to characterize the Meissner effect [19], the assessment of the impact of vortices on atomic spin-flip transitions [20], the realization of magnetic microtraps using the magnetic fields of superconducting vortices [23–25], and measurements of atomic spin-flip transitions as a function of the distance from a superconducting surface in comparison with a normal conducting surface [26].

This paper presents an experimental system to study the interactions between ultracold atomic gases and superconducting microstructures. The important components of the system are illustrated in Figure 1. Ultracold clouds of ^{87}Rb in the $|5\ ^2S_{1/2}, F = 2, m_F = 2\rangle$ state are prepared in a trap setup based on room-temperature coils. The techniques used for that purpose are in sequential order a magneto-optical trap (MOT) [27], polarization-gradient cooling [28] and evaporative cooling [29] in a magnetic Ioffe-Pritchard trap, similar to reference [30]. Subsequently, the ultracold atomic gas is transferred into an optical dipole trap that is formed by focusing a red-detuned gaussian beam with an achromatic lens (L1). The atoms are optically transported to a superconducting microstructure at the cold end of a helium-flow cryostat by moving the achromatic lens with a linear translation stage. These optical tweezers [31] are very suitable to transport the atoms between separate structures of different temperatures within the same vacuum chamber. Finally, the atoms are transferred into the magnetic microtrap generated by the superconducting microstructure. This system has been used to conduct experiments on the Meissner effect [19] and atomic lifetime measurements in the vicinity of superconducting surfaces [26].

2 Vacuum system for ultracold atoms and superconductors

The interior of the vacuum chamber is shown in Figure 2. It contains cold-atom traps based on room-temperature coils and a helium-flow cryostat holding superconducting microstructures and superconducting microtraps. The room-temperature trap setup consists of three pairs of coils – one pair for the six-beam MOT and two additional pairs for adiabatic compression – and two vertical wires (Ioffe wires). The coils have been wound by Kapton-insulated wires (1 mm in diameter) on mounts

[a] e-mail: cano@pit.physik.uni-tuebingen.de

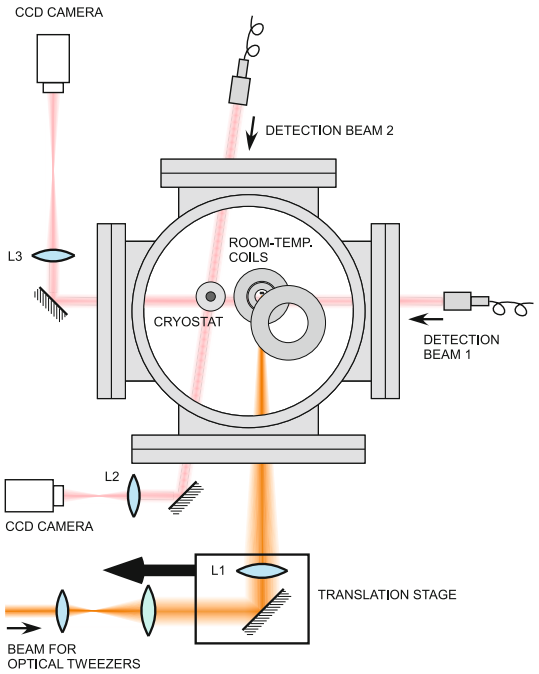

Fig. 1. (Color online) Sketch of the system as seen from above. Experiments take place in an ultra-high-vacuum chamber with four big viewports. Its main parts are a trap setup based on room-temperature coils and a helium-flow cryostat. The room-temperature trap setup accomplishes the preparation of ultracold gases. The cryostat holds and cools a superconducting microstructure generating a magnetic microtrap. Optical tweezers are used to transport the atoms from the room-temperature trap setup to the superconducting microtrap. Also depicted is the detection system. Beams 1 and 2 are used for absorption imaging of the atoms.

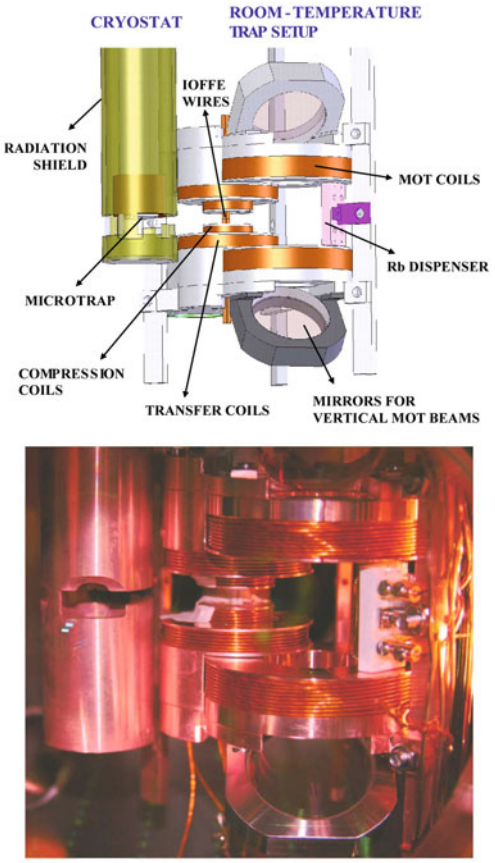

Fig. 2. (Color online) Drawing and photograph of the room-temperature trap setup and the cryostat inside the vacuum chamber (see text).

made of OFHC copper. Thin radial cuts were made in the coil holders in order to minimize eddy currents. The Ioffe wires (1.5 mm in diameter) are electrically isolated by a thin layer of ceramic epoxy. This epoxy favors the thermal contact between the Ioffe wires and the rest of the room-temperature structure. Two dielectric mirrors direct the vertical beams of the six-beam MOT. The system employs two rubidium dispensers as source of rubidium atoms at 22 mm distance from the MOT center.

The superconducting microstructure is attached to the cold end of a helium-flow cryostat. The lower parts of the cryostat are surrounded by a radiation shield that intercepts thermal radiation, thus reducing the heat load on the microstructure. The radiation shield is a hollow cylinder made of gold-plated OFHC copper. A small cut in the shield allows optical access for the optical tweezers and imaging.

The vacuum system is operated at a base pressure of 10^{-11} mbar (Fig. 3). This is achieved by an ion-getter pump (IP) (75 L/s pumping speed) and a titanium sublimation pump (TiP). During the experiments, the TiP pump is cooled with liquid nitrogen to increase its pumping speed, which is of the order of 10^4 L/s. The top flange of the vacuum chamber has a long vertical extension (C) that encloses the cryostat. This vertical extension has a translator (T) that allows changing the vertical position of the cryostat as desired. A reservoir (R) on the top flange contains a coolant that absorbs the heat dissipated by the currents applied to the room-temperature coils of the trap setup. The room-temperature trap setup is thermally connected to that reservoir through a thick metallic bar. The top flange also includes some electrical feedthroughs (F) that transfer electric current through the chamber wall to the room-temperature trap setup. After assembly, the vacuum chamber has been baked out at 200 °C for ten days.

3 Room-temperature trap setup

In order to complete the preparation of the ultracold cloud in the room-temperature trap setup, the MOT phase and polarization-gradient cooling are followed by radiofrequency evaporative cooling. For this purpose the atom cloud is adiabatically transferred from the MOT position into an Ioffe-Pritchard trap that satisfies the required conditions of strong confinement and non-zero magnetic field. The transfer starts with the atoms in the quadrupole trap generated by the MOT coils (see Fig. 4). First, the currents in the Ioffe-wires are turned on (opposite currents

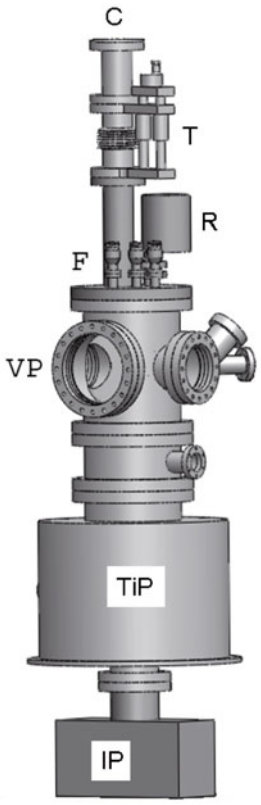

Fig. 3. Vacuum system. Optical access to the trap setup is provided by large viewports (VP) (CF100 and CF160). The trap setup is attached to the top flange (CF200). The top flange includes a coolant reservoir (R), electrical feedthroughs (F), a vertical extension (C) to enclose the cryostat and a translator (T) to position the cryostat. The system is pumped by an ion-getter pump (IP) and a titanium sublimation pump (TiP).

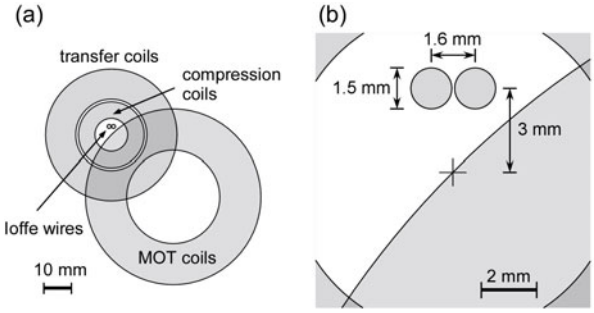

Fig. 4. Top view of the coils and wires that form the room-temperature trap setup (to scale). The right side shows a magnified part in front of the Ioffe wires. The diameter of the Ioffe wires is 1.5 mm.

of 14.5 A). They do not significantly influence the initial trap, but will determine the position and trap geometry after the transfer. Next, by changing the electric currents applied to the MOT coils and the transfer coils, the magnetic quadrupole trap is moved from the position of the MOT to the position of the Ioffe-Pritchard trap. The evolution of the currents is a succession of linear ramps, as shown in Figure 5. The Ioffe-Pritchard trap forms at the

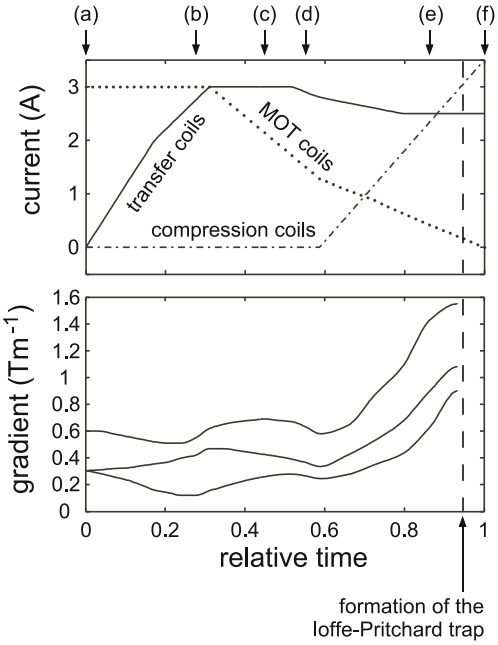

Fig. 5. Upper graph: evolution of the electric currents in the MOT coils, the transfer coils and the compression coils during the magnetic transfer. Lower graph: magnetic gradients in the three main perpendicular axes of the magnetic quadrupole trap. The Ioffe trap forms at the end of the magnetic transfer. In the Ioffe trap the currents in the compression coils and in the transfer coils are 3.5 A and 2.5 A, respectively, and the two Ioffe wires carry opposite currents of 14.5 A. The six labels, (a) to (f), indicate the times of the plots shown in Figure 6.

Table 1. Description of the MOT-, transfer- and compression-coils in the room-temperature trap setup. The vertical distance between coils is measured between the central points of the coils of each pair. The coils of every pair are driven with opposite currents to generate a quadrupole magnetic field. The magnetic gradient in the horizontal directions is half as large as in the vertical direction. The Kapton-insulated wires have a diameter of 1 mm.

	MOT	Trans.	Compr.
Inner radius (mm)	17	13	6
Outer radius (mm)	32	24	12
Thickness (mm)	10	6	10
Vertical distance (mm)	42	24	18
Number of windings	151	50	46
Vertical gradient (T/m/A)	0.20	0.15	0.40

end of the transfer. Figure 4b and Table 1 show the dimensions of the coils and wires that provide the trapping magnetic fields.

Figure 6 shows the isopotential lines of the magnetic-field modulus at six different times of the magnetic transfer, which correspond to the six labels (a)–(f) in Figure 5. Figure 6a shows the magnetic quadrupole trap at the initial time of the magnetic transfer, when only the MOT coils carry an electric current. Subsequently, the magnetic zero of the quadrupole trap is shifted towards the Ioffe-Pritchard trap by increasing the current in the transfer

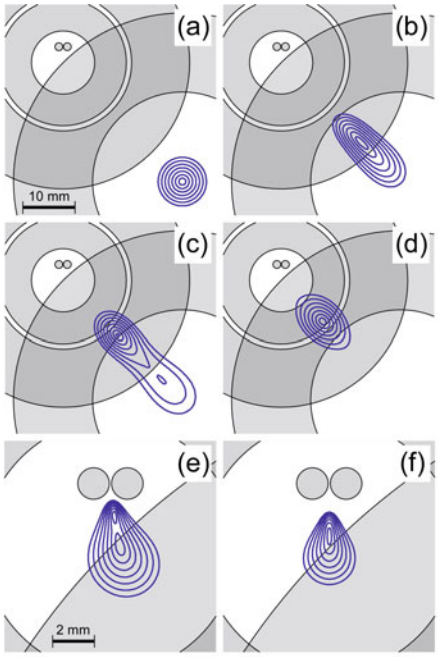

Fig. 6. (Color online) Isopotential lines of the magnetic-field modulus at six different times of the magnetic transfer, which correspond to the six labels in Figure 5. Graph (f) is the Ioffe-Pritchard trap in which evaporative cooling is carried out. The magnetic field changes by 0.2 mT per contour. The drawings are done to scale.

coils, as shown in Figure 6b. Figure 6c represents the time at which the trap becomes more dominated by the transfer coils than by the MOT coils. At this time a relative minimum of the magnetic potential is formed near the quadrupole trap. This relative minimum can trap some atoms that do not return to the quadrupole trap. Two recipes have been followed to increase the distance between this relative minimum and the center of the quadrupole trap, and in this way, to avoid significant loss of atoms. The first one is to not ramp down the current of the MOT coils until the current of the transfer coils has reached its maximum value. The second recipe is that the distance between the axis of the MOT coils and that of the transfer coils should be equal or shorter than the outer radius of the MOT coils.

At the end of the transfer, the currents in the compression coils are ramped up. This increases the magnetic gradient and brings the quadrupole trap closer to its final position. Before the Ioffe-Pritchard configuration is reached, a second quadrupole trap comes up near the Ioffe wires (see Fig. 6e). Finally, as the current in the MOT coils is reduced, the two quadrupole traps, which have perpendicular axes, merge and the Ioffe-Pritchard trap forms. If the currents in the Ioffe wires were ramped up at the end of the transfer instead of at the beginning, the second quadrupole trap would be too close to the Ioffe wire surface, thus reducing the trap depth during the transformation of the two quadrupole traps into the Ioffe-Pritchard trap. For that reason, thick Ioffe wires in this configuration shall be driven with electric currents since the beginning of the transfer. The minimum trap depth during the whole magnetic transfer is 1.1 mT, which corresponds to a temperature of $\simeq$750 μK. The magnetic field at the center of the final trap is 10^{-4} T, which is enough to avoid atom losses by Majorana spin-flip transitions [32] during evaporative cooling. The radial and longitudinal oscillation frequencies are $\omega_r = 2\pi \times 210$ s^{-1} and $\omega_l = 2\pi \times 30$ s^{-1}, respectively. After evaporative cooling the ultracold cloud contains 3×10^6 atoms at 2.5 μK.

4 Optical tweezers for ultracold atoms

The transport of the prepared atom cloud from the room-temperature trap setup into the superconducting microtrap is accomplished using optical tweezers [31]. After evaporative cooling in the magnetic Ioffe-Pritchard trap, the atoms are transferred into an optical dipole trap. This employs a multimode ytterbium fiber laser at $\lambda =$ 1064 nm. The $1/e^2$ beam waist radius is 15 μm at the focal position, around which the atoms are trapped. The transfer is accomplished by ramping the laser light up to 350 mW in 200 ms and then ramping down the trapping magnetic field in 20 ms. The corresponding trap depth is 130 μK and the scattering rate of photons by the atoms is about 1 s^{-1}.

The radial and longitudinal oscillation frequencies of the dipole trap are $\omega_r = 2\pi \times 2300$ s^{-1} and $\omega_l = 2\pi \times 37$ s^{-1}, respectively. The longitudinal axis of the optical dipole trap is parallel to the longitudinal axis of the Ioffe-Pritchard trap. The oscillation frequencies of the optical dipole trap are different from those of the initial magnetic Ioffe-Pritchard trap. This mode mismatch is the most probable cause of the observed sudden increase of temperature by about 1 μK. Just after the transfer there is a quick loss of the hottest atoms (about 20%), and the corresponding re-thermalization results in a cloud with 2.5×10^6 atoms at 2.5 μK in the optical dipole trap.

Once the optical dipole trap is loaded, the atom cloud is optically transported over a distance of 44 mm to the cold surface of the cryostat. For this purpose the focussing lens is moved with an air-bearing linear translation stage which is placed outside the vacuum chamber (Fig. 1). The air-bearing stage (Aerotech, Model ABL 1000) is levitated with pressurized air and is driven by a brushless servo motor that guarantees minimal vibration and that has an accuracy of 0.2 μm. Smooth transport is accomplished within 0.5 s using a sinusoidal acceleration profile with a maximum acceleration of 1 m/s^2. Both smooth transport and minimal vibration are adiabatic requirements because fluctuations in the trap position heat the ultracold atom cloud [33]. With this acceleration profile there are no observable oscillations of the atomic cloud at the end of the optical transport. In this setup the optical dipole trap moves in the direction of highest confinement, thus compensating inertia even during a quick transport. There is neither observable atom loss nor increase of temperature due to optical transport.

The demand for thermal isolation between the superconducting microstructure and the rest of the chamber

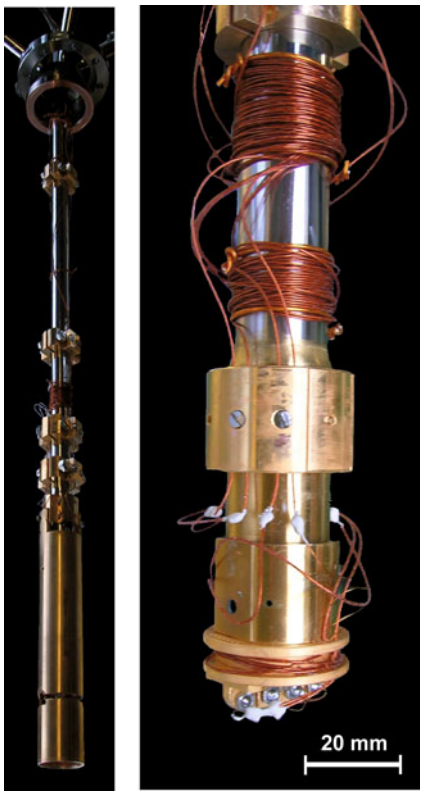

Fig. 7. (Color online) Flow cryostat (Janis research company, Model ST-400). Left: photo of the whole cryostat with a radiation shield that protects the microstructure from the room-temperature radiation. Right: cold end of the cryostat without the radiation shield. A superconducting microstructure is attached to the bottom surface.

restricts the possibilities of transporting the ultracold atom clouds from where they are produced into the superconducting microtrap. This technical difficulty, which does not exist in standard systems with normal conducting microtraps, has been overcome in the present apparatus by using optical tweezers. The optical dipole potential of the optical tweezers is independent of the magnetic potentials and is thus well suited to transport atoms between the trap setup at room temperature and the cold end of the cryostat.

5 Helium-flow cryostat

The superconducting microstructure is attached to the cold end of the cryostat shown in Figure 7. Liquid helium flows from a big storage dewar can through a transfer line to the lower parts of the cryostat, where it evaporates and cools the microstructure. Temperatures of about 2 K, below the boiling point of ^{4}He at ambient pressure, can be achieved when actively pumping the He gas at the return line of the cryostat. The He gas escapes upwards, cooling the outer surface of the cryostat. The outer surface of the cryostat is a 1-meter long tube made of stainless steel, and its temperature varies gradually from cryogenic temperatures in the lower parts to room temperature in the upper parts.

The electric currents applied to the microstructure are transferred through the walls of the vacuum chamber by means of some electrical feedthroughs located near the upper part of the cryostat. The currents are conducted through Kapton-insulated wires (0.25 mm in diameter) between the electrical feedthroughs and the microstructure. The wires are gradually cooled at different positions along the cryostat by means of wire holders that are firmly attached to the outer surface of the cryostat. The thermal paths between the microstructure and the feedthroughs are increased by making the wires much longer than the cryostat. Hence the wires have to be wound around the cryostat as shown in Figure 7. The length of the wires is chosen to trade off heat flux against resistive heating.

The radiation shield is mounted to a thermal anchor on the cryostat surface, and reaches temperatures of about 25 K. Because of the low thermal conductivity of oxide, every copper surface on the cryostat is gold plated in order to prevent the copper surface from oxidation. This is accomplished by electro-chemical deposition in a gold cyanide bath at 60 °C. Just before electro-chemical deposition, the oxide layers on the copper surface are removed with an aqueous solution with a strong detergent (Tickopur RW 77).

Certain measures must be taken concerning the long shape of the cryostat in order to guarantee the correct operation of the whole experimental system. Because the cryostat is basically a long structure suspended from its upper parts, mechanical vibrations at certain frequencies are enhanced at its cold end. This might result in heating and loss of atoms in the superconducting microtrap. To reduce the effect of environmental vibrations the vacuum chamber is resting on an optical table the legs of which include a standard pneumatic isolation system. In addition, the whole experimental system is installed in a basement with a very low level of vibrations and noise. Another possible drawback of the long shape of the cryostat could be the high sensitivity of its length to the temperature distribution. The cryostat shrinks by about 2 mm during cooling from room temperature to the final temperature. This is compensated with the vertical translator (T) shown in Figure 3. Once the microstructure reaches the final temperature, its vertical position oscillates slowly with a peak-to-peak amplitude lower than 10 microns and with a period of between 5 and 15 min. This oscillation is not detrimental to the alignment between optical tweezers and microtrap because the atom cloud during loading is much larger than the oscillation amplitude.

6 Ultracold atoms in the superconducting microstructure

A simple example of a superconducting microstructure with a typical configuration for trapping atoms has been installed in the cryostat. The generated microtrap is loaded with atoms from the optical tweezers. The superconducting microstructure is shown in Figure 8. It is

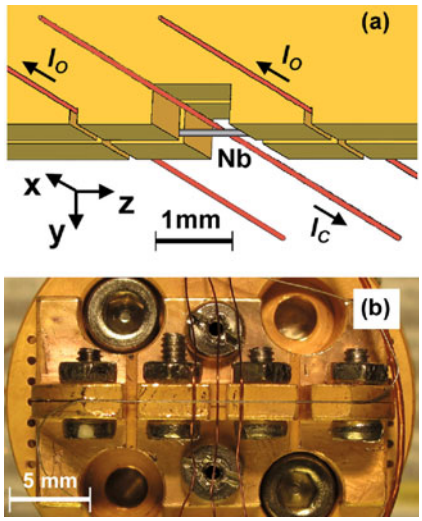

Fig. 8. (Color online) Superconducting microstructure. A bare niobium wire with circular cross section of diameter 125 μm is mechanically clamped between two copper plates by fastening four stainless-steel screws. The two copper plates are part of a larger piece that is firmly attached to the bottom surface of the cryostat. This ensures mechanical stability and good thermal contact. The whole copper piece was previously gold-plated in order to avoid oxide on its surface. The microstructure also includes three offset wires along the x-direction. These are Kapton insulated and 0.1-mm thick. The distance between them is 1.5 mm. The offset wires are located just above the Nb wire. A small cut in the copper holder gives free access to the Nb wire at the central part of the superconducting microtrap. Gravity is in the positive direction of the y-axis.

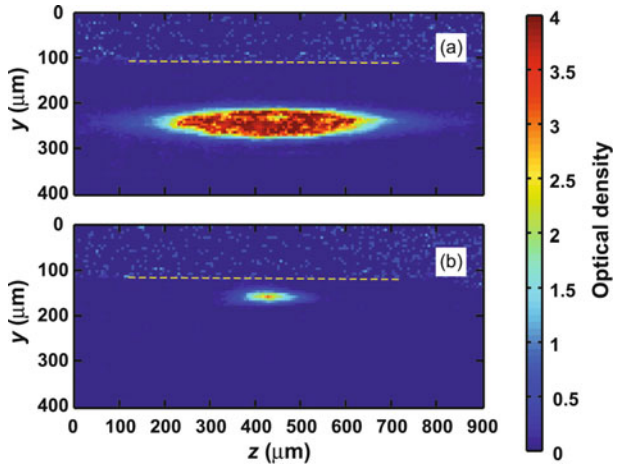

Fig. 9. (Color online) Absorption images of the atom cloud in the superconducting microtrap. The detection laser is in resonance with the $|5\ ^2S_{1/2}, F = 2\rangle \rightarrow |5\ ^2P_{3/2}, F = 3\rangle$ transition. The dashed line marks the surface of the superconducting wire. (a) Atomic cloud before evaporative cooling at 135 μm from the superconducting surface. (b) Atomic cloud after evaporative cooling at 45 μm from the superconducting surface.

a copper piece holding a superconducting niobium wire in the z-direction and three Kapton-insulated wires in the x-direction. The superconducting Nb wire is strongly clamped to guarantee a good thermal contact. The directions of the axes are indicated in Figure 8a. The Nb wire can be easily substituted by superconducting wires of other materials. Niobium was the preferred material for being the element with the highest critical temperature, $T_C = 9.2$ K. This microstructure, although easy to build, allows the realization of experiments on fundamental interactions between atomic gases and superconducting surfaces [19,26].

The generated magnetic microtrap has the same configuration as in previous experiments with normal conducting wires [34–36]. A two-dimensional confining magnetic field is created by the circular magnetic field of the current through the Nb wire in combination with a homogeneous bias field parallel to the x-axis. The atoms are radially confined around the positions where both fields cancel. Therefore, the magnetic guide forms around a straight line that is parallel to the Nb wire and that is included in the plane $x = 0$. The bias field is generated by two Helmholtz coils outside the vacuum chamber.

An homogeneous offset field of 0.2 mT parallel to the z-axis is applied in order to reduce atom losses due to Majorana spin-flip transitions [32]. This is accomplished with a second pair of external Helmholtz coils. Longitudinal confinement in the z-direction is achieved by superimposing the inhomogeneous offset field of the currents I_0 in the two side offset wires. The longitudinal confinement is increased by means of the current I_C in the central offset wire. The current I_C reduces the offset field in the vicinity of the trap center, thus deepening the microtrap and increasing its longitudinal confinement.

The atoms are loaded from the optical tweezers into the superconducting microtrap at a distance from the Nb surface that can vary between 200 and 500 μm. This is accomplished by ramping up the magnetic fields of the microtrap within 100 ms, and subsequently ramping down the laser power to zero in 0.5 s. The longitudinal axes of the microtrap and the optical dipole trap are perpendicular to each other. This reduces the efficiency of the loading process to only 40%. This low efficiency is not very harmful because the lost atoms come mainly from the hottest portion of the atomic cloud, so the atom loss during the loading process is accompanied by a decrease of temperature of the trapped gas. The loading process results in a cloud with 10^6 atoms at about 1 μK. After loading, the microtrap can be positioned at the desired distance from the solid surface by changing the bias field and/or the current of the Nb wire.

Bose-Einstein condensates can be produced through further evaporative cooling. Evaporative cooling is realized with a radiofrequency wave applied to the superconducting wire for 11 s. Clouds of 1.5×10^5 atoms with phase-space densities of up to 2 have been produced in the superconducting microtrap. Typical temperatures after evaporative cooling are around 150 nK. Figure 9 shows absorption images of the atom cloud before and after evaporative cooling. The radial and longitudinal oscillation frequencies of the microtrap during evaporative cooling are $\omega_r = 2\pi \times 135\ \mathrm{s}^{-1}$ and $\omega_l = 2\pi \times 21\ \mathrm{s}^{-1}$, respectively.

7 Conclusion

This experimental system provides appropriate conditions for investigating fundamental interactions between cold atoms and superconducting surfaces. Its feasibility has been proved with a simple example of a superconducting microstructure with a typical configuration for trapping ultracold atoms. Optical tweezers are particularly useful in this kind of experimental system because the gases can be prepared under optimal conditions in a room-temperature trap setup and afterwards moved into the cryogenic environment of the superconducting microstructure. The inclusion of more sophisticated superconducting microstructures will enable the realization of hybrid quantum systems combining ultracold gases and superconducting circuits with future applications to quantum computation.

This work was supported by the DFG (SFB TRR 21, Project C2).

References

1. A.S. Sørensen, C.H. van der Wal, L.I. Childress, M.D. Lukin, Phys. Rev. Lett. **92**, 063601 (2004)
2. S. Scheel, P.K. Rekdal, P.L. Knight, E.A. Hinds, Phys. Rev. A **72**, 042901 (2005)
3. P. Rabl, D. DeMille, J.M. Doyle, M.D. Lukin, R.J. Schoelkopf, P. Zoller, Phys. Rev. Lett. **97**, 033003 (2006)
4. U. Hohenester, A. Eiguren, S. Scheel, E.A. Hinds, Phys. Rev. A **76**, 033618 (2007)
5. S. Scheel, R. Fermani, E.A. Hinds, Phys. Rev. A **75**, 064901 (2007)
6. D. Cano, B. Kasch, H. Hattermann, D. Koelle, R. Kleiner, C. Zimmermann, J. Fortágh, Phys. Rev. A **77**, 063408 (2008)
7. K. Tordrup, K. Mølmer, Phys. Rev. A **77**, R020301 (2008)
8. D. Petrosyan, M. Fleischhauer, Phys. Rev. Lett. **100**, 170501 (2008)
9. D. Petrosyan, G. Bensky, G. Kurizki, I. Mazets, J. Majer, J. Schmiedmayer, Phys. Rev. A **79**, R040304 (2009)
10. A. Imamoglu, Phys. Rev. Lett. **102**, 083602 (2009)
11. J. Verdú, H. Zoubi, Ch. Koller, J. Majer, H. Ritsch, J. Schmiedmayer, Phys. Rev. Lett. **103**, 043603 (2009)
12. R. Fermani, S. Scheel, J. Phys. B: At. Mol. Opt. Phys. **43**, 025001 (2010)
13. K. Henschel, J. Majer, J. Schmiedmayer, H. Ritsch, Phys. Rev. A **82**, 033810 (2010)
14. R. Fermani, T. Müller, B. Zhang, M.J. Lim, R. Dumke, J. Phys. B: At. Mol. Opt. Phys. **43**, 095002 (2010)
15. V. Sokolovsky, L. Prigozhin, V. Dikovsky, Supercond. Sci. Technol. **23**, 065003 (2010)
16. T. Nirrengarten, A. Qarry, C. Roux, A. Emmert, G. Nogues, M. Brune, J.-M. Raimond, S. Haroche, Phys. Rev. Lett. **97**, 200405 (2006)
17. T. Mukai, C. Hufnagel, A. Kasper, T. Meno, A. Tsukada, K. Semba, F. Shimizu, Phys. Rev. Lett. **98**, 260407 (2007)
18. C. Roux, A. Emmert, A. Lupascu, T. Nirrengarten, G. Nogues, M. Brune, J.-M. Raimond, S. Haroche, Europhys. Lett. **81**, 56004 (2008)
19. D. Cano, B. Kasch, H. Hattermann, R. Kleiner, C. Zimmermann, D. Koelle, J. Fortágh, Phys. Rev. Lett. **101**, 183006 (2008)
20. G. Nogues, C. Roux, T. Nirrengarten, A. Lupascu, A. Emmert, M. Brune, J.-M. Raimond, S. Haroche, B. Plaçais, J.-J. Greffet, Europhys. Lett. **87**, 13002 (2009)
21. C. Hufnagel, T. Mukai, F. Shimizu, Phys. Rev. A **79**, 053641 (2009)
22. A. Emmert, A. Lupascu, M. Brune, J.-M. Raimond, S. Haroche, G. Nogues, Phys. Rev. A **80**, R061604 (2009)
23. F. Shimizu, C. Hufnagel, T. Mukai, Phys. Rev. Lett. **103**, 253002 (2009)
24. T. Müller, B. Zhang, R. Fermani, K.S. Chan, Z.W. Wang, C.B. Zhang, M.J. Lim, R. Dumke, New J. Phys. **12**, 043016 (2010)
25. T. Müller, B. Zhang, R. Fermani, K.S. Chan, M.J. Lim, R. Dumke, Phys. Rev. A **81**, 053624 (2010)
26. B. Kasch, H. Hattermann, D. Cano, T.E. Judd, S. Scheel, C. Zimmermann, R. Kleiner, D. Koelle, J. Fortágh, New J. Phys. **12**, 065024 (2010)
27. C.G. Townsend, N.H. Edwards, C.J. Cooper, K.P. Zetie, C.J. Foot, Phys. Rev. A **52**, 1423 (1995)
28. J. Dalibard, C. Cohen-Tannoudji, J. Opt. Soc. Am. A **6**, 2023 (1989)
29. W. Ketterle, N.J. van Druten, Adv. At. Mol. Opt. Phys. **37**, 181 (1996)
30. J. Fortágh, H. Ott, S. Kraft, A. Günther, C. Zimmermann, Appl. Phys. B **76**, 157 (2003)
31. T.L. Gustavson, A.P. Chikkatur, A.E. Leanhardt, A. Görlitz, S. Gupta, D.E. Pritchard, W. Ketterle, Phys. Rev. Lett. **88**, 020401 (2002)
32. C.V. Sukumar, D.M. Brink, Phys. Rev. A **56**, 2451 (1997)
33. T.A. Savard, K.M. O'Hara, J.E. Thomas, Phys. Rev. A **56**, R1095 (1997)
34. R. Folman, P. Krüger, J. Denschlag, C. Henkel, J. Schmiedmayer, Adv. At. Mol. Opt. Phys. **48**, 263 (2002)
35. J. Fortágh, C. Zimmermann, Rev. Mod. Phys. **79**, 235 (2007)
36. A. Günther, S. Kraft, C. Zimmermann, J. Fortágh, Phys. Rev. Lett. **98**, 140403 (2007)

Publication 2

D. Cano, B. Kasch, H. Hattermann, R. Kleiner, C. Zimmermann, D. Koelle, and J. Fortágh,
Meissner Effect in Superconducting Microtraps,
Phys. Rev. Lett. **101**, 183006 (2008).

Meissner Effect in Superconducting Microtraps

D. Cano, B. Kasch, H. Hattermann, R. Kleiner, C. Zimmermann, D. Koelle, and J. Fortágh

Physikalisches Institut, Eberhard-Karls-Universität Tübingen, CQ Center for Collective Quantum Phenomena and their Applications, Auf der Morgenstelle 14, D-72076 Tübingen, Germany

(Received 20 August 2008; published 31 October 2008)

We report on the realization and characterization of a magnetic microtrap for ultracold atoms near a straight superconducting Nb wire with circular cross section. The trapped atoms are used to probe the magnetic field outside the superconducting wire. The Meissner effect shortens the distance between the trap and the wire, reduces the radial magnetic-field gradients, and lowers the trap depth. Measurements of the trap position reveal a complete exclusion of the magnetic field from the superconducting wire for temperatures lower than 6 K. As the temperature is further increased, the magnetic field partially penetrates the superconducting wire; hence the microtrap position is shifted towards the position expected for a normal-conducting wire.

DOI: 10.1103/PhysRevLett.101.183006 PACS numbers: 34.35.+a, 37.10.Gh

Microfabricated magnetic traps for cold atoms provide an intriguing physical scenario in which solid-state and atomic physics converge. Coherent control over the internal and external states of atomic quantum gases has already been achieved by means of magnetic potentials near microfabricated surfaces [1]. These advances led to a number of fundamental studies of atom-surface interactions such as the Casimir-Polder force [2], the spin decoherence of atoms near dielectric bodies [3–5], and the usage of trapped atoms to probe local irregularities of magnetic and electric fields near conductive films [6–8]. Superconductors are expected to play an essential role in this emerging field of research because they can provide an extremely low noise environment for trapped atoms [9]. Increased atomic coherence times at very short distances from superconducting surfaces will allow the manipulation of atomic wave functions even on the submicron scale. Also, it is likely that superconducting microstructures will have important applications such as novel hybrid quantum systems combining superconductors and coherent atom clouds. They include atomic hyperfine transitions coupled to local microwave sources made of Josephson junctions, or even quantum computation with superconducting devices that are coherently coupled to polar molecules [10] or Rydberg atoms [11].

Recent experiments demonstrated the feasibility of superconducting microtraps [12,13] and the trapping of atoms nearby a persistent current loop [14]. The impact of the Meissner effect on the microtrap has been assessed so far only theoretically [15]. The observation of this fundamental property of superconductors requires short enough distances between the atoms and the superconducting surface. Understanding how the Meissner effect distorts magnetic potentials is a prerequisite for a new experimental regime in which the advantages of superconducting microstructures can be fully exploited.

In this Letter we report on the realization of a magnetic microtrap for ultracold ^{87}Rb atoms near a superconducting niobium wire with circular cross section. By monitoring the position of the atom cloud, we observe that the Meissner effect influences the magnetic trap. Total field exclusion from the Nb wire is observed for temperatures below 6 K. As the temperature of the Nb wire is increased, the magnetic field gradually penetrates into the wire. Analytical expressions describing the magnetic trap are deduced by approximating the superconducting wire to a perfectly diamagnetic cylinder.

The experimental system integrates the techniques for producing ultracold atomic quantum gases with the techniques for cooling solid bodies to cryogenic temperatures. A standard, room-temperature trap setup for cooling atoms and a helium flow cryostat (ST-400 Janis) for operating superconducting microstructures are installed next to each other in a single vacuum chamber (Fig. 1). The vacuum chamber is evacuated to 10^{-11} mbar by an ion pump and a titanium-sublimation pump. The transport of atoms from the room-temperature trap setup to the cryogenically cooled superconducting microstructure is accomplished by means of optical tweezers [16]. Such an arrangement is appropriate for trapping ultracold atoms in superconducting microstructures which have to be thermally isolated from the environment and surrounded by a radiation shield.

The central piece of the experiment is a superconducting niobium wire with circular cross section of diameter 125 μm (Fig. 2). The Nb wire is mechanically clamped between two gold-plated copper plates which are firmly attached to the helium cryostat. This ensures mechanical stability and good thermal contact between the wire and the cryostat. The Nb wire is parallel to the z axis. The microtrap is realized by applying an electric current I_{Nb} to the Nb wire and a homogeneous bias field $\boldsymbol{B}_B$ along the x direction. Thus paramagnetic atoms can be radially confined around a line parallel to the Nb wire, where $\boldsymbol{B}_B$ cancels the circular magnetic field of I_{Nb}. The microtrap is closed in the longitudinal direction by the magnetic field of two offset wires driven with equal currents I_0 along the x

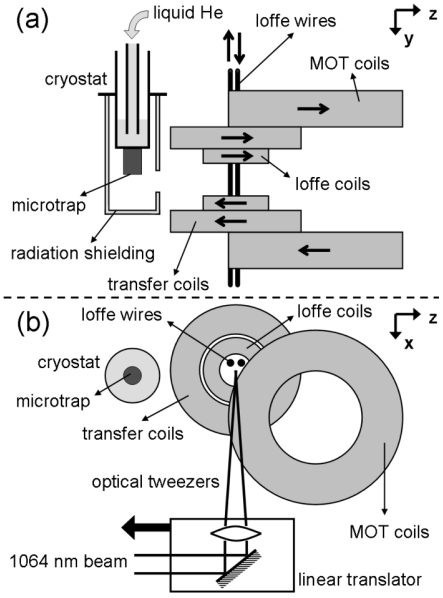

FIG. 1. Front view (a) and top view (b) of the experimental system. A single vacuum chamber contains a standard room-temperature trap setup (to the right) and a superconducting microtrap on a helium flow cryostat (to the left). Atoms are initially prepared in MOT and magnetic trap, and subsequently transported to the superconducting microtrap by means of optical tweezers. The optical tweezers are translated over 44 mm with an air-bearing translation stage outside the vacuum chamber.

direction. The offset wires are separated by 3 mm. Since the Nb wire is electrically not isolated from the Cu piece, the applied current I_{Nb} will entirely flow along the Nb wire only if this has no electrical resistance. Therefore, no microtrap can form in the normal-conducting state. Transition to superconductivity is measured at $T_c = 9.2$ K with a four-point probe.

The atoms are loaded into the superconducting microtrap with the experimental procedure described below. Rubidium atoms (^{87}Rb) from a dispenser are trapped and cooled in a six-beam magneto-optical trap (MOT) . After

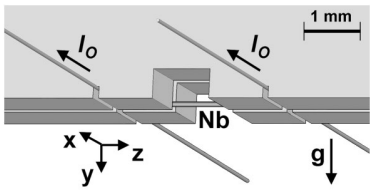

FIG. 2. Superconducting microtrap. The trap is generated below the Nb wire by applying a current I_{Nb} and a bias field $\boldsymbol{B}_B$ in the x direction. The Nb wire with circular cross section of diameter 125 μm is clamped in a slit of a gold-plated copper holder which is attached to the cryostat. It can be cooled to variable temperatures down to 4.2 K. A small cut in the copper holder gives free access to the Nb wire at the central part of the microtrap. A pair of kapton-insulated offset wires along the x direction, just above the Nb wire, are used for the axial confinement. Gravity is along the y direction.

polarization gradient cooling and optical pumping to the $|5S_{3/2}, F = 2, m_F = +2\rangle$ state the atoms are trapped in the quadrupole magnetic trap generated by the MOT coils. The atoms are then magnetically transferred via two transfer coils into an Ioffe-Pritchard trap which is generated by two smaller coils and a pair of wires parallel to the coil axis [17], as shown in Fig. 1. The strong confinement of this trap with radial and longitudinal oscillation frequencies of $\omega_r = 2\pi \times 272\ \mathrm{s}^{-1}$ and $\omega_l = 2\pi \times 45\ \mathrm{s}^{-1}$, respectively, allows for efficient evaporative cooling. Radio frequency evaporative cooling is applied for 13 s to obtain a thermal cloud of 7×10^5 atoms at 2.5 μK [18].

After evaporative cooling the atoms are transferred into an optical dipole trap which is formed by focusing a 1064-nm laser with a 250-mm achromatic lens to a $1/e^2$ beam waist radius of 18 μm. The oscillation frequencies of the dipole trap are $\omega_r = 2\pi \times 2100\ \mathrm{s}^{-1}$ and $\omega_l = 2\pi \times 30\ \mathrm{s}^{-1}$. The transfer is accomplished by ramping the laser light up to 500 mW in 200 ms and then ramping down the magnetic field in 20 ms. Next, the atom cloud is transported with the optical tweezers from the Ioffe-Pritchard trap over a distance of 44 mm to the cold surface of the cryostat. For this purpose, the 250-mm lens is moved with an air-bearing linear translation stage (Aerotech, ABL 1000), which is placed next to the vacuum chamber (Fig. 1). The air-bearing stage is levitated with pressurized air and is driven by a brushless servomotor that guarantees minimal vibration and that has an accuracy of 0.2 μm. Smooth transport is accomplished within 0.5 s using a sinusoidal acceleration profile with a maximum acceleration of 1 m/s^2.

The atoms are loaded from the optical tweezers into the superconducting microtrap at a distance of 500 μm from the Nb wire. This is accomplished by ramping up the magnetic fields of the microtrap within 100 ms, and subsequently ramping down the laser power to zero in 0.5 s. The microtrap is generated by $|\boldsymbol{B}_B| = 0.64$ mT, $I_{\mathrm{Nb}} = 1.6$ A and $I_0 = 0.01$ A. A homogeneous offset field $|\boldsymbol{B}_0| = 0.1$ mT along the z direction is additionally applied to reduce Majorana losses [19]. Both $\boldsymbol{B}_B$ and $\boldsymbol{B}_0$ are created by Helmholtz coils outside the vacuum chamber. Trap frequencies are $\omega_r = 2\pi \times 160\ \mathrm{s}^{-1}$ and $\omega_l = 2\pi \times 2\ \mathrm{s}^{-1}$. The microtrap is loaded with 4×10^5 atoms at 5 μK.

As the atoms are forced into the minimum of the magnetic trap, they can be used to probe the magnetic-field profile near the superconducting wire, and in this way to assess the Meissner effect. The atoms are brought close to the Nb wire by reducing I_{Nb} while keeping $\boldsymbol{B}_B$, I_0, and $\boldsymbol{B}_0$ constant. The positioning of the cloud is accomplished within 0.5 s, which is adiabatic with respect to the motion of atoms inside the trap. We measure the position y_0 of the atom cloud with respect to the center of the Nb wire for different wire currents I_{Nb}. Data are obtained from absorption images as shown in Fig. 3.

The atom cloud in the microtrap is highly elongated due to the weak longitudinal confinement. In order to find the

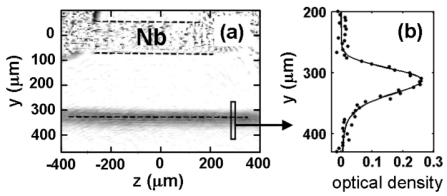

FIG. 3. (a) Absorption image of the atom cloud at the central region of the magnetic trap. The dashed lines represent the longitudinal axis of the trap and the Nb wire surface. (b) Optical density of one of the transverse sections of the atom cloud. The best-fit curve $\rho(y)$ is also plotted.

longitudinal axis of the trap accurately, the absorption image of the cloud is divided into transverse sections. For every transverse section, the measured atom density is fitted by the theoretical density $\rho(y)$ of a thermal cloud in a trapping potential $U(y, x)$, as seen in Fig. 3(b). The asymmetry of the atom density profile is due to the decrease in magnetic gradient with increasing y and, to a lesser extent, due to gravity. These two effects are included in $U(y, x)$. The maxima of $\rho(y)$ of all transverse sections of the atom cloud are fitted to a straight line, which is the longitudinal axis of the microtrap. The value of y_0 is calculated as the distance between the longitudinal axis of the trap and that of the Nb wire.

Figure 4(a) plots y_0 as a function of I_{Nb}. Data are represented in logarithmic scale to give more visibility to the points that are closer to the wire. Measurements were carried out for six different temperatures T of the Nb wire. The dependence of y_0 on T is noticeable only at the lowest values of y_0, where the impact of the Meissner effect is stronger. For every temperature, the measured data are fitted by a theoretical curve that assumes that the superconducting Nb wire behaves like a diamagnetic cylinder of effective radius R. For every temperature, the best-fit curve is found by varying the effective radius R. Figure 4(b) represents the best-fit radius R versus T.

For comparison, the microtrap positions calculated for the normal-conducting state are represented as a dashed curve. It is a straight line, slightly distorted by gravity. Above T_c of Nb, $\boldsymbol{B}_B$ penetrates the conductive wire and remains homogeneous, canceling the circular field of I_{Nb} at a distance from the wire center of $y_{0,\mathrm{NC}} = (\mu_0 I_{\mathrm{Nb}})/(2\pi B_B)$. The magnetic-field gradient in the radial directions around $y_{0,\mathrm{NC}}$ is $a_{\mathrm{NC}} = B_B/y_{0,\mathrm{NC}}$. The gravitational sag is a small quantity that can be calculated as $\Delta_{\mathrm{NC}} = (gmB_0)/(g_F\mu_B m_F a_{\mathrm{NC}}^2)$ [1].

Formulas describing the magnetic trap for the superconducting case are derived by approximating the Nb wire to a diamagnetic cylinder of effective radius R. Because of the axial symmetry, the magnetic field generated by I_{Nb} outside the superconducting wire is the same as in the normal case: $B_{\mathrm{Nb}} = (\mu_0 I_{\mathrm{Nb}})/(2\pi y)$. However, the bias field is strongly affected by the Meissner effect. The bias field on the y axis becomes $B_B(1 + R^2/y^2)\boldsymbol{e}_x$ [20]. In the superconducting case, the bias field cancels the circular field of I_{Nb} at a distance from the wire center of

$$y_{0,\mathrm{SC}} = \frac{\mu_0}{4\pi}\frac{I_{\mathrm{Nb}}}{B_B} + \sqrt{\left(\frac{\mu_0}{4\pi}\frac{I_{\mathrm{Nb}}}{B_B}\right)^2 - R^2}. \quad (1)$$

The magnetic-field gradient around $y_{0,\mathrm{SC}}$ is

$$a_{\mathrm{SC}} = \frac{B_B}{y_{0,\mathrm{SC}}}\left[1 - \left(\frac{R}{y_{0,\mathrm{SC}}}\right)^2\right]. \quad (2)$$

The gravitational sag $\Delta_{\mathrm{SC}} = (gmB_0)/(g_F\mu_B m_F a_{\mathrm{SC}}^2)$ is always smaller than 4 μm and hardly affects the best-fit radius R. Even so, the effect of gravity on the trap position has been considered in the fitting procedure with the aim of

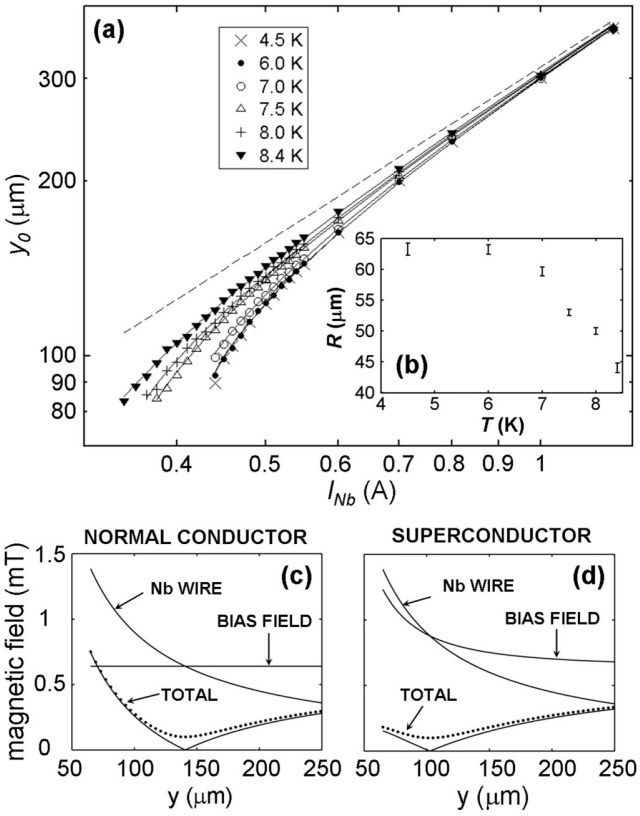

FIG. 4. (a) Distance between the trap center and the wire center as a function of the applied current I_{Nb} for six different temperatures. $|\boldsymbol{B}_B| = 0.64$ mT and $B_0 = 10^{-4}$ T. The normal-conducting case is represented as a dashed curve. The error bars, which result from the fitting procedure illustrated in Fig. 3, are smaller than the symbols and therefore not represented. (b) Best-fit radius as a function of the Nb wire temperature. The error bars represent the 95% confidence interval. (c),(d) Modulus of the magnetic-field profiles calculated for $I_{\mathrm{Nb}} = 0.45$ A for the normal-conducting and the superconducting cases, respectively. The comparison shows that the Meissner effect strongly distorts the bias field while leaving the field of I_{Nb} unchanged. This results in a lower trap depth and a shorter distance to the Nb wire. The realization of the microtrap requires that the bias field is opposite in direction to $\boldsymbol{B}_{\mathrm{Nb}}$. The additional offset field $B_0 = 10^{-4}$ T along the z direction changes the magnetic profile from linear to parabolic (dotted curve).

reducing the error of the obtained best-fit R. The measured data are fitted by the function $y_{0,\mathrm{SC}} + \Delta_{\mathrm{SC}}$. For every temperature, the root mean square of the difference between the measured points and the best-fit curve is lower than 2 μm, which demonstrates that the magnetic field outside the Nb wire can be well described by formulas relying on a diamagnetic cylinder.

The way in which the Meissner effect changes the trap parameters is explained in Figs. 4(c) and 4(d) by comparing the magnetic profiles in the superconducting and in the normal-conducting cases. The magnetic profile in the superconducting case is calculated assuming that the effective radius equals the real radius of the wire, $R = 62.5$ μm. The Meissner effect shortens the distance between the trap and the wire, reduces the radial magnetic-field gradients, and lowers the trap depth. The fact that the theoretical predictions for superconducting thin films reported in Ref. [15] follow a similar tendency suggests that this does not depend on the particular geometry of the superconductor.

The longitudinal confinement, which is very weak at the trap center because of the long distance between the offset wires, does not alter the trap parameters described in the above equations. It is also important to notice that the homogeneous offset field $\boldsymbol{B}_0$ is not distorted by the Meissner effect because the longitudinal demagnetizing factor of a long cylinder quickly tends to zero as its length increases to infinity.

For temperatures lower than 6 K, the best-fit radius R is very similar to the real radius of the wire. This is the expected value at such low temperatures, when the wire is in the pure Meissner state [21], i.e., when the magnetic flux penetrates the superconducting wire only to the London depth, which is for Nb some tens of nanometers [22]. As T is increased, the microtrap positions are shifted towards the positions expected for a normal-conducting wire. This is caused by an increase in the amount of magnetic flux penetrating the wire, which is manifested as a decrease of the effective radius R. The fact that the increase in temperature does not affect the points that are far from the wire demonstrates that the electric resistance remains zero, and so the applied current I_{Nb} flows entirely through the Nb wire. The experimental data reveal a smooth transition from the pure Meissner state to the normal state. For temperatures above 8.4 K, the atoms cannot be loaded into the microtrap because the critical current of the Nb wire drops below 1.6 A, which is the current I_{Nb} required to load the microtrap.

Another set of 160 measurements was taken at $T = 4.5$ K with different currents I_{Nb} in the range of 0.3–1.8 A and different bias fields in the range of 0.4–0.8 mT. By fitting the function $y_{0,\mathrm{SC}} + \Delta_{\mathrm{SC}}$ to the overall data, we obtain an effective radius of (61.5 ± 1.1) μm, which corroborates the presented results.

In conclusion, we demonstrated an experimental system that enables studies at the interface of cold atoms and superconductors. We measured the impact of the Meissner effect on the potential of a magnetic microtrap near a superconducting wire. The position of the atom cloud reveals complete field exclusion from the superconducting wire for temperatures below 6 K. For higher temperatures, the microtrap parameters are sensitive to the temperature of the superconducting wire. Even though transition from the pure Meissner state to the normal state usually consists of complex processes involving vortex formation and penetration-depth increase [23], the trapping field outside the wire can be well described by simple formulas relying on a diamagnetic cylinder of effective, temperature-dependent radius R. The Meissner effect will have important implications for experiments with quantum gases near superconducting surfaces.

We thank Thomas Dahm for useful discussions. This work was supported by the DFG (SFB TRR 21) and by the BMBF (NanoFutur 03X5506).

[1] J. Fortágh and C. Zimmermann, Rev. Mod. Phys. **79**, 235 (2007).
[2] J. M. Obrecht *et al.*, Phys. Rev. Lett. **98**, 063201 (2007).
[3] M. P. A. Jones *et al.*, Phys. Rev. Lett. **91**, 080401 (2003).
[4] D. M. Harber, J. M. McGuirk, J. M. Obrecht, and E. A. Cornell, J. Low Temp. Phys. **133**, 229 (2003).
[5] Y. J. Lin, I. Teper, C. Chin, and V. Vuletic, Phys. Rev. Lett. **92**, 050404 (2004).
[6] J. Estève *et al.*, Phys. Rev. A **70**, 043629 (2004).
[7] S. Wildermuth *et al.*, Appl. Phys. Lett. **88**, 264103 (2006).
[8] S. Aigner *et al.*, Science **319**, 1226 (2008).
[9] U. Hohenester, A. Eiguren, S. Scheel, and E. A. Hinds, Phys. Rev. A **76**, 033618 (2007).
[10] P. Rabl *et al.*, Phys. Rev. Lett. **97**, 033003 (2006).
[11] A. S. Sorensen, C. H. van der Wal, L. I. Childress, and M. D. Lukin, Phys. Rev. Lett. **92**, 063601 (2004).
[12] T. Nirrengarten *et al.*, Phys. Rev. Lett. **97**, 200405 (2006).
[13] C. Roux *et al.*, Europhys. Lett. **81**, 56004 (2008).
[14] T. Mukai *et al.*, Phys. Rev. Lett. **98**, 260407 (2007).
[15] D. Cano *et al.*, Phys. Rev. A **77**, 063408 (2008).
[16] T. L. Gustavson *et al.*, Phys. Rev. Lett. **88**, 020401 (2001).
[17] T. Bergeman, G. Erez, and H. J. Metcalf, Phys. Rev. A **35**, 1535 (1987).
[18] Bose-Einstein condensation is reached with 2×10^5 atoms by continuing evaporative cooling for another 5 s.
[19] C. V. Sukumar and D. M. Brink, Phys. Rev. A **56**, 2451 (1997).
[20] It is deduced from the surface current $\boldsymbol{K} = \boldsymbol{M} \times \boldsymbol{n}$ of the homogeneous magnetization $\boldsymbol{M} = -2\boldsymbol{B}_B/\mu_0$ in the dyamagnetic cylinder, where $\boldsymbol{n}$ is the unit vector perpendicular to the cylinder surface. A similar deduction for a sphere can be found in J. D. Jackson *Classical Electrodynamics* (John Wiley & Sons, New York, 1967), Chap. 5.
[21] F. London, *Superfluids* (Wiley, New York, 1950), Vol. I.
[22] B. W. Maxfield and W. L. McLean, Phys. Rev. **139**, A1515 (1965).
[23] J. B. Ketterson and S. N. Song, *Superconductivity* (Cambridge University Press, Cambridge, England, 1999).

Publication 3

B. Kasch, H. Hattermann, D. Cano, T.E. Judd, S. Scheel, C. Zimmermann, R. Kleiner, D. Koelle, and J. Fortágh,
Cold atoms near superconductors: atomic spin coherence beyond the Johnson noise limit,
New. J. Phys. **12**, 065024 (2010).

New Journal of Physics
The open-access journal for physics

Cold atoms near superconductors: atomic spin coherence beyond the Johnson noise limit

B Kasch[1,3], H Hattermann[1], D Cano[1], T E Judd[1], S Scheel[2], C Zimmermann[1], R Kleiner[1], D Koelle[1] and J Fortágh[1]

[1] Physikalisches Institut, Eberhard-Karls-Universität Tübingen, CQ Center for Collective Quantum Phenomena and their Applications, Auf der Morgenstelle 14, D-72076 Tübingen, Germany
[2] Quantum Optics and Laser Science, Blackett Laboratory, Imperial College London, Prince Consort Road, London SW7 2AZ, UK
E-mail: kasch@pit.physik.uni-tuebingen.de

New Journal of Physics **12** (2010) 065024 (8pp)
Received 3 December 2009
Published 28 June 2010
Online at http://www.njp.org/
doi:10.1088/1367-2630/12/6/065024

Abstract. We report on the measurement of atomic spin coherence near the surface of a superconducting niobium wire. As compared to normal conducting metal surfaces, the atomic spin coherence is maintained for time periods beyond the Johnson noise limit. The result provides experimental evidence that magnetic near-field noise near the superconductor is strongly suppressed. Such long atomic spin coherence times near superconductors open the way towards the development of coherently coupled cold atom/solid state hybrid quantum systems with potential applications in quantum information processing and precision force sensing.

Contents

[3] Author to whom any correspondence should be addressed.

1. Introduction

The construction of hybrid quantum systems that combine ultracold atoms with solid state devices has attracted considerable interest in recent years. A particular goal has been the exchange of quantum information between gaseous atoms and microchip devices. One of the most promising proposals for achieving this involves coupling a Cooper pair box to a cold atomic cloud via a superconducting stripline cavity [1]–[3]. Coupling of the Cooper pair box to the stripline cavity has already been achieved [4], but the device will also require long-lived coherent coupling between cold atoms and the superconducting microwave cavity, which is yet to be demonstrated. To fully realize the potential of such devices (e.g. the application of them as a hybrid quantum processor, where gate operations are performed by the solid state quantum device and the atomic spin states serve as quantum memory), it will be necessary to bring the atoms to within a few microns of the chip elements. However, the small separation between the atom cloud and the fabricated surface sets constraints on the atomic spin coherence.

Atoms trapped in a magnetic trap are subject to decoherence due to magnetic field fluctuations at the Larmor frequency, ω_{L}, which change the spin state of the atom. A natural source of magnetic field fluctuations is the thermally excited motion of electrons in a metal (Johnson noise). Recent experiments have shown that the spin decoherence rate of atoms increases strongly when the atom cloud is trapped close to a conducting surface [5]–[8]. The measured decoherence rates are of the order of $1\,\mathrm{s}^{-1}$ at a few tens of microns from bulk metals [5, 6] and about $10\,\mathrm{s}^{-1}$ near room temperature metallic thin films at micron atom–surface separations [7]. The decoherence rate decreases when the surface is cooled, as demonstrated on a 4.2 K gold thin film where rates of $0.1\,\mathrm{s}^{-1}$ have been measured for distances down to $20\,\mu$m [8]. The data confirmed theoretical predictions that Johnson-noise-induced field fluctuations limit the spin coherence of atoms [9, 10]. We note that Johnson noise has also been identified as a primary heating source in ions trapped in the vicinity of microscopic electrodes [11].

Unlike normal conductors, superconductors are expected to shield magnetic field fluctuations. Atomic spin decoherence near superconductors has been predicted to drop well below the Johnson noise limit of normal conductors [12] and any other experimentally relevant loss rates, such as vacuum background collisions and tunneling of atoms from the trap to the surface [7].

Here we report the observation of spin decoherence rates significantly below the Johnson noise limit in a hybrid system consisting of ultracold atoms and a superconducting surface. The coherence times are the longest yet observed in the vicinity of a highly conducting material and confirm the suppression of Johnson noise in superconductors. These results therefore support the suggestion that superconductors can be used to transfer quantum information between solids and gases.

2. Cold atoms near superconductors

Our experimental system combines a cold atom setup and a helium flow cryostat placed next to each other in ultrahigh vacuum at 6×10^{-11} mbar (figure 1). Initially, ultracold atoms are prepared via magneto-optical and magnetic trapping between room temperature electromagnets (figure 1, right). The cryostat (figure 1, left) holds superconducting structures on its cold end at a temperature of 4.2 K and is protected against thermal radiation by a thermal shield at a temperature of 20 K.

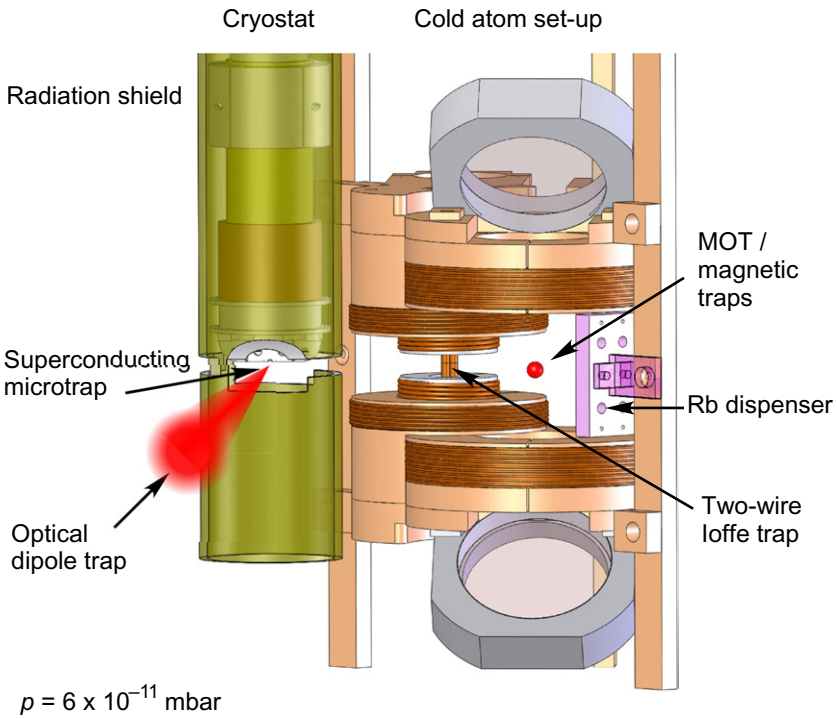

Figure 1. *In vacuo* trap setup. The cold atom setup (right) consists of a six-beam MOT, magnetic quadrupole traps and a two-wire Ioffe–Pritchard-type trap. The electromagnets are at room temperature. The MOT is loaded from a dispenser source. The ^{4}He flow cryostat (left) is mounted next to the room temperature setup. An optical dipole trap transports the atom cloud from the two-wire Ioffe trap to the cryogenic region. At the cold end of the cryostat, we operate a superconducting magnetic microtrap for cold atoms. The background pressure is $p \approx 6 \times 10^{-11}$ mbar.

At the beginning of the experimental cycle, a six-beam magneto-optical trap (MOT) is loaded from a pulsed rubidium dispenser. After standard polarization gradient cooling and optical pumping, the atoms in the $|F = 2, m_F = 2\rangle$ state are captured in a magnetic quadrupole trap and are subsequently transferred to a two-wire Ioffe–Pritchard-type magnetic trap [13]. The cloud is further cooled by forced radio-frequency evaporation to a temperature of 2.5 μK, before it is loaded adiabatically into the dipole potential of an optical tweezer beam (1064 nm, 0.8 W and beam waist $= 30\,\mu$m). The optical tweezers are used to transport the atoms to a position below the cryostat [14]. The horizontal translation of the beam waist over a distance of 44 mm is accomplished within 570 ms by translating the focusing lens of the tweezer beam outside the vacuum chamber on an air-bearing translation stage. At the cold end of the cryostat, we routinely load 10^6 ^{87}Rb atoms at a temperature of 1 μK into a magnetic microtrap that is generated near a superconducting niobium wire (diameter $d = 125\,\mu$m). The radial confinement is defined by the magnetic field of the current-carrying niobium wire and an external bias field perpendicular to the wire [15].

The niobium wire is clamped between solid copper blocks to ensure good thermal contact to the cryostat (figure 2). Due to the metallic contact between niobium and copper, the magnetic

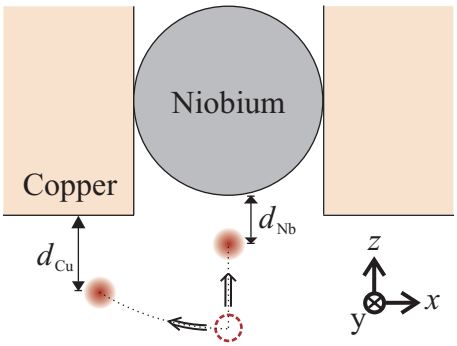

Figure 2. Geometry of the experiment for measuring atomic spin decoherence near superconducting niobium and normal conducting copper at $T = 4.2$ K. The 125 μm niobium wire is clamped between solid copper in order to ensure thermal contact. From an initial position, the cloud is moved closer to the niobium wire by reducing the current in the wire, or moved closer to the copper surface by rotating the external bias field about the wire axis.

trap can only be operated with the niobium wire in the superconducting state. The axial confinement is given by a pair of parallel pinch wires separated by 2 mm, running perpendicular to the niobium wire and mounted on the copper holder above the niobium wire [14]. An external homogeneous field parallel to the niobium wire axis is used to control the offset field in the magnetic trap. The distance between the atom cloud and the niobium wire d_{Nb} is controlled by the wire current (figure 2). The atom cloud can also be moved on a circular trajectory to the surface of the copper block by rotating the external bias field.

We calibrate the distance between the atom cloud and the niobium wire surface by means of *in situ* absorption images. The position of the atoms is measured for various currents in the niobium wire. For small currents the distance between the trap and the wire surface is shortened by the Meissner effect, deviating strongly from a normal conducting trap, where the distance to the wire center is strictly linear to the current. By creating a fit to the theoretical trap position (equation (1) of [14]), with the bias field as a free parameter and including gravity, we obtain the cloud–surface separation with an accuracy of ± 2 μm for any applied current.

The distance between the cloud and the copper surface is calibrated by imaging the circular trajectory on which the atom cloud moves when the bias field is rotated (figure 2). The current in the niobium wire and the modulus of the bias field are kept constant; thus the angle of rotation is given by the ratio of the vertical and horizontal magnetic fields. The position of the surface is determined by measuring the fields where all atoms are immediately lost. The method gives an accuracy of $+1/-3$ μm.

3. Exceptionally long atomic spin coherence near superconductors

Magnetic traps allow for a rather simple method of measuring the spin coherence of an atomic ensemble. Since in a conservative magnetic potential, only the low-field-seeking spin states are trapped, the spin decoherence rate of atoms can be derived from measurements of the magnetic trap lifetime [5]–[7]. We apply this method for measuring the spin coherence near superconducting niobium.

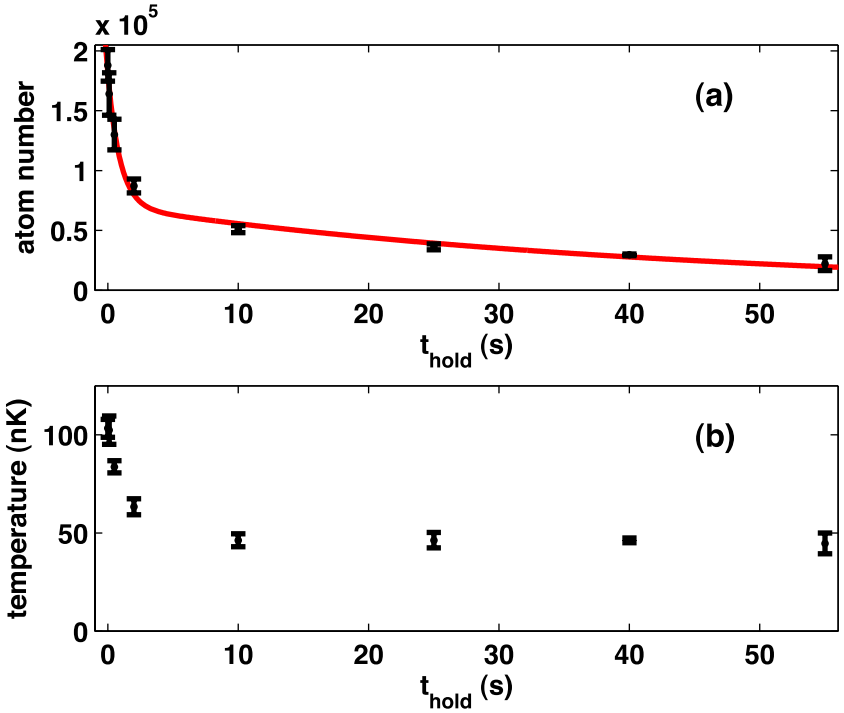

Figure 3. Time evolution of the number (a) and temperature (b) of an atom cloud held in a magnetic trap at a distance of 25 μm from niobium. After an initial atom loss due to surface evaporation on a timescale of $1/\Gamma_1$ (see text), the cloud decays exponentially with the rate Γ_2 and without measurable change in temperature.

For our niobium measurements, we use the following experimental sequence. The ^{87}Rb atom cloud is loaded into a magnetic microtrap near the superconducting niobium wire. The trap has radial frequency $\omega_r/2\pi = 135$ Hz and axial frequency $\omega_a/2\pi = 4$ Hz. The Larmor frequency is $\omega_L/2\pi = 1.71$ MHz for the spin-polarized hyperfine state $|F = 2, m_F = 2\rangle$ at $B_{off} = 2.44$ G. The cloud is cooled by forced evaporation for 11 s, whereby the temperature and atom number are reduced to $T \approx 100$ nK and $N \approx 2 \times 10^5$, respectively. The atom cloud is then moved in 1 s to a distance d_{Nb} from the niobium surface (figure 2) and held there for a variable hold time t_{hold}. During the shift toward the surface, the trap geometry changes: the Meissner effect reduces the radial frequency to less than 115 Hz at 20 μm in our trap geometry [14]. The offset field, which is the only critical parameter for spin decoherence, is kept constant. Bringing the thermal atom cloud close to the surface leads to truncation of the Gaussian density profile. The subsequent surface evaporation and rethermalization [6] reduce the number of atoms on a timescale of $1/\Gamma_1$ to typically 5×10^4 and the temperature to 50 nK (figure 3(b)). After the hold time t_{hold} the cloud is shifted away from the surface within 200 ms, after which the trap is turned off and the atoms are counted by absorption imaging after 5 ms time-of-flight.

For copper, we use a different trap configuration with frequencies $\omega_r/2\pi = 138$ Hz and $\omega_a/2\pi = 21$ Hz. The axial offset field is kept at the same value as in the niobium measurements. After evaporative cooling to $T \approx 300$ nK and $N \approx 2 \times 10^5$, the cloud is moved toward the copper, whereby surface cooling leads to a minimum temperature of $T \approx 150$ nK with $N \approx 5 \times 10^4$ atoms. All measurements have been made with thermal clouds.

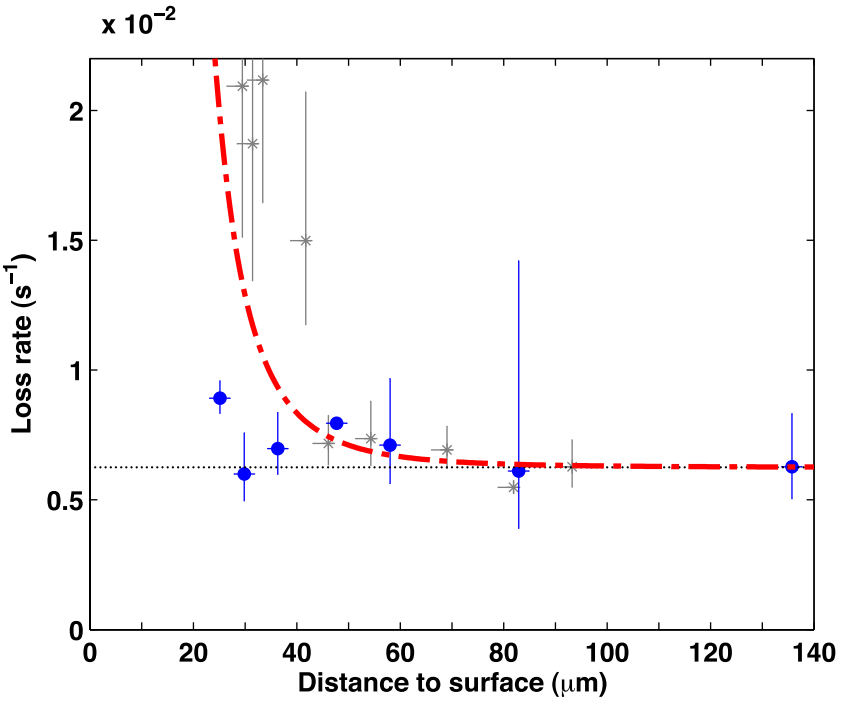

Figure 4. Atom loss rate near superconducting niobium at 4.2 K (blue circles) as a function of the atom–surface separation. The dash-dotted line (red) is the Johnson noise loss rate near normal conducting copper at 4.2 K (see equation (2)) including the measured vacuum background loss (black dotted line). The data below the Johnson noise limit give evidence that magnetic field noise near superconductors is reduced compared with normal metals. A comparison measurement near copper is shown by the gray data points.

The characteristic decay of the atom number in the superconducting microtrap as a function of the hold time is plotted in figure 3(a). We employ the fit function

$$N(t_{\mathrm{hold}}) = (N_0\ \exp(-\Gamma_1 t_{\mathrm{hold}}) + N_1)\ \exp(-\Gamma_2 t_{\mathrm{hold}}), \tag{1}$$

which resembles the experimental situation. $N_0 + N_1$ is the initial atom number, with N_1 being the asymptotic atom number after surface evaporation. For hold times longer than $1/\Gamma_1$, the atom number decays exponentially with a rate Γ_2, which contains all experimentally relevant loss mechanisms, such as vacuum background collisions and spin decoherence.

Figure 4 summarizes the key results of this paper. We plot the measured loss rates Γ_2 near the superconducting niobium wire (blue circles) in order to compare them with the expected spin decoherence rate due to Johnson noise near a normal conducting metal (copper) at the same temperature. The Johnson noise-induced spin decoherence rate for copper is calculated from equation (4) in [10] by

$$\Gamma_2 = \left(\frac{3}{8}\right)^2 \frac{\bar{n}_{\mathrm{th}} + 1}{\tau_0} \left(\frac{c}{\omega_{\mathrm{L}}}\right)^3 \frac{3\delta_{\mathrm{L}}}{d^4}, \tag{2}$$

where $\delta_{\mathrm{L}} = \sqrt{2/\omega_{\mathrm{L}}\mu_0\sigma(T)}$ is the skin depth, $\sigma(T)$ is the electric conductivity of the metal, $\bar{n}_{\mathrm{th}} \approx k_{\mathrm{B}}T/\hbar\omega_{\mathrm{L}}$ is the average occupation of thermal photons, $\tau_0 = 4 \times 10^{23}$ s is the free space

lifetime and d is the separation from the surface. This equation is valid provided that the skin depth is less than the atom–surface separation and also less than the metal thickness. The red dash-dotted line in figure 4 is the calculated spin decoherence rate near copper at 4.2 K ($\delta_L \approx 5\,\mu$m), accounting for the lifetime limiting $|F = 2, m_F = 2\rangle$ to $|F = 2, m_F = 1\rangle$ transition, including an offset of $6.25 \times 10^{-3}\,s^{-1}$ that is the measured vacuum background loss rate.

The measured loss rates for atom–surface separations between 20 and 40 μm give clear evidence that the loss of atoms from the magnetic trap, and thus the spin decoherence rate near the superconductor, is below the Johnson noise limit of a normal metal. Magnetic field fluctuations near superconducting niobium are therefore strongly suppressed.

The diagram also shows the control measurement we made near a normal conducting copper surface at 4.2 K (gray dots). The data confirm that the lifetime of the atom cloud is above the Johnson noise limit and agree with data reported elsewhere [8]. We conclude that near the copper (for the geometry of the measurement see figure 2), Johnson noise and additional surface evaporation due to the limited trap depth are responsible for the observed loss rate. Cooling due to surface evaporation is observed within $\approx 35\,\mu$m of the surface.

For separations smaller than 20 μm between the atom cloud and the niobium wire, the Meissner effect reduces the magnetic trap depth [14] and surface evaporation becomes the dominant loss mechanism. Nonetheless, this limitation of the actual microtrap configuration, which is caused by the exclusion of the magnetic flux from the niobium wire, can be overcome by using superconducting thin films [16] or superconducting microstructures with antidots [17]. These allow the penetration of magnetic flux and promise to support strong magnetic confinement for atom clouds with exceptional spin coherence times even at micron distances from the superconducting surface.

4. Conclusion

Our measurements demonstrate that magnetic field fluctuations near a superconductor are suppressed below the Johnson noise limit of normal conductors. The loss rate we measured at 30 μm distance to the superconducting niobium wire is $6.25 \times 10^{-3}\,s^{-1}$, the smallest loss rate yet measured in the vicinity of highly conductive surface. These results are a step toward the coherent coupling of cold atoms with solid state systems, and toward integrated precision force sensors, whereby cold atoms represent a quantum system of exceptionally long coherence time.

Acknowledgments

This work was supported by the DFG (SFB TRR 21), the UK EPSRC and the BMBF (NanoFutur 03X5506).

References

[1] Rabl P, DeMille D, Doyle J M, Lukin M D, Schoelkopf R J and Zoller P 2006 Hybrid quantum processors: molecular ensembles as quantum memory for solid state circuits *Phys. Rev. Lett.* **97** 033003

[2] Petrosyan D and Fleischhauer M 2008 Quantum information processing with single photons and atomic ensembles in microwave coplanar waveguide resonators *Phys. Rev. Lett.* **100** 170501

[3] Petrosyan D, Bensky G, Kurizki G, Mazets I, Majer J and Schmiedmayer J 2009 Reversible state transfer between superconducting qubits and atomic ensembles *Phys. Rev.* A **79** 040304
[4] Wallraff A, Schuster D I, Blais A, Frunzio L, Huang R-S, Majer J, Kumar S, Girvin S M and Schoelkopf R J 2004 Strong coupling of a single photon to a superconducting qubit using circuit quantum electrodynamics *Nature* **431** 162–7
[5] Jones M P A, Vale C J, Sahagun D, Hall B V and Hinds E A 2003 Spin coupling between cold atoms and the thermal fluctuations of a metal surface *Phys. Rev. Lett.* **91** 080401
[6] Harber D M, McGuirk J M, Obrecht J M and Cornell E A 2003 Thermally induced losses in ultra-cold atoms magnetically trapped near room-temperature surfaces *J. Low Temp. Phys.* **133** 229–38
[7] Lin Y, Teper I, Chin C and Vuletić V 2004 Impact of the Casimir–Polder potential and Johnson noise on Bose–Einstein condensate stability near surfaces *Phys. Rev. Lett.* **92** 050404
[8] Emmert A, Lupascu A, Nogues G, Brune M, Raimond J-M and Haroche S 2009 Measurement of the trapping lifetime close to a cold metallic surface on a cryogenic atom-chip *Eur. Phys. J.* D **51** 173–7
[9] Henkel C, Pötting S and Wilkens M 1999 Loss and heating of particles in small and noisy traps *Appl. Phys.* B **69** 379–87
[10] Scheel S, Rekdal P K, Knight P L and Hinds E A 2005 Atomic spin decoherence near conducting and superconducting films *Phys. Rev.* A **72** 042901
[11] Labaziewicz J, Ge Y, Antohi P, Leibrandt D, Brown K R and Chuang I L 2008 Suppression of heating rates in cryogenic surface-electrode ion traps *Phys. Rev. Lett.* **100** 013001
[12] Hohenester U, Eiguren A, Scheel S and Hinds E A 2004 Spin-flip lifetimes in superconducting atom chips: Bardeen–Cooper–Schrieffer versus Eliashberg theory *Phys. Rev.* A **76** 033618
[13] Silber C, Günther S, Marzok C, Deh B, Courteille Ph W and Zimmermann C 2005 Quantum-degenerate mixture of fermionic lithium and bosonic rubidium gases *Phys. Rev. Lett.* **95** 170408
[14] Cano D, Kasch B, Hattermann H, Kleiner R, Zimmermann C, Koelle D and Fortágh J 2008 Meissner effect in superconducting microtraps *Phys. Rev. Lett.* **101** 183006
[15] Fortágh J and Zimmermann C 2007 Magnetic microtraps for ultracold atoms *Rev. Mod. Phys.* **79** 235–55
[16] Cano D, Kasch B, Hattermann H, Koelle D, Kleiner R, Zimmermann C and Fortágh J 2008 Impact of the Meissner effect on magnetic microtraps for neutral atoms near superconducting thin films *Phys. Rev.* A **77** 063408
[17] Kemmler M, Gürlich C, Sterck A, Pöhler H, Neuhaus M, Siegel M, Kleiner R and Koelle D 2006 Commensurability effects in superconducting Nb films with quasiperiodic pinning arrays *Phys. Rev. Lett.* **97** 147003

Publication 4

S. Bernon, H. Hattermann, D. Bothner, M. Knufinke, P. Weiss, F. Jessen, D. Cano, M. Kemmler, R. Kleiner, D. Koelle and J. Fortágh,
Manipulation and coherence of ultra-cold atoms on a superconducting atom chip,
Nat. Commun. **4**, 2380 (2013).

nature COMMUNICATIONS

ARTICLE

Received 25 Mar 2013 | Accepted 31 Jul 2013 | Published 29 Aug 2013

DOI: 10.1038/ncomms3380

Manipulation and coherence of ultra-cold atoms on a superconducting atom chip

Simon Bernon[1,*,†], Helge Hattermann[1,*], Daniel Bothner[1], Martin Knufinke[1], Patrizia Weiss[1], Florian Jessen[1], Daniel Cano[1], Matthias Kemmler[1], Reinhold Kleiner[1], Dieter Koelle[1] & József Fortágh[1]

The coherence of quantum systems is crucial to quantum information processing. Although superconducting qubits can process quantum information at microelectronics rates, it remains a challenge to preserve the coherence and therefore the quantum character of the information in these systems. An alternative is to share the tasks between different quantum platforms, for example, cold atoms storing the quantum information processed by superconducting circuits. Here we characterize the coherence of superposition states of ^{87}Rb atoms magnetically trapped on a superconducting atom chip. We load atoms into a persistent-current trap engineered next to a coplanar microwave resonator structure, and observe that the coherence of hyperfine ground states is preserved for several seconds. We show that large ensembles of a million of thermal atoms below 350 nK temperature and pure Bose–Einstein condensates with 3.5×10^5 atoms can be prepared and manipulated at the superconducting interface. This opens the path towards the rich dynamics of strong collective coupling regimes.

[1] CQ Center for Collective Quantum Phenomena and their Applications in LISA$^+$, Physikalisches Institut, Eberhard-Karls-Universität Tübingen, Auf der Morgenstelle 14, D-72076, Tübingen, Germany. * These authors contributed equally to this work. † Present address: Quantronics Group, SPEC (CNRS URA 2464), IRAMIS, DSM, CEA-Saclay, 91191 Gif-sur-Yvette, France. Correspondence and requests for materials should be addressed to J.F. (email: fortagh@uni-tuebingen.de).

The quantum physics of interfaces is attracting great interest because quantum state transfer between subsystems is required for quantum measurements, quantum information processing and quantum communication[1]. To overcome the fast decoherence of superconducting qubits, the engineering of various hybrid quantum systems recently became a subject of intensive research[2–8]. The success of strong coupling between superconducting two-level systems and microwave cavities[9], the implementation of quantum algorithms with superconducting circuits[10–12] and the successful realization of superconducting surface traps for ultra-cold atoms[13–15] encourage the development of superconductor/cold atom hybrids. So far, some fundamental interactions between the two systems have been observed[15–17]. However, coherent coupling between the systems remains a scientific and technological challenge. Although theoretical proposals suggest using atomic ensembles as quantum memories in a hybrid quantum computer[18–20], the trapping of atoms in the vicinity of a superconducting coplanar microwave resonator (CPR) is still required.

Long coherence times and state transfer are central issues for quantum information processing. In cold atomic ensembles, the fine control of inhomogeneous dephasing sources[21,22] allows long storage times of a single collective excitation[23]. A similar control in chip-based trapped atomic clocks[24] allowed to preserve coherent states of rubidium hyperfine levels over tens of seconds[25]. In addition, the energy spectrum of rubidium atoms can be used to convert the quantum information to the near infrared, in the telecom band[22], where long-distance quantum communication can be realized[26]. Hybrid systems of cold atoms and superconductors are therefore very appealing for a solid state, atomic and photonic quantum interface. Nevertheless, the question how to preserve such coherence and optical properties in the complex environment of a hybrid system needs to be solved.

Here, we report on the preparation of coherent atomic samples at a superconducting interface. We load ultra-cold ^{87}Rb atoms into a magnetic trap generated by a superconducting niobium thin film structure. We measure exceptionally long lifetimes of fully spin-polarized states (>4 min). In either of the hyperfine ground states of rubidium, we reach the critical temperature of Bose – Einstein condensation with more than one million atoms. The coherence of the superpositions of these ground states is measured for various positions on the superconducting interface. In a self-centred persistent-current trap engineered in the vicinity of a CPR we observe a coherence time $T_2 \sim 8$ s. This demonstrates that cold atom trap inhomogeneities can be controlled in this complex environment to a metrological level, paving the way towards long-living single excitations.

Results

Experimental apparatus. The experimental apparatus combines a cryostat (Janis ST-400, 2 W cooling power) holding a superconducting atom chip and a cold atom setup integrated in a single ultrahigh vacuum chamber (Fig. 1a). The pressure of the chamber, as measured by an ion gauge, is $\sim 10^{-11}$ mbar. Owing to the strong cryopumping, the pressure close to the chip surface is probably even lower. Such vacuum constitutes an excellent heat isolation between the superconducting chip surface at a temperature of $T = 4.2$ and the room temperature electromagnets that are used for the preparation of cold atomic samples[27]. A copper radiation shield at ~ 20 K protects the chip from the room temperature thermal radiation. A slit of 2 mm height on the shield gives optical access to an optical tweezers that transports atom clouds from the room temperature environment to the superconducting atom chip.

The superconducting chip with Z-shaped wires (red line) and a quarter-wave CPR structure is shown in Fig. 1b,c. The niobium film structures (500 nm thickness) were fabricated on monocrystalline sapphire by magnetron sputtering, optical lithography and reactive ion etching (SF_6). Niobium is, in our experimental conditions, a type II superconductor with a transition temperature of 9.2 K. At 4.2 K, the wires carry mean current densities of up to 4×10^6 A cm^{-2}, corresponding to a current of 1 A for a wire of 50 μm width. Supply wires (normal conducting copper) are connected by ultrasonic soldering to the niobium. The sapphire substrate is similarly soldered to the copper mount of the cryostat. Two superconducting wires of 100 μm diameter pass below the chip and help to maintain the longitudinal confinement of the trap (Fig. 1b).

The preparation of atomic clouds follows the standard techniques of magneto-optical (MOT) and magnetic trapping (see Methods for details) and leads, in the room temperature environment, to a cold cloud of 5×10^6 atoms at $T < 1.5$ μK. After transfer to an optical dipole trap, the cloud is transported into the cryogenic environment to the loading position at ~ 400 μm from the superconducting chip surface. The atoms are then transferred into a harmonic magnetic trap[28] formed by superposing the field generated by the current $I_{\mathrm{Trap}} = 0.8$ A driven through the largest Z-shaped trapping wire with a homogeneous magnetic bias field $B_{\mathrm{bias}} = 4$ G applied along y and a magnetic offset field $B_{\mathrm{off}} = 0.6$ G applied along x. The atoms loaded are then adiabatically compressed in a trap with oscillation frequencies $\{\omega_x, \omega_y, \omega_z\}/2\pi = \{19{,}145{,}128\}$ Hz and subsequently cooled by radio-frequency (RF) forced evaporation to temperatures of ~ 200 nK. By changing the length of the initial MOT phase (1–10 s), the atom number in the superconducting trap (10^4–10^6) and the final state (thermal cloud or Bose – Einstein condensate (BEC)) can be conveniently controlled without affecting the temperature. Owing to the strong cryopumping and the suppression of thermally driven magnetic field fluctuations[17], the lifetimes of the atoms in such a surface trap are predicted to be exceptionally long[29–31]. For a cloud of $N_{\mathrm{at}} = 10^5$ atoms polarized in state $|F = 1, m_F = -1\rangle$ (Fig. 1f) at a density of 10^{13} at cm^{-3} held in the compressed trap with an offset field $B_{\mathrm{off}} = 0.6$ G, we measure a lifetime of more than 4 min. From this result and the lifetime of 10 min obtained in Emmert *et al.*[32], we expect excellent vacuum conditions for sub-kelvin cryostats where both cold atoms and superconducting circuits will behave quantum mechanically.

We form pure BECs with up to 3.5×10^5 atoms in either of the spin states, $|F = 1, m_F = -1\rangle$ or $|F = 2, m_F = 2\rangle$. The lifetime of such a condensate in the $|F = 1, m_F = -1\rangle$ state in a trap with frequencies $\{15, 72, 43\}$ Hz is 30(3) s and is density limited by three-body collisional losses[33]. Such high atom number BECs are of special interest for superradiance experiments, for the realization of an on-chip maser[34] and for quantum information protocols in which an effective strong coupling regime is reached by a collective enhancement[20]. For the latter a BEC is not mandatory. It could be better positioned than a thermal cloud but would suffer from a lower atom number and related weaker collective enhancement.

In the following, we explore the properties of the cold cloud in the vicinity of the superconducting CPR. We first consider the positioning of atoms in the close vicinity of the CPR, where we additionally engineer a persistent-current trap. As a further step, we study the coherence of atomic superposition states in different positions of the CPR mode volume. The resonator used in this report is designed to be 250 MHz off resonance from any hyperfine transitions and should therefore not affect the internal state dynamics of the atoms.

Positioning of atomic clouds into a CPR. In a CPR, the electromagnetic fields are concentrated in the gaps between the ground

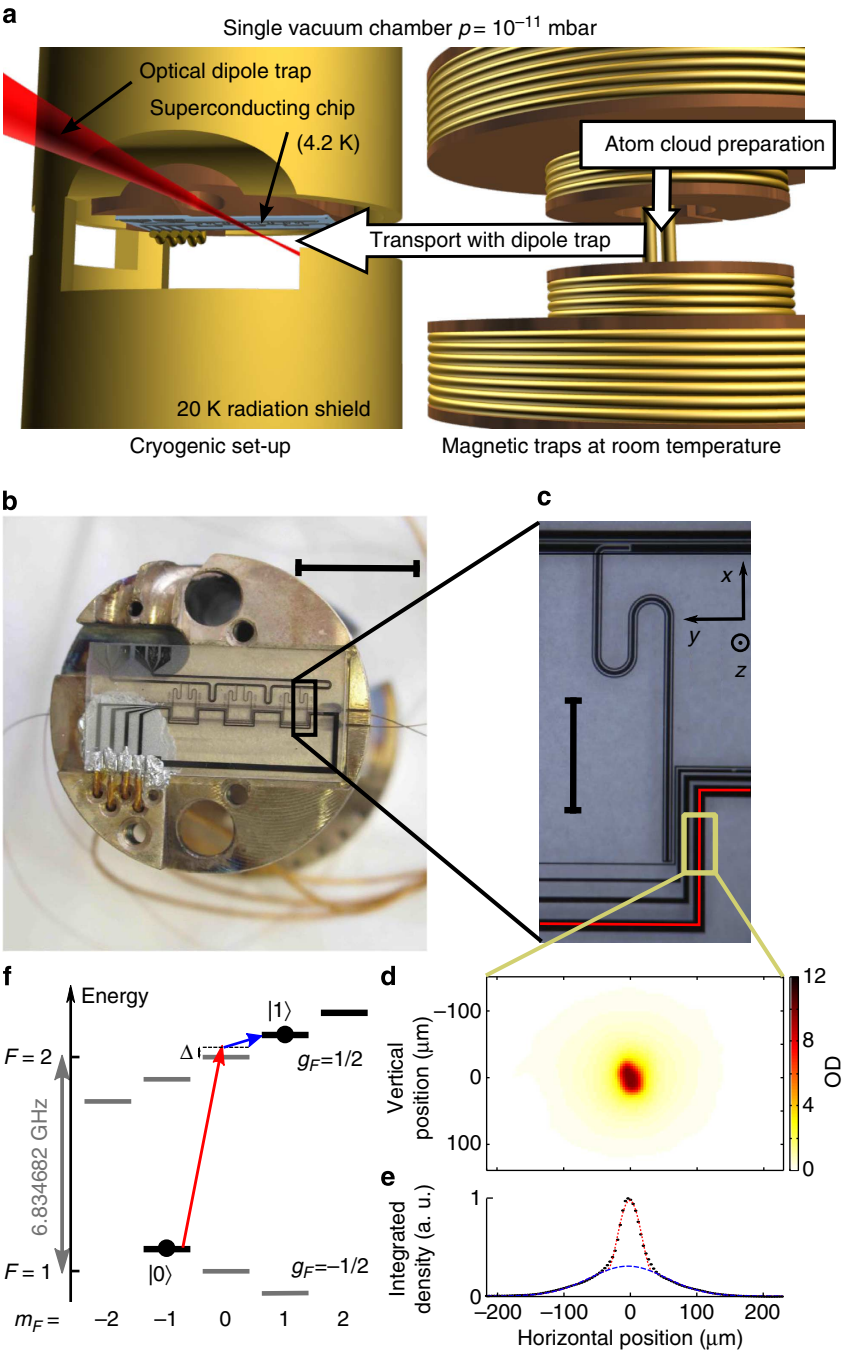

Figure 1 | Hybrid system of ultra-cold atoms and superconductors. (**a**) *In-vacuo* setup (to scale): on the right side, the atoms are trapped and cooled in a room temperature environment. The left part shows the superconducting chip attached to the cryostat at 4.2 K and surrounded by a gold-plated radiation shield at ~20 K. The atoms are transported from one environment to the other (40 mm distance) by optical tweezers. (**b**) Photograph of the superconducting atom chip mounted onto an oxygen-free copper holder. Scale bar, 1 cm. (**c**) Microscope image of the superconducting trapping structure. Visible are four *Z*-wires for trapping, one being highlighted by the red line and a quarter-wave CPR capacitively coupled to the feedline. Scale bar, 1 mm. (**d**) Absorption image of a BEC in state $|0\rangle$ with $N_{BEC} = 3 \times 10^5$ atoms after 15 ms TOF. Colour scale corresponds to optical density (OD). (**e**) Normalized integrated density showing the bi-modal structure of a BEC (black points). In dashed blue is shown a fit to the thermal background and in dotted red a fit to the central Thomas Fermi profile. (**f**) Energy diagram of ^{87}Rb in a magnetic field. In dark are shown the three magnetically trappable states. The coupling of $|F=1, m_F=-1\rangle$ ($|0\rangle$) and $|F=2, m_F=1\rangle$ ($|1\rangle$) is realized by a two-photon transition.

planes and the central conductor. To maximize the atom–cavity coupling, atoms need to be positioned in the close vicinity of these gaps. Nevertheless, for trap-wire distances smaller than the wire width, the trapping parameters are significantly affected by the Meissner–Ochsenfeld effect (MOE)[16,35]. To limit such deformations in the vicinity of the CPR, the design shown in Fig. 1c includes four *Z*-shaped wires with widths ranging from 100 to 15 μm. Starting from the largest *Z*-wire trap, the atoms are first horizontally transferred to the third *Z*-wire trap. The fourth and last wire (15 μm width) revealed to be unnecessary. At 100 μm below the third trapping wire, the trap needs to be rotated towards the CPR gap. Two parameters are classically used to

manipulate the atoms on a chip; the value of the trapping wire current modifies the trap-wire distance and the direction of the bias field rotates the trap around the trapping wire. Because of the MOE, positioning that is straightforward for a normal conducting chip is more subtle for a superconducting atom chip. In the present case, we take advantage of the conservation of magnetic flux in superconducting loops to directly guide the atoms below the gap of the CPR.

The design of the quarter-wave CPR includes a superconducting loop formed by the ground planes of the resonator (blue in Fig. 2). When a field perpendicular to the substrate is applied, such as the bias field, a screening current is induced in the ground planes and ensures the conservation of the magnetic flux in this superconducting loop. Such a current, that circulates just next to the gap, generates a magnetic field profile that guides the atoms into the gap. At distances comparable to the width of the ground planes, such guiding is further enhanced by the MOE that focuses magnetic field lines and generates magnetic gradients that centre the cloud in the gap. The guiding of atoms into the gap is observed by *in situ* measurements of the position of the atomic cloud for different bias field orientations (angle α in Fig. 3a) and different currents in the wire (Fig. 3a). For each experimental point, the cloud is first brought to a trap-wire distance of $\sim$100 µm, rotated to the angle α and then moved to the desired trapping current. The measured position (y, z) agrees well with a 2D simulation of the London equations[36] that includes gravity and the conservation of flux in the resonator loop (see Methods). The simulations are performed without free parameters. As experimentally observed and consistent with our model, we note that the two gaps of the CPR are not equivalent. Owing to the opposite direction of the current in the ground planes and the orientation of the bias field, only the closest gap to the trapping wire can be accessed. We call this trap, resulting from applied and induced currents, a hybrid trap.

A further advantage in using superconductors to manipulate cold atoms is the possibility to engineer traps induced by persistent currents. These persistent-current traps[14] render the direct injection of currents on the chip unnecessary and therefore suppress the related source of noise. In our geometry, such a trap can be generated directly below the CPR. Here we demonstrate a self-centred trap generated by a single homogeneous bias field and its induced screening currents. By trapping flux in the resonator loop with a freezing field applied during the cooling of the cryostat, the magnitude of the screening currents can be controlled independently from the applied bias field. This experimentally realized trap is simulated in Fig. 3b, where both the resulting potential and the current densities are depicted. The simulation presented includes the distortion due to the MOE, the conservation of magnetic flux in the loop and the effect of vortices trapped inside the film during the cooling of the cryostat[37,38]. The agreement of position and trap frequencies between the experiment and our simple model requires an adjustment of the input parameters by $<20\%$. In the trap of Fig. 3b with oscillation frequencies $\{35, 173, 107\}$ Hz, a cloud at $T\sim90$ nK starting with $>30\%$ condensed fraction and a central density $<8\times10^{13}$ at cm^{-3} has a lifetime of 10(4) s, probably limited by the shallow trap depth ($\sim$320 nK). We stress that, in this loop geometry, the conservation of magnetic flux should reduce the amplitude of external magnetic noise at the trap position.

Coherence in a superconducting CPR. To study the coherence lifetime of atomic ensembles in the close vicinity of a CPR, we perform Ramsey measurements at different positions below the superconducting chip. These measurements compare the coherence of a trapped atomic ensemble in a superposition of the states $|0\rangle = |F=1,\ m_F=-1\rangle$ and $|1\rangle = |F=2,\ m_F=1\rangle$ (Fig. 1f) with a high-stability 10 MHz reference oscillator that has a short-

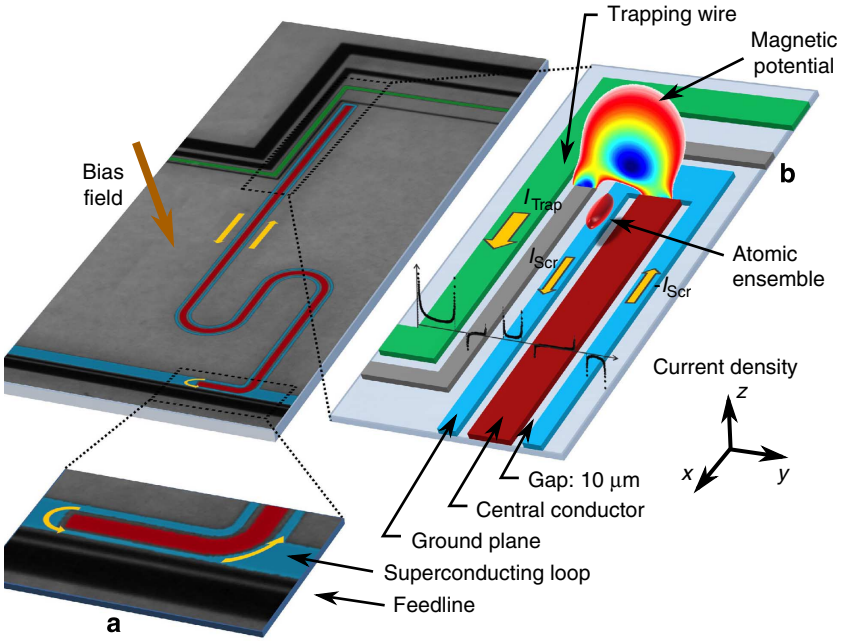

Figure 2 | Atom-trapping scheme. Scheme of the atoms trapped in the gap of a superconducting quarter wavelength coplanar microwave resonator (CPR). (**a**) Zoom of the superconducting link between the two ground planes of the CPR. (**b**) Zoom of the structure around the trapping region. The trap inside the gap is a result of the magnetic fields generated by the current of the trapping wire I_{Trap} and by the screening current I_{Scr} in the ground plane. These fields cancel with an externally applied bias field. The embedded plot (black dots) is the simulated distribution of the screening currents in the superconductor. These currents keep the flux in the superconducting loop constant and the interior of the films field free. The transverse profile of the magnetic potential is shown in colour. The dark blue corresponds to the potential minimum.

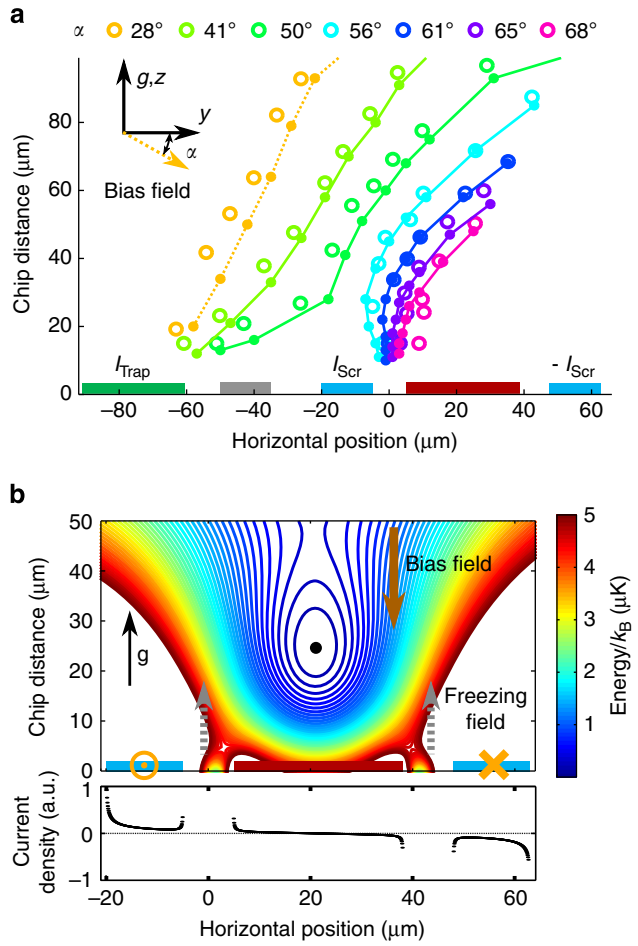

Figure 3 | Positioning atoms close to a superconducting coplanar microwave resonator. (**a**) Position of the trap for different currents in the trapping wire and different angles α between the bias field and the surface of the chip. $\alpha = \arctan(B_z^{bias}/B_y^{bias})$ is varied by changing B_z^{bias} with $B_y^{bias} = 2.3$ G constant. The position of the atoms has been measured by *in situ* absorption imaging (Methods). For small angles, the trap behaves as for a normal conducting chip, that is, when the current is reduced in the trapping wire (I_{Trap}), the trap moves towards it. For large angles, this behaviour is modified and the trap is focused into the gap between the centre conductor and the ground plane of the CPR. The agreement between measurement (circles) and simulations (dotted and solid lines with dots) proves that positioning of the atoms in the gap of the CPR can be facilitated by screening currents I_{Scr} in the ground planes. The simulations[36] are performed with no adjustable parameter and assume a Meissner state for the superconductor. Gravity, g, is oriented upwards. (**b**) Top: potential energy landscape of a persistent-current trap above the central conductor (red) of the CPR. This trap is generated by the superposition of a vertical homogeneous bias field $B_z^{bias} \approx 1.2$ G and the field induced by the screening currents. To enhance the screening currents at a given bias field, a non-zero flux is trapped in the gap of the CPR during the cool-down of the cryostat (freezing field, $B_z^{freezing} \approx 0.5$ G). Isolines are separated by 100 nK. Bottom: screening current density distribution induced by the combination of bias field and freezing field.

and long-term frequency stability $\Delta f/f < 5 \times 10^{-12}$. These two states are chosen for the low sensitivity of their transition frequency to magnetic inhomogeneities at a magnetic offset field of 3.228 G (see Methods)[39]. The atomic cloud is first prepared in a thermal and pure state of $|0\rangle$. The initialization of the coherent superposition is realized by a $\pi/2$ two-photon excitation that starts the interferometric sequence. After a variable waiting time T_R, the interferometer is closed by a second $\pi/2$ pulse. The populations $N_0(T_R)$ and $N_1(T_R)$ in, respectively, $|F=1\rangle$ and $|F=2\rangle$ are consecutively read out by state-selective absorption imaging (see Methods), and the resulting probability of $|F=2\rangle$: $N_1(T_R)/(N_0(T_R)+N_1(T_R))$ is displayed in Fig. 4a–c.

To study the capabilities of our setup, we first describe a reference measurement that is performed far from the CPR: 60 μm below the third trapping wire (green star: Fig. 4a). This measurement is conducted with $1.9(4) \times 10^4$ atoms at a temperature of 245(30) nK in a magnetic trap with oscillation frequencies {10, 215, 181} Hz, corresponding to a mean density (in units of 10^{12} at/cm^3) $\bar{n} \approx 0.4(1)$. In this configuration, the coherence time, as measured by the decay of the envelope, is $T_{coh} = 20.5(6.0)$ s ($1/e$ exponential decay time). Owing to magnetic noise in this non-shielded apparatus and drifts over the length of the scan (several hours), the phase starts to be lost for $T_R > 5$ s, corresponding to a technically induced reduction of the T_2 time of the ensemble. The observed decay time T_{coh} exceeds the time of 6 s predicted by the residual trap inhomogeneities $\Delta_0/2\pi \approx 0.04$ Hz (see Methods[40]). This indicates that we entered the spin self-rephasing (SSR) regime[25], where the identical spin rotation rate $\omega_{ex}/2\pi = 3$ Hz dominates both Δ_0 and the rate of lateral elastic collisions $\gamma_c = 1\,s^{-1}$. This regime can be understood as a continuous spin-echo process triggered by forward atomic collisions.

The second trap under study is the hybrid trap, situated 14 μm below the gap of the CPR. As mentioned before, this position is particularly privileged for the perspective of strong atom–cavity coupling. The Ramsey fringes shown by blue squares (Fig. 4b) were obtained for $1.25(40) \times 10^4$ atoms at a temperature of 320(20) nK held in a confined trap {16.9, 451, 390} Hz, corresponding to $\bar{n} \approx 1.24(40)$. The coherence time is $T_2 \approx T_{coh} = 3.9(5)$ s. The reduction with respect to the reference position is mainly explained based on the atom loss decay time of 3.4(2) s of the hybrid trap. This loss rate is asymmetric and mainly affects the state $|1\rangle$. It is partially explained by spin-exchanging collisions that transfer two collisioning atoms in $|1\rangle$ towards the states $|F=2, m_F=0\rangle$ (untrapped) and $|F=2, m_F=2\rangle$ (trapped). In Fig. 4b, this collision process is responsible for the asymmetry of the probability for large T_R. It comes as a drawback of the guiding mechanism that strongly compresses the trap and increases the atomic density (see Table 1). The spin-exchanging collision rate $\gamma_{22} = 1.6 \times 10^{-13}\,cm^3\,s^{-1}$ reported in Egorov *et al.*[41] is insufficient to fully explain our observed loss rate and other possible mechanisms are under study. The fringes presented in Fig. 4b result from an optimization of the temperature that is high enough to minimize collisional losses and low enough to enter the SSR regime ($\omega_{ex}/2\pi = 9.5$ Hz, $\gamma_c = 3.6\,s^{-1}$, $\Delta_0/2\pi = 0.12$ Hz).

The last position studied corresponds to the persistent-current trap previously mentioned (red disk: Fig. 4c). In this trap the measurement was performed with $1.25(40) \times 10^4$ atoms at 158(23) nK, corresponding to $\bar{n} \approx 0.78(30)$ and to the related SSR parameters $\omega_{ex}/2\pi = 6$ Hz, $\gamma_c = 1.6\,s^{-1}$ and $\Delta_0/2\pi = 0.1$ Hz. The coherence lifetime obtained is $T_2 \approx T_{coh} = 7.8(14)$ s and is mainly limited, in this shallow trap ($\sim$320 nK), by the atom loss decay time 4.8(3) s.

Discussion

The three measurements are compared in Table 1. It shows that the trap deformation induced by the superconducting CPR results in an increase in the trap frequencies, which impact the coherence of the atomic cloud. We do not expect that such coherence would change for a cavity on-resonance with the transition from $|0\rangle$ to

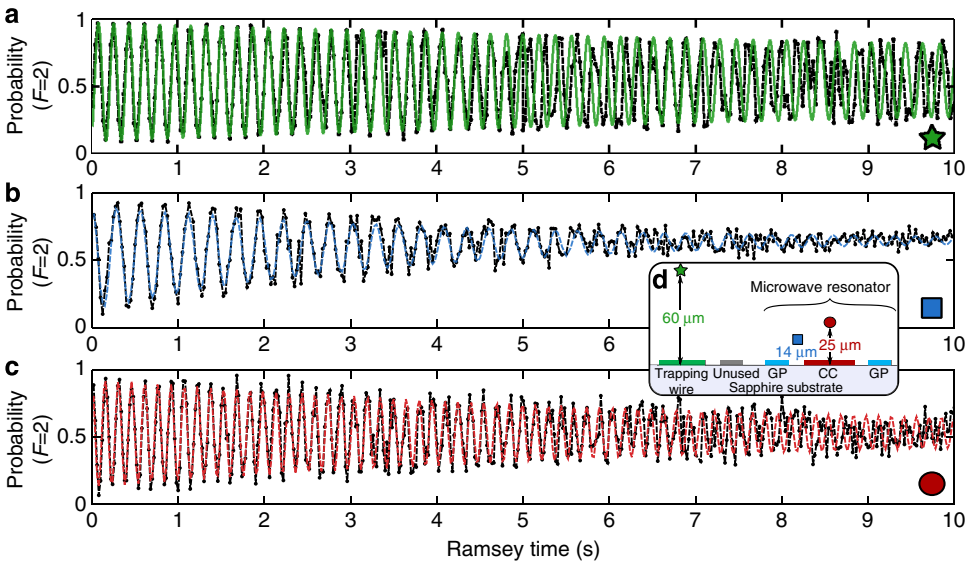

Figure 4 | Atomic coherence in a superconducting coplanar microwave resonator. Ramsey fringes measured in the time domain for different trapping positions on the superconducting atom chip. From top to bottom, the trapping positions correspond to: (**a**) the reference trap (green star in (**d**)), (**b**) the hybrid trap (blue square in (**d**)) and (**c**) the persistent-current trap (red disk in (**d**)). The coherence time obtained for the three sets are 20.5, 3.9 and 7.8 s, respectively, that indicate collision-induced SSR effects[25] (see main text and Methods). The coherence time of each set is estimated by measuring the fringe contrast decay on time intervals in which the phase is preserved. Black dots are experimental data and coloured lines are fits, with a fixed decay, to the first few seconds of the oscillation: 5, 3 and 4 s, respectively. Inset (**d**): positions of the different traps. The reference trap is situated 60 µm straight below the trapping wire. The hybrid trap, which is generated by applied and induced currents, stands 14 µm below the 10-µm-wide gap of the CPR. The persistent-current trap is 25 µm below the central conductor (CC) of the CPR that has a width of 33 µm. GP stands for ground planes. Horizontal and vertical axes are to scale. The experimental parameters for each measurement are summarized in Tables 1 and 2.

Table 1 | Results of atomic coherence.

	Reference	Hybrid	Persistent
Symbols	Green star	Blue square	Red disk
Trap frequencies (Hz)	10.3 (2)	16.9 (2)	35 (2)
	215 (5)	451 (5)	173.4 (6)
	181 (2)	390 (8)	107 (3)
Mean frequency (Hz)	73.7 (6)	144 (3)	87 (3)
Atomic density ($\times 10^{12}$ at. cm^{-3})	0.4 (1)	1.24 (40)	0.78 (30)
Coherence time (s)	20.5 (6.0)	3.9 (5)	7.8 (1.4)
Expected τ_{inh} without SSR (s)	6.5	1.8	2.1

Experimental parameters for the three measurements shown in Fig. 4. The density quoted is the mean atomic density. The mean frequency is the geometrical average. $\tau_{inh} = \sqrt{2}/\Delta_0$ is the coherence time expected without SSR for the corresponding residual frequency inhomogeneity Δ_0 (see Methods).

$|1\rangle$ that necessarily involves two photons. Nevertheless, thermal photons in a cavity that would be on resonance with one of the transitions from $|0\rangle$ or $|1\rangle$ to untrapped states could open an asymmetric loss channel and a corresponding loss of coherence. In the effective strong coupling limit that we target, this process could be used to cool the mode of the resonator[20].

In conclusion, we have demonstrated that, in the vicinity of a superconducting CPR, magnetic traps can be engineered to produce robust and controllable conditions for the coherent manipulation of atoms. The preparation of large BECs and thermal clouds of a million atoms opens the path to the strong collective coupling to a CPR, and to the transfer of quantum information between atomic and superconducting systems. The long coherence of atomic superposition states on the time scale of seconds encourages the development of cold atom/superconductor hybrid quantum systems in which cold atoms would serve as quantum memory. Although the motion of particles is usually considered as a source of decoherence, which, for example, prevents the use of spin-echo techniques, it has an important role in this experiment to maintain the coherence of the superposition state. If such a mechanism can be extended to preserve the coherence of single excitations, it will surely lead to very rich dynamics of collective states.

Methods

Atom cloud preparation. The magneto-optical trap (MOT) is loaded from a 2D-MOT. For a loading time of 6 s, the MOT contains $\sim 10^9$ ^{87}Rb atoms at a temperature of ~ 200 µK. With this method, we do not observe perturbation of the background pressure. After an optical molasses, the atomic cloud is optically pumped into one of the two hyperfine ground states $|0\rangle$ or $|F=2, m_F=2\rangle$ (total angular momentum states) and is transferred through a magnetic quadrupole into a harmonic Ioffe – Pritchard-type trap. It is further cooled by forced RF evaporation to a temperature of ~ 1.5 µK, slightly above the BEC transition. The remaining 5×10^6 atoms are loaded into optical tweezers ($\lambda = 1064$ nm laser, $P = 500$ mW, focused to $w_0 = 25$ µm beam waist) and transported without significant loss or heating over a distance of 40 mm to the superconducting chip. During the optical transfer, a quantization field of 350 mG along x is applied to maintain the polarization of the sample.

Magnetic field calibration. At the position of the atomic cloud, below the superconducting chip, the magnetic field is controlled by three orthogonal pairs of coils that allow to independently control the three directions of space. The calibration of the residual field and the field generated by the coils is realized *in situ* by microwave spectroscopy. To that purpose, the atoms are prepared in $|0\rangle$ and the magnetic field is set to the desired field of study. After all Eddy currents have damped out, the atoms are released from the optical dipole trap. The microwave transition considered is $|0\rangle$ to $|F=2, m_F=0\rangle$. In the absence of a magnetic field it has a frequency of 6.834682610 GHz and a first-order Zeeman sensitivity of 700 kHz G^{-1}. In a first coarse step, the absolute field is reduced to below 5 mG. In a second fine step, each pair of coils is switched on in a row to generate a frequency shift of approximately 200 kHz. This shift is then measured with an accuracy of $\pm$ 500 Hz. This way, each pair of coils is *in situ* and independently calibrated (residual contribution from other pairs below 1%) and the residual field is measured to below 1 mG, while the coils are calibrated with an accuracy better than 0.3%.

Table 2 | Experimental parameters for atomic coherence measurements.

Properties	Reference	Hybrid	Persistent
P_{MW} (dBm)	19	−10	−14
P_{RF} (dBm)	−2	11.5	11.5
$\Delta_R/2\pi$ (Hz)	5.7	3.5	6.5
$\Omega_R/2\pi$ (Hz)	432	416	179
B_1 (G)	3.193 (4)	3.203 (20)	3.20 (3)
B_1^{opt} (G)	3.197	3.17	3.17
$\Delta_O/2\pi$ (Hz)	0.04	0.12	0.1
τ_{inh} (s)	6.5	1.8	2.1

The parameters presented relate to the measurement shown in Fig. 4.

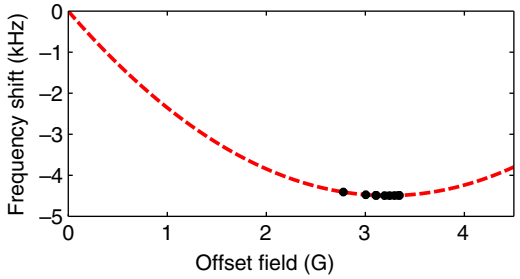

Figure 5 | Differential frequency shift of the $|0\rangle$ to $|1\rangle$ transition. The black points are experimental data. The red dashed line is the prediction given by the Breit-Rabi formula[45].

To avoid perturbation by the MOE of the nearby superconductor, this calibration is done with the cryostat at $T \approx 10$ K.

Imaging and measurement of position. The atoms are observed by absorption imaging with a variable time of flight (TOF). The large BEC in Fig. 1d was measured by off-resonance imaging, which was calibrated on a low-density cloud. Owing to eddy currents in the mechanical system, the measured atom number is not absolute and depends on the TOF. For TOF < 10 ms, the calibration of the detection of the state $|0\rangle$ with respect to the state $|1\rangle$ is obtained by minimizing the variance of the total atom number detected over the length of the scan. For TOF > 10 ms, atom numbers stay constant, showing that eddy currents are no more an issue at the corresponding distances. The absolute calibration of the atom number is obtained from the critical temperature of Bose − Einstein condensation. This calibration is the main source of uncertainty of the atom numbers (20%). Therefore, the atom number uncertainty quoted in the text does not represent shot-to-shot fluctuations.

The state-selective measurement realized for the coherence measurement is done by first measuring and blasting the atoms in $F = 2$, and second by repumping and measuring the atoms in $F = 1$. The two measurements are realized on orthogonal axes.

In situ, the position of the atomic cloud is measured along the three directions of space by two reflection imaging systems that are aligned along x and y. The calibration of distances is realized by TOF of the magnetically insensitive state $|F = 2, m_F = 0\rangle$. To avoid spurious effects, the chip is uncoated.

Magnetic field calculations. To calculate the current densities in the superconductor and the subsequent atomic trap deformation, we solved the London equations using the 2D algorithm described in Cano *et al.*[36] This treatment is particularly valid in the trapping region where thin films are parallel to each other. The assumption of a pure Meissner state can be justified by an estimate of the maximum fields at the lead edges[42]. In our field and current range, these edge fields remain considerably below the lower critical field of a dirty niobium film[43], assuming a penetration depth $\lambda_L \approx 100$ nm and a Ginzburg − Landau parameter $\kappa \approx 10$. The conservation of flux in the superconducting loop of the resonator is further taken into account by imposing net currents in the grounds of the resonator. The influence of an homogeneous density of vortices pointing along z is modelled by the superposition of an homogeneous field along z (undeformed) and the opposite field deformed by the superconducting structure in a pure Meissner state. In all simulations, the quantization of flux is neglected ($\Phi_0/\Phi \approx 5 \times 10^{-5}$). The simulations presented in Figs 2 and 3 have been confirmed using a 3D simulator (3D-MLSI[44]). The effect of gravity is included in all simulations.

Details on the measurement of coherence lifetime. The measurement of the T_{coh} time of the atomic qubit formed by the state $|0\rangle$ and $|1\rangle$ is realized by a Ramsey-type experiment. As shown in Fig. 1f, the two states are coupled via a two-photon transition involving a microwave photon at $f_{MW} = 6.83337816$ GHz and an RF photon at $f_{RF} = 1.3$ MHz. Both frequencies are generated by commercial synthesizer phase locked to a high-stability 10 MHz quartz oscillator (Oscillo-quartz, 8607-BHM15), and their sum is frequency detuned from the atomic transition by $\Delta_R/2\pi$. For all the measurement presented, the microwave with power P_{MW} is radiated by an helicoidal antenna situated outside the vacuum chamber at a distance of 20 cm from the atoms. The RF with power P_{RF} is coupled on the chip to the largest Z-wire. The Rabi frequency Ω_R obtained in each situation is summarized in Table 2. Figure 5 shows the differential frequency shift of the qubit transition that is well approximated by $\Delta\nu(\mathbf{r}) = \nu_{|1\rangle} - \nu_{|0\rangle} = \Delta\nu_0 + \beta(B(\mathbf{r}) - B_0)^2$, with $\Delta\nu_0 = 4.4973$ kHz, $B_0 = 3.228917(3)$ G (ref. 25) and $\beta = 431.36$ Hz/G^2 (ref. 39). At the magic offset field B_0, this shift is first-order insensitive to the magnetic field. The sensitivity of the coherence time to the magnetic inhomogeneities of the trap is therefore highly reduced. The measurements presented in Fig. 4 are performed with an offset field B_{off} slightly lower than B_0. This configuration is known as the mutual compensation scheme[39,40], which allows to compensate the negative collisional shift $\Delta_c(\mathbf{r})/2\pi = -0.4n(\mathbf{r})/10^{12}$ Hz by the positive magnetic shift $\Delta_B(\mathbf{r}) = 2\pi\Delta\nu(\mathbf{r})$. In such conditions, an optimum residual radial frequency homogeneity $\Delta_0 = \sqrt{\langle(\Delta_c(\mathbf{r}) + \Delta_B(\mathbf{r}))^2\rangle - \langle\Delta_c(\mathbf{r}) + \Delta_B(\mathbf{r})\rangle^2}$ is obtained for an optimal offset field B_1^{opt} that depends on the number of particles, the temperature and the geometry of the trap. In Table 2, we give the optimum value of Δ_0 for each experimental configuration. In the abscence of spin-rephasing, such inhomogeneities should result in a decay of the Ramsey contrast with a time constant $\tau_{inh} = \sqrt{2}/\Delta_0$ (ref. 40).

References

1. Wallquist, M., Hammerer, K., Rabl, P., Lukin, M. & Zoller, P. Hybrid quantum devices and quantum engineering. *Phys. Scr.* **2009,** 014001 (2009).
2. Kubo, Y. *et al.* Hybrid quantum circuit with a superconducting qubit coupled to a spin ensemble. *Phys. Rev. Lett.* **107,** 220501 (2011).
3. Zhu, X. *et al.* Coherent coupling of a superconducting flux qubit to an electron spin ensemble in diamond. *Nature* **478,** 221–224 (2011).
4. Amsüss, R. *et al.* Cavity QED with magnetically coupled collective spin states. *Phys. Rev. Lett.* **107,** 060502 (2011).
5. Camerer, S. *et al.* Realization of an optomechanical interface between ultracold atoms and a membrane. *Phys. Rev. Lett.* **107,** 223001 (2011).
6. O'Connell, A. D. *et al.* Quantum ground state and single-phonon control of a mechanical resonator. *Nature* **464,** 697–703 (2010).
7. Kálmán, O., Kiss, T., Fortágh, J. & Domokos, P. Quantum galvanometer by interfacing a vibrating nanowire and cold atoms. *Nano Lett.* **12,** 435–439 (2012).
8. Xiang, Z.-L., Ashhab, S., You, J. Q. & Nori, F. Hybrid quantum circuits: superconducting circuits interacting with other quantum systems. *Rev. Mod. Phys.* **85,** 623–653 (2013).
9. Wallraff, A. *et al.* Strong coupling of a single photon to a superconducting qubit using circuit quantum electrodynamics. *Nature* **431,** 162–167 (2004).
10. DiCarlo, L. *et al.* Demonstration of two-qubit algorithms with a superconducting quantum processor. *Nature* **460,** 240–244 (2009).
11. Fedorov, A., Steffen, L., Baur, M., Da Silva, M. P. & Wallraff, A. Implementation of a Toffoli gate with superconducting circuits. *Nature* **481,** 170–172 (2012).
12. Reed, M. D. *et al.* Realization of three-qubit quantum error correction with superconducting circuits. *Nature* **482,** 382–385 (2012).
13. Nirrengarten, T. *et al.* Realization of a superconducting atom chip. *Phys. Rev. Lett.* **97,** 200405 (2006).
14. Mukai, T. *et al.* Persistent supercurrent atom chip. *Phys. Rev. Lett.* **98,** 260407 (2007).
15. Müller, T. *et al.* Trapping of ultra-cold atoms with the magnetic field of vortices in a thin-film superconducting micro-structure. *New J. Phys.* **12,** 043016 (2010).
16. Cano, D. *et al.* Meissner effect in superconducting microtraps. *Phys. Rev. Lett.* **101,** 183006 (2008).
17. Kasch, B. *et al.* Cold atoms near superconductors: atomic spin coherence beyond the Johnson noise limit. *New J. Phys.* **12,** 065024 (2010).
18. Petrosyan, D. & Fleischhauer, M. Quantum information processing with single photons and atomic ensembles in microwave coplanar waveguide resonators. *Phys. Rev. Lett.* **100,** 170501 (2008).
19. Petrosyan, D. *et al.* Reversible state transfer between superconducting qubits and atomic ensembles. *Phys. Rev. A* **79,** 040304 (2009).
20. Verdú, J. *et al.* Strong magnetic coupling of an ultracold gas to a superconducting waveguide cavity. *Phys. Rev. Lett.* **103,** 043603 (2009).
21. Dudin, Y. O., Zhao, R., Kennedy, T. A. B. & Kuzmich, A. Light storage in a magnetically dressed optical lattice. *Phys. Rev. A* **81,** 041805 (2010).
22. Radnaev, A. G. *et al.* A quantum memory with telecom-wavelength conversion. *Nature Phys.* **6,** 894–899 (2010).

23. Bao, X. H., Reingruber, A., Dietrich, P. & Rui, J. Efficient and long-lived quantum memory with cold atoms inside a ring cavity. *Nature Phys.* **8,** 517–521 (2012).
24. Treutlein, P., Hommelhoff, P., Steinmetz, T., Hänsch, T. W. & Reichel, J. Coherence in microchip traps. *Phys. Rev. Lett.* **92,** 203005 (2004).
25. Deutsch, C. *et al.* Spin self-rephasing and very long coherence times in a trapped atomic ensemble. *Phys. Rev. Lett.* **105,** 020401 (2010).
26. Ritter, S. *et al.* An elementary quantum network of single atoms in optical cavities. *Nature* **484,** 195–200 (2012).
27. Cano, D. *et al.* Experimental system for research on ultracold atomic gases near superconducting microstructures. *Eur. Phys. J. D* **63,** 17–23 (2011).
28. Fortágh, J. & Zimmermann, C. Magnetic microtraps for ultracold atoms. *Rev. Mod. Phys.* **79,** 235–289 (2007).
29. Skagerstam, B. K., Hohenester, U., Eiguren, A. & Rekdal, P. K. Spin decoherence in superconducting atom chips. *Phys. Rev. Lett.* **97,** 070401 (2006).
30. Hohenester, U., Eiguren, A., Scheel, S. & Hinds, E. A. Spin-flip lifetimes in superconducting atom chips: Bardeen-Cooper-Schrieffer versus Eliashberg theory. *Phys. Rev. A* **76,** 033618 (2007).
31. Nogues, G. *et al.* Effect of vortices on the spin-flip lifetime of atoms in superconducting atom-chips. *Eur. Phys. Lett.* **87,** 13002 (2009).
32. Emmert, A. *et al.* Measurement of the trapping lifetime close to a cold metallic surface on a cryogenic atom-chip. *Eur. Phys. J. D* **51,** 173–177 (2009).
33. Söding, J. *et al.* Three-body decay of a rubidium Bose – Einstein condensate. *Appl. Phys. B* **69,** 257–261 (1999).
34. Henschel, K., Majer, J., Schmiedmayer, J. & Ritsch, H. Cavity QED with an ultracold ensemble on a chip: prospects for strong magnetic coupling at finite temperatures. *Phys. Rev. A* **82,** 033810 (2010).
35. Markowsky, A., Zare, A., Graber, V. & Dahm, T. Optimal thickness of rectangular superconducting microtraps for cold atomic gases. *Phys. Rev. A* **86,** 023412 (2012).
36. Cano, D. *et al.* Impact of the Meissner effect on magnetic microtraps for neutral atoms near superconducting thin films. *Phys. Rev. A* **77,** 063408 (2008).
37. Stan, G., Field, S. B. & Martinis, J. M. Critical field for complete vortex expulsion from narrow superconducting strips. *Phys. Rev. Lett.* **92,** 097003 (2004).
38. Emmert, A. *et al.* Microtraps for neutral atoms using superconducting structures in the critical state. *Phys. Rev. A* **80,** 061604(R) (2009).
39. Harber, D. M., Lewandowski, H. J., McGuirk, J. M. & Cornell, E. A. Effect of cold collisions on spin coherence and resonance shifts in a magnetically trapped ultracold gas. *Phys. Rev. A* **66,** 053616 (2002).
40. Rosenbusch, P. Magnetically trapped atoms for compact atomic clocks. *Appl. Phys. B* **95,** 227–235 (2009).
41. Egorov, M. *et al.* Precision measurements of s-wave scattering lengths in a two-component Bose – Einstein condensate. *Phys. Rev. A* **87,** 053614 (2013).
42. Zeldov, E., Clem, John R., McElfresh, M. & Darwin, M. Magnetization and transport currents in thin superconducting films. *Phys. Rev. B* **49,** 9802–9822 (1994).
43. Brandt., E. H. The flux-line lattice in superconductors. *Rep. Prog. Phys.* **58,** 1465–1594 (1995).
44. Khapaev, M. M., Kupriyanov, M. Y., Goldobin, E. & Siegel, M. Current distribution simulation for superconducting multi-layered structures. *Supercond. Sci. Technol.* **16,** 24–27 (2003).
45. Breit, G. & Rabi, I. I. Measurement of nuclear spin. *Phys. Rev.* **38,** 2082–2083 (1931).

Acknowledgements

We would like to thank Thomas Udem from the MPQ Munich as well as Max Kahmann and Ekkehard Peik from the PTB Braunschweig for the loan of the reference oscillators. This work was supported by the Deutsche Forschungsgemeinschaft (SFB TRR 21) and ERC (Socathes). H.H. and D.B. acknowledge support from the Evangelisches Studienwerk e.V.Villigst. M.Kn. and M.Ke. acknowledge support from the Carl Zeiss Stiftung.

Author contributions

D.K., R.K., J.F., S.B., H.H., F.J., M.Kn. and M.Ke. designed and mounted the experiment. D.B., M.Kn., M.Ke. and H.H. designed and fabricated the superconducting chip. S.B., H.H. and P.W. carried out the experiments and analysed the data. S.B., H.H., D.C., M.Kn. and D.B. made the numerical simulations. D.K., R.K. and J.F. supervised the project. S.B., H.H. and J.F. edited the manuscript. All authors discussed the results and commented on the manuscript.

Additional information

Competing financial interests: The authors declare no competing financial interests.

Reprints and permission information is available online at http://npg.nature.com/reprintsandpermissions/

How to cite this article: Bernon, S. *et al.* Manipulation and coherence of ultra-cold atoms on a superconducting atom chip. *Nat. Commun.* 4:2380 doi: 10.1038/ncomms3380 (2013).

Publication 5

H. Hattermann, M. Mack, F. Karlewski, F. Jessen, D. Cano, and J. Fortágh,
Detrimental adsorbate fields in experiments with cold Rydberg gases near surfaces,
Phys. Rev. A **86**, 022511 (2012).

PHYSICAL REVIEW A **86**, 022511 (2012)

Detrimental adsorbate fields in experiments with cold Rydberg gases near surfaces

H. Hattermann,* M. Mack, F. Karlewski, F. Jessen, D. Cano, and J. Fortágh†
CQ Center for Collective Quantum Phenomena and their Applications, Physikalisches Institut, Eberhard-Karls-Universität Tübingen, Auf der Morgenstelle 14, D-72076 Tübingen, Germany
(Received 4 June 2012; published 17 August 2012)

We observe the shift of Rydberg levels of rubidium close to a copper surface when atomic clouds are repeatedly deposited on it. We measure transition frequencies of rubidium to S and D Rydberg states with principal quantum numbers n between 31 and 48 using the technique of electromagnetically induced transparency. The spectroscopic measurement shows a strong increase of electric fields towards the surface that evolves with the deposition of atoms. Starting with a clean surface, we measure the evolution of electrostatic fields in the range between 30 and 300 μm from the surface. We find that after the deposition of a few hundred atomic clouds, each containing $\sim 10^6$ atoms, the field of adsorbates reaches 1 V/cm for a distance of 30 μm from the surface. This evolution of the electrostatic field sets serious limitations on cavity QED experiments proposed for Rydberg atoms on atom chips.

DOI: 10.1103/PhysRevA.86.022511 PACS number(s): 32.30.−r, 32.80.Rm, 68.43.−h

I. RYDBERG ATOMS AT SURFACES

The large electric polarizability of Rydberg atoms leads to a large response to electric fields [1]. This property is an enormous advantage for applications that require fast coupling between atoms and photons, such as the entanglement of Rydberg atoms via the electromagnetic modes of radio-frequency and microwave cavities [2]. Several quantum computation schemes have been proposed based on Rydberg atoms coupled to superconducting coplanar cavities [3–5]. In the proposed scenarios, cold atomic gases are first positioned near a coplanar resonator. The atoms are subsequently laser excited into Rydberg states which interact with the electromagnetic modes of the resonator. Recent progress with coupling such cavities to superconducting qubits [6,7] and the coupling of Rydberg atoms to a microwave stripline [8] outline good perspectives.

However, the technical realization faces challenges. One significant problem is the detrimental effect of the electrostatic fields generated by adsorbed atoms on the chip surface. Because of the high electronegativity of metals, atoms deposited on the chip surface partially donate their valence electron to the metal. The result is a permanent electric dipole layer on the surface that produces inhomogeneous electrostatic fields and alters both the energy and the orbital structure of nearby Rydberg atoms. The fields can be strong enough to shift Rydberg states out of the cavity resonance.

New chips are initially free of adsorbates, but experiments progressively accumulate adatoms on the surface. An important question is how long it takes until the accumulation of atoms on the surface becomes detrimental. Two research groups reported previously on this subject. First, McGuirk *et al*. [9] and Obrecht *et al*. [10] studied the electrostatic field of adsorbed atoms on both conducting and insulating surfaces. Second, Tauschinsky *et al*. [11] measured electrostatic fields of adsorbates using electromagnetically induced transparency (EIT) on Rydberg states. The results presented in this article complement the data published by these two groups. We measure the evolution of electrostatic fields at distances of 30–300 μm to the surface during a series of consecutive experiments. Starting with a clean copper surface we deposit clouds of ^{87}Rb atoms onto the surface and measure the inhomogeneous electrostatic field of polarized adatoms by spectroscopy on Rydberg states. We find that the electrostatic fields are already significant after about a few hundred experimental cycles. This corresponds to only a few hours of operation for a typical cold atom experiment.

II. MEASUREMENT OF THE ELECTROSTATIC FIELDS OF ADSORBATES BY RYDBERG EIT

We measure the electrostatic field of adsorbed and polarized adatoms through the energy shift (dc Stark shift) induced on highly excited Rydberg states of rubidium. We start our experiments with a clean copper surface which is horizontally aligned inside a vacuum chamber [Fig. 1(a)] at a base pressure of 10^{-11} mbar. We transport ultracold clouds of ^{87}Rb ($T = 1.5$ μK) with optical tweezers to a position 200 μm above the surface and release the atomic cloud. About $\sim 10^6$ atoms are dropped in each experimental cycle onto the surface. While the atomic cloud is falling towards the surface, we measure its EIT spectra.

The ladder-type excitation scheme used for the EIT measurements [13,14] is shown in Fig. 1(b). We probe the absorption on the $5S$-$5P$ transition with a weak probe laser. The $5P$ state is strongly coupled to a highly excited nS or nD Rydberg state by means of a 480-nm laser. While the frequency of the probe laser is stabilized to the $5S$-$5P$ transition, the coupling laser can be continuously scanned within a wide range of frequencies ($\pm$50 MHz). Whenever the coupling laser is on resonance with a Rydberg state, the conditions for EIT are satisfied and the atomic ensemble becomes transparent for the probe laser [15]. The presence of adsorbed atoms on the surface perturbs the Rydberg states and the resonance conditions for the coupling laser. We observe pronounced energy shifts towards the surface which increase with the deposition of atomic clouds. For the measurements we use S and D Rydberg states with principal quantum numbers n between 31 and 48.

*hattermann@pit.physik.uni-tuebingen.de
†fortagh@uni-tuebingen.de

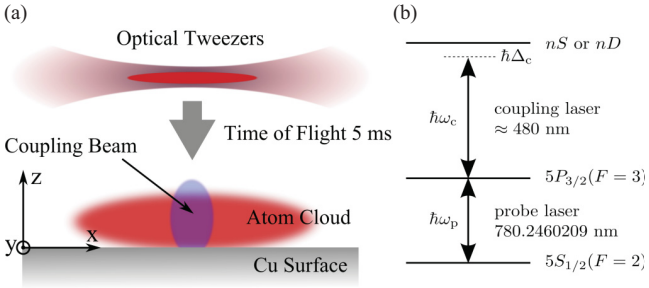

FIG. 1. (Color online) (a) An atomic cloud (10^6 ^{87}Rb atoms in the $5S_{1/2}$ ($F = 2, m_F = 2$) ground state at temperature 1.5 μK) is released from an optical dipole trap to free fall and expand. The cloud hits a Cu surface 200 μm below the trap. The electric field of polarized adatoms is tested by means of Rydberg EIT. While the probe beam illuminates the full area, the coupling beam has a smaller, elliptical spot size, illustrated in blue. (b) Ladder configuration for EIT signals. The probe beam couples the $5S_{1/2}$ ($F = 2, m_F = 2$) and the $5P_{3/2}$ ($F = 3, m_F = 3$) levels. Simultaneously, a counterpropagating coupling beam focused onto a part of the cloud (blue spot) is switched on. The lasers are referenced to a frequency comb. In Ref. [12] we describe the details of the locking method.

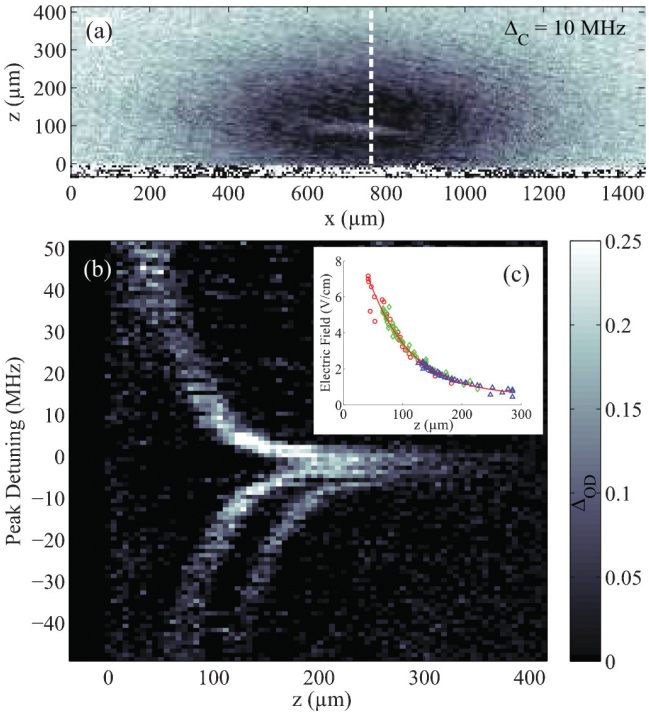

FIG. 2. (Color online) (a) Absorption image of an atomic cloud during free fall onto the surface taken with the probe beam. The stronger the absorption, the darker the pixel in the image. In this example, the coupling laser is blue detuned by 10 MHz from the $35D_{5/2}$ state of ^{87}Rb and produces a transparency window. The lateral extension of the window is given here by the width of the coupling laser beam. For the data analysis we take the z position of the transparency window along the vertical dashed line. Similar images have been taken for detunings ranging from −50 to +50 MHz, allowing the measurement of electrostatic fields as a function of z. (b) Map of the relative optical density as a function of distance to the surface (horizontal axis) and detuning of the coupling laser from the unperturbed transition frequency $5P_{3/2}$ ($F = 3$, m_F=3) → $35D_{5/2}$ (vertical axis). Each horizontal line shows a single measurement. (c) Calculated electrostatic field as function of z using the EIT measurements on the $35D_{5/2}$ state. The different colors are the field strengths obtained using the $|m_J| = 1/2$ (red circles), 3/2 (green diamonds), and 5/2 states (blue triangles). The data of the three states follow the same curve, which is well approximated by an exponential decay.

For our experiments we prepare clouds of ^{87}Rb atoms in the $5S_{1/2}$ ($F = 2, m_F = 2$) state in a setup described in Ref. [16]. The atomic cloud is loaded from a magneto-optical trap (MOT) into a Ioffe-Pritchard type magnetic trap and cooled by forced radio-frequency evaporation to a temperature of 1.5 μK. The cloud with about 10^6 atoms is then loaded into an optical dipole potential of a focused 1064-nm laser beam. By moving the focusing lens with an air bearing translation stage, the optical tweezers transport the atoms from the preparation zone over a distance of 35 mm to a position above a copper surface. The tweezers are micropositioned 200 μm above the surface and the atomic cloud is released by instantly ramping down the laser power. After 5 ms of free fall and expansion, the atomic cloud is imaged by absorption imaging. As the cloud falls, EIT spectra of the atoms are taken. The imaging beam (probe beam for the EIT) has a Gaussian profile of 7.5 mm full width at half maximum (FWHM) and ∼100 μW power. The counterpropagating coupling beam is simultaneously focused onto the cloud. It has an elliptical profile with ∼200 and 300 μm FWHM, respectively. The frequency stabilization of the lasers with an absolute accuracy of better than ±1.5 MHz is described in Ref. [12].

The measurements are illustrated in Fig. 2(a). The absorption image of an atomic cloud during free fall shows a "transparency window" at the positions where the coupling laser is resonant with the transition, in this case the $35D_{5/2}$ ($m_J = 1/2$) state. The image shows that the resonance condition is satisfied only in a small window revealing a spatial inhomogeneity of the energy shift. In this window the shift of the Rydberg level equals the detuning Δ_C of the coupling laser, in this example +10 MHz with respect to the unperturbed transition frequency. If the detuning of the coupling laser is changed, the transparency window appears at a different distance from the surface.

We take a series of absorption images as a function of the detuning Δ_C. The laser frequency is varied in steps of 1 MHz between consecutive measurements. The results are summarized in Fig. 2(b), which shows the Stark shift of Rydberg states as a function of the distance z to the surface. Each horizontal line of Fig. 2(b) is obtained from the vertical column of absorption images, as indicated by the vertical dashed line in Fig. 2(a). Thus it shows the position of the transparency window for different detunings. The three branches in Fig. 2(b) correspond to the projections of the total angular momentum J of the $35D_{5/2}$ Rydberg state: $|m_J| = 1/2, 3/2$, and $5/2$.

We now determine the electrostatic field above the copper surface by using the measured Stark shifts and comparing them with the theoretically calculated shift of Rydberg levels in electrostatic fields. We calculate the Stark maps with the numerical method of Ref. [17]. For our evaluation, we use

an algorithm which identifies the electrostatic fields that best fit the measured data. As shown in Fig. 2(c), the results for the three different $|m_J|$ states lie on the same curve, confirming the validity of our procedure. The shifts of the Rydberg states are thus explained by static electric fields alone. The decay of the electrostatic field is modeled here with an exponential function: $E(z) = E_0 \exp(-z/\sigma) + E_{\text{res}}$, where z is the distance to the surface, σ is the decay length, and E_{res} is a residual, homogeneous electrostatic field that accounts for possible external field sources. Figure 2(c) shows the best-fit fields calculated with the three experimental curves of Fig. 2(b). We repeated our measurements on S and D Rydberg states with principal quantum numbers n between 31 and 48 that reproduce the same behavior. For distances smaller than 30 μm, the electrostatic field cannot be determined reliably, as high field gradients over the size of one pixel of the camera (5.6 μm in the object plane) lead to blurring of the measured line shifts. We note that the electric field is also inhomogeneous along the x axis. This is a result of the Gaussian distribution of the atomic clouds dropped onto the surface and of the residual roughness of the copper. In order to facilitate the evaluation of the changes of the field with time, all the measurements have been evaluated along the same line, as indicated in Fig. 2(a).

III. TEMPORAL EVOLUTION OF THE ELECTROSTATIC FIELDS OF DEPOSITED ADATOMS

We evaluate the evolution of the electrostatic field close to the surface as atom clouds are repeatedly deposited on it. Figure 3 summarizes the results. The diagram shows the electric field as a function of the distance from the surface and the number of deposited atomic clouds. Different colors correspond to different strengths of the electric field. The red (solid) lines are exponential fits that we use for determining the electric field as in Sec. II. The inset shows the increase of the measured electric field with the number of deposited atoms

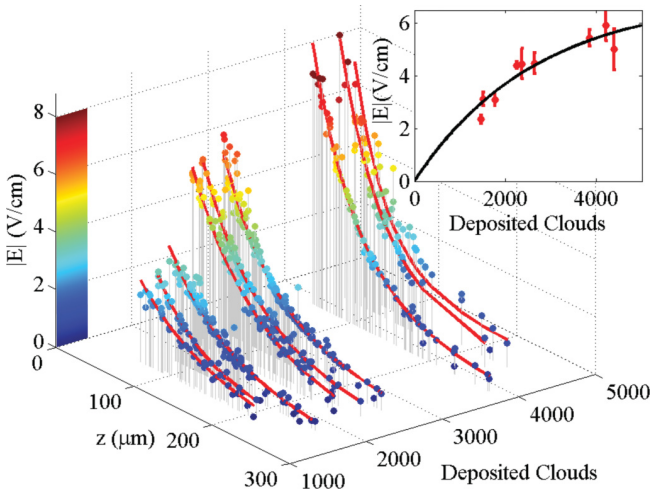

FIG. 3. (Color online) Measured electrostatic field as a function of z and the number of experimental cycles carried out. Inset: Measured electrostatic field at a distance of 80 μm from the surface. We observe an increase of the electric field due to adsorption of rubidium onto the copper surface. The saturation builds up after the deposition of few thousand atomic clouds.

for a distance of 80 μm from the surface. The magnitude of the field increases with the number of experimental runs. However, we observe a saturation after about ten days of experiments during which we released approximately 5×10^9 atoms on the copper surface. Based on our measurements, we estimate that it takes as little as few hundred experimental runs to produce an electric field of 1 V/cm at a distance of 30 μm, assuming a zero-field at the beginning of the experiments. This field produces a level shift of -2 MHz on the $35S_{1/2}$ state and of -49 MHz on the $55S_{1/2}$ state. This is much larger than the linewidth of a high-Q stripline resonator, making cavity QED experiments problematic by shifting the atoms out of the cavity resonance.

IV. CONCLUSION

Our measurements show that neutral atoms adsorbed on a metal surface cause electrostatic fields on the order of 1 V/cm after as little as 100 repetitions of a cold atom experimental cycle. Adsorbate fields have also been observed on dielectric surfaces [18]. This sets serious limitations on the feasibility of cavity QED experiments with Rydberg atoms and coplanar cavities. Also dispersion forces between Rydberg atoms and planar surfaces [19] are masked by the strong electric fields of adsorbates. A search for strategies to correct for this problem is therefore very important for atom chips. A possible solution could be the cleaning of the surface whenever the electrostatic fields due to adsorbates become harmful. For example, regular heating of the surface cause adsorbed atoms to diffuse. Another possibility would be photodissorption of the adsorbed atoms, but given the work function of metals, this would require light in the far ultraviolet range. Given the fast appearance of detrimental adsorbate fields, an open question is still if there are cleaning techniques which can be applied quickly between experimental cycles. A workaround for this problem would be the development of experimental techniques that avoid deposition of atoms onto the surface or using surface coatings with materials on which no adsorbate fields have been observed [14]. While atoms on surfaces have undesired effects on cold atom experiments, it is worth mentioning that adatoms may be useful to control electric properties of surface layers. For example, alkali-metal adsorbates have been used to engineer the electronic structure of graphene [20,21].

Rydberg EIT can be used for a sensitive measurement of electric fields. In combination with micropositioning of atomic clouds by optical tweezers or magnetic conveyor belts in a scanning probe configuration [22] three-dimensional imaging of the electric field distribution is feasible. However, the measurement technique contaminates the surface, which must be taken into account.

ACKNOWLEDGMENTS

The authors would like to thank Thomas Judd for useful discussions. This work was supported by the European Research Council (Socathes) and the Deutsche Forschungsgemeinschaft (SFB TRR21). The authors acknowledge additional support from the Evangelisches Studienwerk Villigst e.V. and the Baden-Württemberg-Stiftung through the "Kompetenznetz Funktionelle Nanostrukturen."

[1] T. F. Gallagher, *Rydberg Atoms* (Cambridge University Press, Cambridge, UK, 1994).
[2] J. M. Raimond, M. Brune, and S. Haroche, Rev. Mod. Phys. **73**, 565 (2001).
[3] D. Petrosyan and M. Fleischhauer, Phys. Rev. Lett. **100**, 170501 (2008).
[4] D. Petrosyan, G. Bensky, G. Kurizki, I. Mazets, J. Majer, and J. Schmiedmayer, Phys. Rev. A **79**, 040304 (2009).
[5] M. Saffman, T. G. Walker, and K. Mølmer, Rev. Mod. Phys. **82**, 2313 (2010).
[6] L. DiCarlo, J. M. Chow, J. M. Gambetta, L. S. Bishop, B. R. Johnson, D. I. Schuster, J. Majer, A. Blais, L. Frunzio, S. M. Girvin, and R. J. Schoelkopf, Nature (London) **460**, 240 (2009).
[7] A. Wallraff, D. Schuster, A. Blais, L. Frunzio, R. Huang, J. Majer, S. Kumar, S. Girvin, and R. Schoelkopf, Nature (London) **431**, 162 (2004).
[8] S. D. Hogan, J. A. Agner, F. Merkt, T. Thiele, S. Filipp, and A. Wallraff, Phys. Rev. Lett. **108**, 063004 (2012).
[9] J. M. McGuirk, D. M. Harber, J. M. Obrecht, and E. A. Cornell, Phys. Rev. A **69**, 062905 (2004).
[10] J. M. Obrecht, R. J. Wild, and E. A. Cornell, Phys. Rev. A **75**, 062903 (2007).
[11] A. Tauschinsky, R. M. T. Thijssen, S. Whitlock, H. B. van Linden van den Heuvell, and R. J. C. Spreeuw, Phys. Rev. A **81**, 063411 (2010).
[12] M. Mack, F. Karlewski, H. Hattermann, S. Höckh, F. Jessen, D. Cano, and J. Fortágh, Phys. Rev. A **83**, 052515 (2011).
[13] A. K. Mohapatra, T. R. Jackson, and C. S. Adams, Phys. Rev. Lett. **98**, 113003 (2007).
[14] H. Kübler, J. P. Shaffer, T. Baluktsian, R. Löw, and T. Pfau, Nat. Photonics **4**, 112 (2010).
[15] M. Fleischhauer, A. Imamoglu, and J. P. Marangos, Rev. Mod. Phys. **77**, 633 (2005).
[16] D. Cano, H. Hattermann, B. Kasch, C. Zimmermann, R. Kleiner, D. Koelle, and J. Fortágh, Eur. Phys. J. D **63**, 17 (2011).
[17] M. L. Zimmerman, M. G. Littman, M. M. Kash, and D. Kleppner, Phys. Rev. A **20**, 2251 (1979).
[18] R. P. Abel, C. Carr, U. Krohn, and C. S. Adams, Phys. Rev. A **84**, 023408 (2011).
[19] J. A. Crosse, S. A. Ellingsen, K. Clements, S. Y. Buhmann, and S. Scheel, Phys. Rev. A **82**, 010901 (2010).
[20] T. Ohta, A. Bostwick, T. Seyller, K. Horn, and E. Rotenberg, Science **313**, 951 (2006).
[21] K.-H. Jin, S.-M. Choi, and S.-H. Jhi, Phys. Rev. B **82**, 033414 (2010).
[22] M. Gierling, P. Schneeweiss, G. Visanescu, P. Federsel, M. Häffner, D. P. Kern, T. E. Judd, A. Günther, and J. Fortágh, Nat. Nanotechnol. **6**, 446 (2011).